Electronic Supplementary Information

A Soft Molecular 2Fe 2As Precursor Approach to Nanostructured FeAs For Efficient Electrocatalytic Water Oxidation

Rodrigo Beltrán-Suito,[+,a] Viktoria Forstner,[+,a] J. Niklas Hausmann,[a] Stefan Mebs,[b] Johannes Schmidt,[c] Ivelina Zaharieva,[b] Konstantin Laun,[d] Ingo Zebger,[d] Holger Dau,[b,*] Prashanth W. Menezes,[a,*] and Matthias Driess[a,*]

[a.] Department of Chemistry: Metalorganics and Inorganic Materials, Technische Universität Berlin, Straße des 17 Juni 135, Sekr. C2, 10623 Berlin, Germany. E-mail: prashanth.w.menezes@tu-berlin.de, matthias.driess@tu-berlin.de

[b.] Fachbereich Physik, Freie Universität Berlin, Arnimallee 14, 14195 Berlin, Germany. E-mail: holger.dau@fu-berlin.de

[c.] Department of Chemistry: Functional Materials, Technische Universität Berlin, Hardenbergstraße 40, 10623 Berlin, Germany

[d.] Institut für Chemie, Max-Volmar-Laboratorium für Biophysikalische Chemie, Technische Universität Berlin, Straße des 17 Juni 135, 10623 Berlin, Germany

[+] These authors contributed equally to this work.

Table of Contents

Experimental Procedures

General considerations and instrumentation. All synthetic procedures were done under inert conditions using standard Schlenk techniques or a M. Braun dry box containing an atmosphere of inert purified nitrogen. Solvents were dried by standard methods. ^{1}H NMR spectra were recorded on a Bruker Spectrometer APX 200 at room temperature and the solvent residual signals were referenced as the internal standard. Fourier transform infrared (FTIR) spectra were recorded on a Thermofisher Nicolet iS5 IR spectrometer (ATR-Diamond) under inert conditions. Elemental analysis was carried out with a Thermo Flash EA 1112 Organic Elemental Analyzer by dynamic flash combustion at 1020 °C.

All experiments and measurements were reproduced for three times and the values derived from them are reported as mean ± standard deviation.

Materials and synthesis

1 M aqueous KOH and other reagents used in the synthetic procedures were obtained from Sigma Aldrich. Nickel foam (NF) and fluorine-doped tin oxide (FTO, resistivity 8−12 Ω sq^{-1}) were purchased from Recemat BV and Sigma Aldrich, respectively. Fe_2O_3 was purchased from Sigma Aldrich. The molecular complex precursors L^BFeCl (L^B = CH(C^{t}BuNDipp)$_2$, Dipp = 2,6-^{i}Pr$_2$C$_6$H$_3$) and NaOCAs·(dioxane)$_{2.1}$ were prepared according to literature procedures.[1–4]

Synthesis of L^BFeAs$_2$FeL^B. L^BFeCl (447 mg; 0.75 mmol; 1.0 eq.) and NaOCAs·(dioxane)$_{2.1}$ (258 mg; 0.83 mmol; 1.1 eq.) were stirred in 50 mL toluene for 5 h at room temperature, during which the initially dark red solution turned dark brown. The reaction mixture was filtered and the residue washed again with 10 mL toluene. The filtrate was then carefully concentrated to one-sixth of its volume so that a dark red crystalline solid could be isolated after one day at 5 °C. The dinuclear iron arsenide cluster complex L^BFeAs$_2$FeL^B was obtained in 40 % yield (220 mg, 0.15 mmol) relative to the iron precursor. Two molecules of toluene co-crystallized with the compound. *Elemental analysis:* (%) calc. for M·2 tol: C: 69.60, H: 8.50, N: 3.87; found: C: 66.89, H: 8.14, N: 3.69. Despite repeated attempts, we have not been able to obtain an accurate analysis of a spectroscopically pure sample. The slight difference in carbon content can be explained by the high sensitivity of the molecule. Due to severe fragmentation, no indication of the synthesized complex could be observed in mass spectrometry. *^{1}H NMR (*paramagnetic, 200 MHz, C$_6$D$_6$, Figure S1): δ/ppm = 104.23 (1H, γ-*H*)*; 41.98 (18H, ^{t}Bu-H)*; 7.03 (m, tol); 2.11 (s, tol); 1.28*; -27.58 (12H, Dipp-C*H*$_3$)*; -108.88 (2H, p-*H*)*; -112.01 (12H, Dipp-C*H*$_3$)*. Because of the highly paramagnetic nature of the compound and the extreme broadening observed, signals could only be tentatively assigned. Signals marked with (*) have been observed for the iron chloride precursor as well. These signals appeared both *in-situ* and in solutions from sufficiently pure crystalline samples, and can thus be assigned to the iron arsenide complex. It has to be noted that many three-coordinate iron complexes L^BFeR (with R = hydride, halide, alkyl, amide) exhibit very similar signal patterns and shifts.[5–9] *ATR-IR data* (Figure S2): $\tilde{\nu}$/cm^{-1} = 2957 (s), 2922 (s, 2906 (s), 2865 (s), 1999 (w), 1920 (w), 1535 (w),

1485 (s), 1460 (m), 1443 (m), 1432 (m), 1400 (w), 1379 (s), 1358 (s), 1311 (s), 1280 (m), 1251 (m), 1214 (m), 1200 (w), 1188 (s), 1177 (s), 1154 (m), 1126 (m), 1097 (m), 1054 (m), 1028 (m), 957 (w), 934 (m), 918 (w), 899 (w), 888 (w), 878 (w), 839 (w), 815 (w), 799 (m), 776 (s), 764 (m), 754 (s), 730 (s), 717 (w), 695 (m), 677 (m), 664 (w), 647 (w). CCDC 1989143 contains the supplementary crystallographic data for this paper. This data is provided free of charge by The Cambridge Crystallographic Data Centre.

Synthesis of crystalline FeAs by hot injection. The modification of a previously developed procedure was used.[10] To a three-necked round bottom Schlenk flask fitted with a temperature sensor and a condenser, 25 mL oleylamine (Sigma-Aldrich) was added. The solvent was previously degassed by a 3-cycle freeze-pump method and stored with molecular sieves (3 Å). The whole set up was degassed using a vacuum followed by nitrogen refill three times and then the flask was heated to 250 °C. The $L^BFeAs_2FeL^B$ precursor (1449.46 g mol^{-1}; 150 mg; 0.103 mmol) was dissolved in 5 mL of dry oleylamine at 35 °C in another flask. The solution was transferred to the three-necked flask at 250 °C by injection under inert conditions. The reaction temperature was maintained at 250 °C for one more hour and then the mixture was allowed to cool down naturally to room temperature. The whole reaction mixture was transferred into a centrifuge tube and centrifuged along with additional 20 mL ethanol at 9000 rpm to produce a black solid. The mixture was placed 15 min in the ultrasonic bath to remove any excess ligand and oleylamine. Sonication and centrifugation cycles were repeated for 4 additional times. The precipitate was then washed with acetone and dried overnight at 60 °C and used for characterizations.

Synthesis of amorphous $Fe(OH)_3$ and FeOOH. Amorphous $Fe(OH)_3$ was synthesized by precipitation of iron(III) nitrate following a reported protocol and FeOOH by precipitation of iron(II) sulfate followed by oxidation with H_2O_2.[11,12]

Characterization

Powder X-ray and neutron diffraction. Powder X-ray diffraction (PXRD) patterns were obtained on a Bruker AXS D8 advanced automatic diffractometer equipped with a position-sensitive detector (PSD) and curved germanium (111) primary monochromator using Cu Kα radiation (λ = 1.5418 Å).

Inductively coupled plasma atomic emission spectroscopy. The inductively coupled plasma atomic emission spectroscopy (ICP-AES) was conducted on a Thermo Jarrell Ash Trace Scan analyzer. The materials were digested in aqua regia HCl: HNO_3 4:1 v/v (nitric acid, SUPRA-Qualität ROTIPURAN® Supra 69% and hydrochloric acid, SUPRA-Qualität ROTIPURAN® Supra 30%) and the average of three reproducible independent experiments is reported. The digestion volume (2.5 mL) was diluted with Milli-Q water up to 15 mL. Calibration curves were prepared for iron and arsenic with concentrations between 1 mg L^{-1} and 100 mg L^{-1} from standard solutions (1000 mg L^{-1} Single-Element ICP-Standard Solution ROTI STAR).

Scanning electron microscopy. Scanning electron microscopy (SEM) was performed on a GeminiSEM500 NanoVP microscope (ZEISS) integrated with an EDX detector (Bruker Quantax XFlash® 6|60). The most abundant elements were selected from the EDX spectrum. Data handling and analysis were achieved with the software package EDAX. The SEM experiments were conducted at the Zentrum für Elektronenmikroskopie (ZELMI) of the TU Berlin.

Transmission electron microscopy. Transmission electron microscopy (TEM) was performed on an FEI Tecnai G2 20 S-TWIN transmission electron microscope (FEI Company, Eindhoven, Netherlands) equipped with a LaB_6 source at 200 kV acceleration voltage. For the investigation of the films after electrocatalysis, the films were scratched from the electrode substrate and transferred onto a carbon-coated copper grid. EDX analyses were achieved with an EDAX r-TEM SUTW detector (Si (Li) detector), and the images were recorded with a GATAN MS794 P CCD camera. The TEM experiments were conducted at the Zentrum für Elektronenmikroskopie (ZELMI) of the TU Berlin.

X-ray photoelectron spectroscopy. X-ray photoelectron spectroscopy (XPS) measurements were carried out using a ThermoScientific K-Alpha+ X-ray photoelectron spectrometer. All samples were analyzed using a micro-focused, monochromated Al-K_α X-ray source (1486.68 eV; 400 μm spot size). The analyzer had pass energy of 200 eV (survey), and 50 eV (high-resolution spectra), respectively. Binding energies were calibrated to the C 1s peak at 284.8 eV. To prevent any localized charge build-up during analysis the K-Alpha+ charge compensation system was employed at all measurements. The samples were mounted on conductive carbon tape or measured directly from the electrode substrates (FTO and NF). The resulting spectra were analyzed using the Avantage software from ThermoScientific.

Extended X-ray absorption fine structure (EXAFS) and X-ray absorption near edge structure (XANES). The experiments were conducted at the KMC3 beamline of the BESSY synchrotron operated at the Helmholtz-Zentrum Berlin (HZB). Data collection was performed at 20 K in a liquid-helium cryostat in fluorescence detection mode using a 13 element silicon drift detector (Rayspec). Over 20 spectra were averaged for each compound in order to improve the signal-to-noise ratio. Averaged spectra were background-corrected and normalized using in-house software. Subsequently, unfiltered k^3-weighted spectra and phase functions from FEFF8.5[13] were used for the least-squares curve-fitting of the EXAFS with in-house software and for calculation of Fourier-transforms representing k-values between 1.6 and 14 $Å^{-1}$. Data were multiplied by a fractional cosine window (10% at low and high k-side); the amplitude reduction factor S_0^2 was 0.75 for iron and 1.00 for arsenic. The samples were kept for 6 h under constant current of 10 mA cm^{-2} using FeAs/FTO as working electrode (WE), Pt wire as counter electrode (CE) and Hg/HgO electrode (CH Instruments) as reference electrode (RE) on a three electrode system on KOH 1 M. After that time, the experiment was stopped and the sample was immediately immersed on liquid N_2 (77 K) to freeze quench it. The sample was stored and taken to BESSY for measurement.

Resonance Raman spectroscopy. Resonance Raman spectra were recorded using the 458 nm emission of an Argon ion laser (Innova 70, Coherent) for excitation and a confocal Raman spectrometer (Lab Ram HR- 800 Jobin Yvon) equipped with a liquid-nitrogen cooled charge-coupled device (CCD) camera for data acquisition. The typical laser power at the sample ranged between 2-3 mW. The samples were measured using a Linkam Cryostage THMS600 cryostat. The temperature of the samples was kept at 80 K throughout the measurements. The spectrometer was calibrated before each experiment using toluene as an external standard. Baseline subtraction/processing from FTO was performed for analyzing the data.

.

Infrared spectroscopy. Infrared (IR) spectra were recorded on a Thermo Fisher Nicolet iS5 Fourier transform (FT) IR spectrometer using a Diamond for the Attenuated Total Reflexion (ATR) IR measurements.

Resistivity measurement. A Signature Pro4 System measured the resistivity with Keithley 2400 source-measure unit (SP4-40045TBY) using a four-point probe resistivity technique. The spacing between tungsten carbide tips was 1.016 mm with a radius of 0.245 mm, and a spring pressure was 45 grams. The materials were electrophoretically deposited on electrodes to estimate the specific resistivity of each synthesized material, and the average results are presented.

BET surface area. The determination of the surface area was performed by Nitrogen sorption using the BET (Brunauer-Emmet-Teller) method. Measurements were performed with a Nova 4000e from Quantachrome Instruments. Degassing was performed at 120 ºC for 12 h before conducting the measurement.

Electrochemical measurements

A typical electrocatalytic run was carried out in a standard three-electrode setup consisting of a reference electrode (RE), a counter electrode (CE) and the catalyst-modified working electrode (WE). The three were immersed in an aqueous electrolyte (1M KOH, Sigma Aldrich). The presence of Fe on it was ruled out by purifying the electrolyte before its use following the literature procedure.[14] A potentiostat (SP-200, BioLogic Science Instruments) controlled by the EC-Lab v10.20 software package was used for all the experiments. The electrodes (NF/FTO) with samples deposited served as the WE, Pt wire (0.5 mm diameter × 230 mm length; A-002234, BioLogic) as the CE and Hg/HgO (OER) as the RE (CH Instruments, Inc.).

CV and LSV. Cyclic voltammetry (CV) and linear sweep voltammetry (LSV) was performed without stirring and with an applied iR compensation of 85%, applied before each experiment. The uncompensated resistance (R_u) was acquired by impedance spectroscopy at 100 MHz. The potential of the reference electrode in this work was referenced to the reversible hydrogen electrode (RHE) through calibration, and in 1 M aqueous KOH the potential was calculated using the following equation:

$E(\text{RHE}) = E(\text{Hg/HgO}) + 0.098\ \text{V} + (0.059 \times \text{pH})\ \text{V}.$

The potential ranges were 1.0 to 1.8 V vs. RHE for OER on NF, 1.2 to 1.9 V vs. RHE for OER on FTO. The presented LSV polarization were derived from CV experiments carried for a specific time until no changes where observed on the electrochemical behaviour, i.e. when the shape of the CV curve showed no more variation and the overpotential was constant.

Chronopotentiometry. The chronopotentiometry measurements were performed in 1 M aqueous KOH, an applied iR compensation of 85% and at a constant current density of 10 mA cm^{-2} for 24 h.

Chronoamperometry. The chronoamperometry measurements were performed in 1 M aqueous KOH, applied iR compensation of 85% and at a constant potential of 1.38 V *vs.* RHE (η = 480 mV, OER) was applied for 10 h for the NF sample.

Tafel analysis. The polarization curves were replotted as overpotential (η) vs. the logarithm of current density (log j) to obtain Tafel plots. The Tafel slope was calculated according to the Tafel equation $\eta = b\log j + a$, where η is the overpotential (V), j is the current density (mA cm^{-2}), and b is the Tafel slope (mV dec^{-1}).

Double-layer capacitance. The double-layer capacitance (C_{dl}) was determined to calculate the active surface area of the materials and the substrate.[15] From the already measured LSV, a potential range in which no faradaic process (no catalysis) is occurring was selected (0.881 to 0.931 V vs. RHE). The anodic charging currents measured at 0.906 V vs. RHE were plotted as a function of the scan rate (5 mV s^{-1} to 200 mV s^{-1}) and from the slope, the C_{dl} was attained.[15–17] The ECSA is directly proportional to C_{dl}.[10]

Electrochemical impedance spectroscopy. Electrochemical impedance spectroscopy (EIS) was recorded at 1.58 V vs. RHE for FTO samples and at 1.51 V vs RHE for NF samples to obtain the Nyquist plots. The selected potentials are beyond onset potential and all the studied catalysts have appreciable activity at it (> 10 mA cm^{-2}).[18] The amplitude of the sinusoidal wave was examined in a frequency range of 100 kHz to 1 mHz. The curves were fitted to a Randles equivalent circuit (inset, Figure 3 on Main Text), where R_s, CPE, and R_{ct} are the equivalent series resistance, constant phase element of the C_{dl}, and the charge transfer resistance, respectively.[10,15,19] Mean values and standard deviations of the parameters derived from the fitting of the experimental data were obtained using the Zfit tool from EC-Lab® Version 11.10 (January 2017) software (Bio-Logic Science Instruments Ltd.).

Electrophoretic deposition (EPD, film preparation). The investigated materials were deposited electrophoretically by a well-established method on both, on a 1 x 1 cm^2 NF and FTO electrode.[10,12,20–22] The electric charge on the catalyst in acetone is insufficient for EPD, as very small amounts of free ions exist in acetone. When iodine is used as the dispersant, it can react with acetone through the keto-enol tautomerization to produce protons as per the following equation:

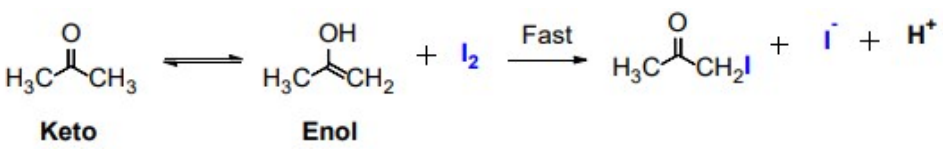

Thus, formed protons are adsorbed on the surface of the suspended particles by making them positively charged. The applied electric field induces the positively charged particles to migrate towards and deposit on the cathode. Typically, 30-40 mg of the catalyst powder was suspended in 10 mL acetone and sonicated for 1 h then 3 mg of iodine was added and the suspension sonicated for another 3 min. The EPD was conducted at +10.0 V for 4 min and thin uniform films were obtained. The sample loading on each NF was 1.0 ±0.1 mg cm^{-2} for all the tested materials. On FTO, it was 0.4 ±0.1 mg cm^{-2} for FeAs, FeOOH and Fe_2O_3, and 2.4 ±0.1 mg cm^{-2} for $Fe(OH)_3$.

Results and Discussion

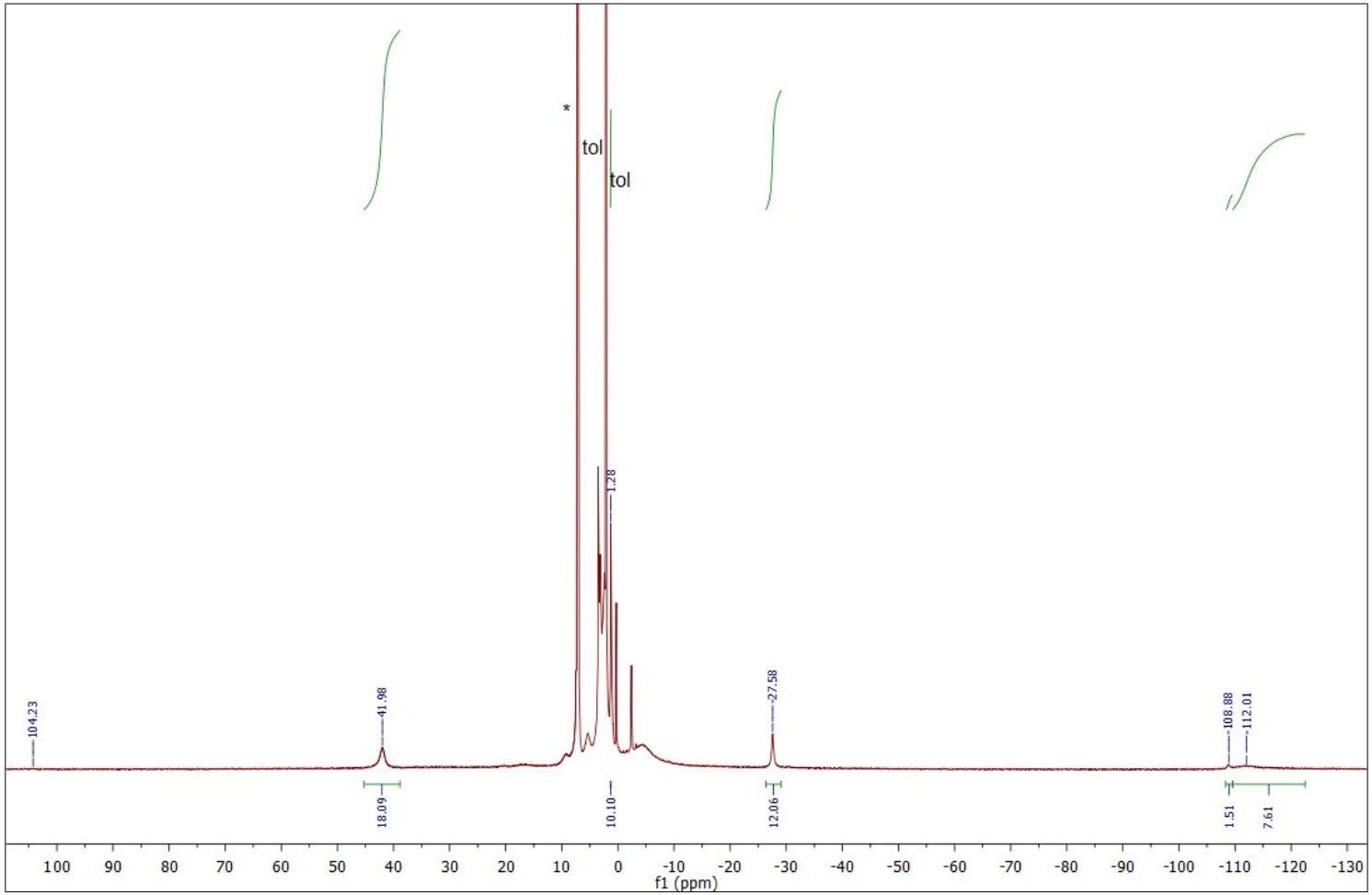

Figure S1. ^{1}H NMR of **2**·2 tol in C_6D_6 at room temperature.

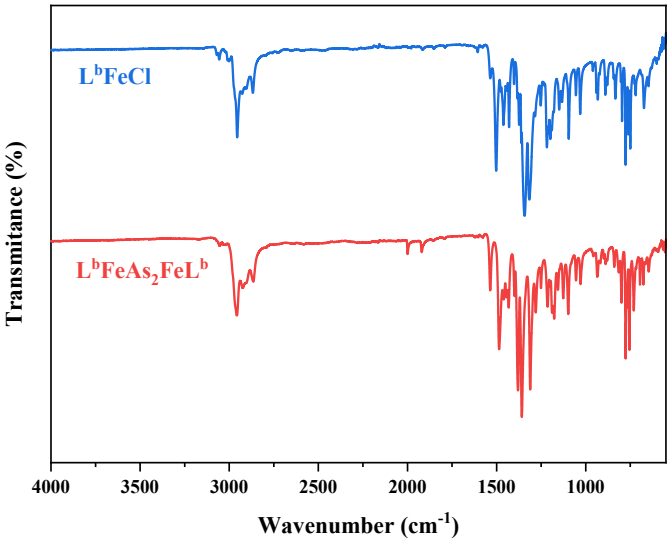

Figure S2. Comparison of the ATR-IR spectra of the precursor $L^{B}FeCl$ (blue trace, top) and **2** (red trace, bottom).

Table S1. Crystal data and structure refinement for **2**·2 tol.

Empirical formula	$C_{84}H_{122}N_4Fe_2As_2$	
Formula weight	1449.38	
Crystal system	monoclinic	
Space group	$P2_1/n$	
Unit cell dimensions	a = 13.4664(2) ☐Å	α = 90 ☐°
	b = 14.7987(2) ☐Å	β = 91.2700(10) °
	c = 19.6270(3) ☐Å	γ = 90 °
Cell Volume	3910.41(10) ☐Å^3	
Z	2	
Temperature	150.(2) K	
Crystal size	0.226 x 0.208 x 0.064 mm^3	
Density	1.23 mg·m^{-3}	
F(100)	1544	
Absorption coefficient	4.240 mm^{-1}	
Transmission max/min	1.00000/0.63919	
Refinement method	Full-matrix least-squares on F^2	
Absorption correction	Semi-empirical from equivalents	
Wavelength	1.54184 (Cu) ☐Å	
Collected/independent reflections	26275/7050 (0.0463)	
Index ranges	$-15 \le h \le 16$ $-17 \le k \le 12$ $-23 \le l \le 23$	
Theta range for data collection	3.741 - 67.496 °	
Completeness to theta = 67.49 °	100.00 %	
☐Data / restraints / parameter	7050 / 261 / 525	

R_1/wR_2 $[I > 2\sigma(I)]$	0.0364/0.0929
R_1/wR_2 (all data)	0.0455/0.1001
☐*Goodness-of-fit* on F^2	1.033
Largest diff. peak and hole	0.612/-0.425 e·Å^{-3}

Table S2. Atomic coordinates (x 10^4) and equivalent isotropic displacement parameters ($Å^2$x 10^3) for kria. U(eq) is defined as one third of the trace of the orthogonalized U^{ij} tensor.

	x	y	z	U(eq)
As(1)	5070(1)	5383(1)	5522(1)	28(1)
Fe(1)	4719(1)	6233(1)	4502(1)	22(1)
N(2)	3429(1)	6857(1)	4274(1)	24(1)
C(12)	2607(2)	6577(2)	4679(1)	26(1)
C(2)	5232(2)	7798(1)	3650(1)	25(1)
C(4)	3362(2)	7540(2)	3825(1)	26(1)
C(24)	6621(2)	7119(2)	4294(1)	27(1)
C(3)	4210(2)	7890(2)	3519(1)	27(1)
C(13)	2012(2)	5841(2)	4473(1)	32(1)
C(25)	7285(2)	6558(2)	3950(1)	34(1)
C(17)	2435(2)	7033(2)	5294(1)	37(1)
C(1)	5850(2)	8507(2)	3234(1)	32(1)
C(14)	1208(2)	5613(2)	4873(1)	40(1)
C(29)	6933(2)	7616(2)	4872(1)	36(1)
C(15)	992(2)	6095(2)	5454(1)	43(1)
C(26)	8282(2)	6572(2)	4153(2)	46(1)
C(5)	2386(2)	8025(2)	3568(1)	36(1)
C(16)	1604(2)	6788(2)	5663(1)	41(1)
C(27)	8612(2)	7113(2)	4682(2)	53(1)
C(11)	2250(2)	7821(2)	2803(1)	49(1)
C(6)	5445(2)	9466(2)	3353(2)	50(1)
C(33)	6966(2)	5961(2)	3356(1)	43(1)
C(28)	7943(2)	7613(2)	5044(2)	47(1)
C(21)	2201(2)	5303(2)	3832(1)	45(1)
C(10)	2509(2)	9053(2)	3666(2)	48(1)
C(7)	5699(3)	8280(2)	2474(1)	55(1)
C(35)	7196(2)	4970(2)	3509(2)	47(1)
C(23)	2340(2)	4301(2)	3987(2)	53(1)
C(8)	6970(2)	8575(2)	3377(2)	48(1)
C(9)	1397(2)	7784(2)	3905(2)	54(1)
C(30)	6269(8)	8189(5)	5260(4)	46(2)
C(18)	3093(3)	7786(2)	5561(2)	60(1)
C(22)	1353(3)	5396(2)	3295(2)	71(1)
C(20)	3603(2)	7507(3)	6234(2)	68(1)
C(34)	7445(4)	6208(2)	2683(2)	80(1)
C(32)	6238(7)	7847(5)	5998(4)	51(2)
C(19)	2518(4)	8672(2)	5667(2)	82(1)
C(31)	6597(7)	9185(3)	5261(3)	67(2)
C(36)	687(4)	10472(4)	5733(3)	86(2)

C(37)	212(4)	10007(4)	6330(3)	52(1)
C(41)	-212(9)	9985(6)	7512(4)	68(2)
C(40)	-685(8)	9166(5)	7421(3)	66(2)
C(42)	233(9)	10407(5)	6967(4)	58(2)
C(39)	-679(5)	8748(4)	6789(3)	58(1)
C(38)	-226(4)	9167(4)	6247(3)	50(1)
C(36B)	523(10)	11454(11)	7223(9)	88(4)
C(37B)	396(11)	10219(13)	6426(11)	80(5)
C(41B)	-400(30)	9973(18)	7462(12)	74(5)
C(40B)	-640(20)	9122(18)	7259(13)	87(5)
C(42B)	150(20)	10510(14)	7055(12)	76(5)
C(39B)	-421(19)	8842(16)	6622(13)	95(6)
C(38B)	109(14)	9385(15)	6209(10)	96(5)
C(31B)	5811(11)	9019(6)	5152(5)	55(3)
C(30B)	6098(15)	8059(7)	5380(7)	35(3)
C(32B)	6400(14)	8118(9)	6138(7)	52(3)

Table S3. Bond lengths [Å] and angles [°] for **2**·2 tol.

As(1)-As(1)#1	2.3447(5)
As(1)-Fe(1)	2.4023(4)
As(1)-Fe(1)#1	2.4087(4)
Fe(1)-N(2)	2.0085(18)
Fe(1)-N(1)	2.0096(18)
N(1)-C(2)	1.338(3)
N(1)-C(24)	1.443(3)
N(2)-C(4)	1.342(3)
N(2)-C(12)	1.438(3)
C(12)-C(13)	1.407(3)
C(12)-C(17)	1.407(3)
C(2)-C(3)	1.401(3)
C(2)-C(1)	1.577(3)
C(4)-C(3)	1.402(3)
C(4)-C(5)	1.571(3)
C(24)-C(25)	1.404(3)
C(24)-C(29)	1.408(3)
C(3)-H(3)	0.9500
C(13)-C(14)	1.392(3)
C(13)-C(21)	1.516(4)
C(25)-C(26)	1.392(4)
C(25)-C(33)	1.518(4)
C(17)-C(16)	1.394(4)
C(17)-C(18)	1.510(4)
C(1)-C(8)	1.531(4)
C(1)-C(7)	1.538(4)
C(1)-C(6)	1.540(3)
C(14)-C(15)	1.380(4)
C(14)-H(14)	0.9500
C(29)-C(28)	1.393(4)
C(29)-C(30)	1.458(11)
C(29)-C(30B)	1.654(19)
C(15)-C(16)	1.373(4)
C(15)-H(15)	0.9500
C(26)-C(27)	1.376(4)
C(26)-H(26)	0.9500
C(5)-C(11)	1.540(4)
C(5)-C(10)	1.541(4)
C(5)-C(9)	1.542(4)
C(16)-H(16)	0.9500
C(27)-C(28)	1.376(5)
C(27)-H(27)	0.9500
C(11)-H(11A)	0.9800

C(11)-H(11B)	0.9800
C(11)-H(11C)	0.9800
C(6)-H(6A)	0.9800
C(6)-H(6B)	0.9800
C(6)-H(6C)	0.9800
C(33)-C(34)	1.526(4)
C(33)-C(35)	1.529(4)
C(33)-H(33)	1.0000
C(28)-H(28)	0.9500
C(21)-C(23)	1.525(4)
C(21)-C(22)	1.543(4)
C(21)-H(21)	1.0000
C(10)-H(10A)	0.9800
C(10)-H(10B)	0.9800
C(10)-H(10C)	0.9800
C(7)-H(7A)	0.9800
C(7)-H(7B)	0.9800
C(7)-H(7C)	0.9800
C(35)-H(35A)	0.9800
C(35)-H(35B)	0.9800
C(35)-H(35C)	0.9800
C(23)-H(23A)	0.9800
C(23)-H(23B)	0.9800
C(23)-H(23C)	0.9800
C(8)-H(8A)	0.9800
C(8)-H(8B)	0.9800
C(8)-H(8C)	0.9800
C(9)-H(9A)	0.9800
C(9)-H(9B)	0.9800
C(9)-H(9C)	0.9800
C(30)-C(32)	1.537(6)
C(30)-C(31)	1.539(6)
C(30)-H(30)	1.0000
C(18)-C(20)	1.532(5)
C(18)-C(19)	1.540(5)
C(18)-H(18)	1.0000
C(22)-H(22A)	0.9800
C(22)-H(22B)	0.9800
C(22)-H(22C)	0.9800
C(20)-H(20A)	0.9800
C(20)-H(20B)	0.9800
C(20)-H(20C)	0.9800
C(34)-H(34A)	0.9800
C(34)-H(34B)	0.9800
C(34)-H(34C)	0.9800
C(32)-H(32A)	0.9800

C(32)-H(32B)	0.9800
C(32)-H(32C)	0.9800
C(19)-H(19A)	0.9800
C(19)-H(19B)	0.9800
C(19)-H(19C)	0.9800
C(31)-H(31A)	0.9800
C(31)-H(31B)	0.9800
C(31)-H(31C)	0.9800
C(36)-C(37)	1.514(7)
C(36)-H(36A)	0.9800
C(36)-H(36B)	0.9800
C(36)-H(36C)	0.9800
C(37)-C(42)	1.382(5)
C(37)-C(38)	1.384(5)
C(41)-C(40)	1.380(6)
C(41)-C(42)	1.386(6)
C(41)-H(41)	0.9500
C(40)-C(39)	1.387(5)
C(40)-H(40)	0.9500
C(42)-H(42)	0.9500
C(39)-C(38)	1.385(5)
C(39)-H(39)	0.9500
C(38)-H(38)	0.9500
C(36B)-C(42B)	1.520(11)
C(36B)-H(36D)	0.9800
C(36B)-H(36E)	0.9800
C(36B)-H(36F)	0.9800
C(37B)-C(42B)	1.357(13)
C(37B)-C(38B)	1.358(13)
C(37B)-H(37B)	0.9500
C(41B)-C(40B)	1.357(13)
C(41B)-C(42B)	1.361(13)
C(41B)-H(41B)	0.9500
C(40B)-C(39B)	1.357(13)
C(40B)-H(40B)	0.9500
C(39B)-C(38B)	1.356(13)
C(39B)-H(39B)	0.9500
C(38B)-H(38B)	0.9500
C(31B)-C(30B)	1.535(8)
C(31B)-H(31D)	0.9800
C(31B)-H(31E)	0.9800
C(31B)-H(31F)	0.9800
C(30B)-C(32B)	1.537(7)
C(30B)-H(30B)	1.0000
C(32B)-H(32D)	0.9800
C(32B)-H(32E)	0.9800

C(32B)-H(32F)	0.9800
As(1)#1-As(1)-Fe(1)	60.969(13)
As(1)#1-As(1)-Fe(1)#1	60.695(13)
Fe(1)-As(1)-Fe(1)#1	121.664(12)
N(2)-Fe(1)-N(1)	95.95(7)
N(2)-Fe(1)-As(1)	125.38(5)
N(1)-Fe(1)-As(1)	126.97(5)
N(2)-Fe(1)-As(1)#1	123.66(5)
N(1)-Fe(1)-As(1)#1	127.04(5)
As(1)-Fe(1)-As(1)#1	58.335(12)
C(2)-N(1)-C(24)	123.56(18)
C(2)-N(1)-Fe(1)	122.16(15)
C(24)-N(1)-Fe(1)	114.17(13)
C(4)-N(2)-C(12)	122.56(18)
C(4)-N(2)-Fe(1)	122.50(15)
C(12)-N(2)-Fe(1)	114.65(13)
C(13)-C(12)-C(17)	121.0(2)
C(13)-C(12)-N(2)	120.3(2)
C(17)-C(12)-N(2)	118.7(2)
N(1)-C(2)-C(3)	121.6(2)
N(1)-C(2)-C(1)	126.8(2)
C(3)-C(2)-C(1)	111.59(19)
N(2)-C(4)-C(3)	121.1(2)
N(2)-C(4)-C(5)	126.8(2)
C(3)-C(4)-C(5)	112.11(19)
C(25)-C(24)-C(29)	121.0(2)
C(25)-C(24)-N(1)	119.9(2)
C(29)-C(24)-N(1)	119.0(2)
C(2)-C(3)-C(4)	133.8(2)
C(2)-C(3)-H(3)	113.1
C(4)-C(3)-H(3)	113.1
C(14)-C(13)-C(12)	118.0(2)
C(14)-C(13)-C(21)	119.3(2)
C(12)-C(13)-C(21)	122.7(2)
C(26)-C(25)-C(24)	118.2(3)
C(26)-C(25)-C(33)	119.0(2)
C(24)-C(25)-C(33)	122.8(2)
C(16)-C(17)-C(12)	118.0(2)
C(16)-C(17)-C(18)	118.9(2)
C(12)-C(17)-C(18)	123.0(2)
C(8)-C(1)-C(7)	107.5(2)
C(8)-C(1)-C(6)	105.2(2)
C(7)-C(1)-C(6)	108.0(2)
C(8)-C(1)-C(2)	118.5(2)
C(7)-C(1)-C(2)	107.2(2)

C(6)-C(1)-C(2)	110.0(2)
C(15)-C(14)-C(13)	121.4(3)
C(15)-C(14)-H(14)	119.3
C(13)-C(14)-H(14)	119.3
C(28)-C(29)-C(24)	117.7(3)
C(28)-C(29)-C(30)	118.8(4)
C(24)-C(29)-C(30)	123.3(4)
C(28)-C(29)-C(30B)	121.9(6)
C(24)-C(29)-C(30B)	119.9(6)
C(16)-C(15)-C(14)	119.7(2)
C(16)-C(15)-H(15)	120.1
C(14)-C(15)-H(15)	120.1
C(27)-C(26)-C(25)	121.2(3)
C(27)-C(26)-H(26)	119.4
C(25)-C(26)-H(26)	119.4
C(11)-C(5)-C(10)	109.0(2)
C(11)-C(5)-C(9)	106.7(2)
C(10)-C(5)-C(9)	105.4(2)
C(11)-C(5)-C(4)	107.7(2)
C(10)-C(5)-C(4)	109.0(2)
C(9)-C(5)-C(4)	118.7(2)
C(15)-C(16)-C(17)	121.5(3)
C(15)-C(16)-H(16)	119.2
C(17)-C(16)-H(16)	119.2
C(28)-C(27)-C(26)	119.9(3)
C(28)-C(27)-H(27)	120.1
C(26)-C(27)-H(27)	120.1
C(5)-C(11)-H(11A)	109.5
C(5)-C(11)-H(11B)	109.5
H(11A)-C(11)-H(11B)	109.5
C(5)-C(11)-H(11C)	109.5
H(11A)-C(11)-H(11C)	109.5
H(11B)-C(11)-H(11C)	109.5
C(1)-C(6)-H(6A)	109.5
C(1)-C(6)-H(6B)	109.5
H(6A)-C(6)-H(6B)	109.5
C(1)-C(6)-H(6C)	109.5
H(6A)-C(6)-H(6C)	109.5
H(6B)-C(6)-H(6C)	109.5
C(25)-C(33)-C(34)	114.0(3)
C(25)-C(33)-C(35)	110.8(2)
C(34)-C(33)-C(35)	108.2(2)
C(25)-C(33)-H(33)	107.9
C(34)-C(33)-H(33)	107.9
C(35)-C(33)-H(33)	107.9
C(27)-C(28)-C(29)	121.6(3)

C(27)-C(28)-H(28)	119.2
C(29)-C(28)-H(28)	119.2
C(13)-C(21)-C(23)	111.5(2)
C(13)-C(21)-C(22)	112.6(3)
C(23)-C(21)-C(22)	108.0(2)
C(13)-C(21)-H(21)	108.2
C(23)-C(21)-H(21)	108.2
C(22)-C(21)-H(21)	108.2
C(5)-C(10)-H(10A)	109.5
C(5)-C(10)-H(10B)	109.5
H(10A)-C(10)-H(10B)	109.5
C(5)-C(10)-H(10C)	109.5
H(10A)-C(10)-H(10C)	109.5
H(10B)-C(10)-H(10C)	109.5
C(1)-C(7)-H(7A)	109.5
C(1)-C(7)-H(7B)	109.5
H(7A)-C(7)-H(7B)	109.5
C(1)-C(7)-H(7C)	109.5
H(7A)-C(7)-H(7C)	109.5
H(7B)-C(7)-H(7C)	109.5
C(33)-C(35)-H(35A)	109.5
C(33)-C(35)-H(35B)	109.5
H(35A)-C(35)-H(35B)	109.5
C(33)-C(35)-H(35C)	109.5
H(35A)-C(35)-H(35C)	109.5
H(35B)-C(35)-H(35C)	109.5
C(21)-C(23)-H(23A)	109.5
C(21)-C(23)-H(23B)	109.5
H(23A)-C(23)-H(23B)	109.5
C(21)-C(23)-H(23C)	109.5
H(23A)-C(23)-H(23C)	109.5
H(23B)-C(23)-H(23C)	109.5
C(1)-C(8)-H(8A)	109.5
C(1)-C(8)-H(8B)	109.5
H(8A)-C(8)-H(8B)	109.5
C(1)-C(8)-H(8C)	109.5
H(8A)-C(8)-H(8C)	109.5
H(8B)-C(8)-H(8C)	109.5
C(5)-C(9)-H(9A)	109.5
C(5)-C(9)-H(9B)	109.5
H(9A)-C(9)-H(9B)	109.5
C(5)-C(9)-H(9C)	109.5
H(9A)-C(9)-H(9C)	109.5
H(9B)-C(9)-H(9C)	109.5
C(29)-C(30)-C(32)	109.3(6)
C(29)-C(30)-C(31)	112.3(7)

C(32)-C(30)-C(31)	109.1(6)
C(29)-C(30)-H(30)	108.7
C(32)-C(30)-H(30)	108.7
C(31)-C(30)-H(30)	108.7
C(17)-C(18)-C(20)	110.4(3)
C(17)-C(18)-C(19)	112.5(3)
C(20)-C(18)-C(19)	109.2(3)
C(17)-C(18)-H(18)	108.2
C(20)-C(18)-H(18)	108.2
C(19)-C(18)-H(18)	108.2
C(21)-C(22)-H(22A)	109.5
C(21)-C(22)-H(22B)	109.5
H(22A)-C(22)-H(22B)	109.5
C(21)-C(22)-H(22C)	109.5
H(22A)-C(22)-H(22C)	109.5
H(22B)-C(22)-H(22C)	109.5
C(18)-C(20)-H(20A)	109.5
C(18)-C(20)-H(20B)	109.5
H(20A)-C(20)-H(20B)	109.5
C(18)-C(20)-H(20C)	109.5
H(20A)-C(20)-H(20C)	109.5
H(20B)-C(20)-H(20C)	109.5
C(33)-C(34)-H(34A)	109.5
C(33)-C(34)-H(34B)	109.5
H(34A)-C(34)-H(34B)	109.5
C(33)-C(34)-H(34C)	109.5
H(34A)-C(34)-H(34C)	109.5
H(34B)-C(34)-H(34C)	109.5
C(30)-C(32)-H(32A)	109.5
C(30)-C(32)-H(32B)	109.5
H(32A)-C(32)-H(32B)	109.5
C(30)-C(32)-H(32C)	109.5
H(32A)-C(32)-H(32C)	109.5
H(32B)-C(32)-H(32C)	109.5
C(18)-C(19)-H(19A)	109.5
C(18)-C(19)-H(19B)	109.5
H(19A)-C(19)-H(19B)	109.5
C(18)-C(19)-H(19C)	109.5
H(19A)-C(19)-H(19C)	109.5
H(19B)-C(19)-H(19C)	109.5
C(30)-C(31)-H(31A)	109.5
C(30)-C(31)-H(31B)	109.5
H(31A)-C(31)-H(31B)	109.5
C(30)-C(31)-H(31C)	109.5
H(31A)-C(31)-H(31C)	109.5
H(31B)-C(31)-H(31C)	109.5

C(37)-C(36)-H(36A)	109.5
C(37)-C(36)-H(36B)	109.5
H(36A)-C(36)-H(36B)	109.5
C(37)-C(36)-H(36C)	109.5
H(36A)-C(36)-H(36C)	109.5
H(36B)-C(36)-H(36C)	109.5
C(42)-C(37)-C(38)	119.4(3)
C(42)-C(37)-C(36)	120.3(5)
C(38)-C(37)-C(36)	120.2(5)
C(40)-C(41)-C(42)	120.2(4)
C(40)-C(41)-H(41)	119.9
C(42)-C(41)-H(41)	119.9
C(41)-C(40)-C(39)	119.6(4)
C(41)-C(40)-H(40)	120.2
C(39)-C(40)-H(40)	120.2
C(37)-C(42)-C(41)	120.3(4)
C(37)-C(42)-H(42)	119.9
C(41)-C(42)-H(42)	119.9
C(38)-C(39)-C(40)	120.0(4)
C(38)-C(39)-H(39)	120.0
C(40)-C(39)-H(39)	120.0
C(37)-C(38)-C(39)	120.3(4)
C(37)-C(38)-H(38)	119.8
C(39)-C(38)-H(38)	119.8
C(42B)-C(36B)-H(36D)	109.5
C(42B)-C(36B)-H(36E)	109.5
H(36D)-C(36B)-H(36E)	109.5
C(42B)-C(36B)-H(36F)	109.5
H(36D)-C(36B)-H(36F)	109.5
H(36E)-C(36B)-H(36F)	109.5
C(42B)-C(37B)-C(38B)	119.9(5)
C(42B)-C(37B)-H(37B)	120.0
C(38B)-C(37B)-H(37B)	120.0
C(40B)-C(41B)-C(42B)	119.9(6)
C(40B)-C(41B)-H(41B)	120.1
C(42B)-C(41B)-H(41B)	120.1
C(41B)-C(40B)-C(39B)	119.9(6)
C(41B)-C(40B)-H(40B)	120.0
C(39B)-C(40B)-H(40B)	120.0
C(37B)-C(42B)-C(41B)	119.9(5)
C(37B)-C(42B)-C(36B)	113.7(17)
C(41B)-C(42B)-C(36B)	126.4(17)
C(38B)-C(39B)-C(40B)	119.9(5)
C(38B)-C(39B)-H(39B)	120.0
C(40B)-C(39B)-H(39B)	120.0
C(39B)-C(38B)-C(37B)	120.1(5)

C(39B)-C(38B)-H(38B)	119.9
C(37B)-C(38B)-H(38B)	119.9
C(30B)-C(31B)-H(31D)	109.5
C(30B)-C(31B)-H(31E)	109.5
H(31D)-C(31B)-H(31E)	109.5
C(30B)-C(31B)-H(31F)	109.5
H(31D)-C(31B)-H(31F)	109.5
H(31E)-C(31B)-H(31F)	109.5
C(31B)-C(30B)-C(32B)	106.8(10)
C(31B)-C(30B)-C(29)	111.2(10)
C(32B)-C(30B)-C(29)	115.9(13)
C(31B)-C(30B)-H(30B)	107.5
C(32B)-C(30B)-H(30B)	107.5
C(29)-C(30B)-H(30B)	107.5
C(30B)-C(32B)-H(32D)	109.5
C(30B)-C(32B)-H(32E)	109.5
H(32D)-C(32B)-H(32E)	109.5
C(30B)-C(32B)-H(32F)	109.5
H(32D)-C(32B)-H(32F)	109.5
H(32E)-C(32B)-H(32F)	109.5

Symmetry transformations used to generate equivalent atoms:
#1 -x+1,-y+1,-z+1

Table S4. Anisotropic displacement parameters ($Å^2 x\ 10^3$) for **2**·2 tol. The anisotropic displacement factor exponent takes the form: $-2\pi^2[h^2a^{*2}U^{11} + \ldots + 2hka^*b^*U^{12}]$

	U^{11}	U^{22}	U^{33}	U^{23}	U^{13}	U^{12}
As(1)	37(1)	24(1)	24(1)	3(1)	3(1)	3(1)
Fe(1)	20(1)	21(1)	25(1)	5(1)	5(1)	1(1)
N(1)	21(1)	25(1)	26(1)	3(1)	7(1)	0(1)
N(2)	20(1)	27(1)	24(1)	3(1)	5(1)	3(1)
C(12)	18(1)	33(1)	29(1)	7(1)	6(1)	2(1)
C(2)	31(1)	21(1)	24(1)	0(1)	8(1)	-1(1)
C(4)	27(1)	26(1)	25(1)	2(1)	4(1)	5(1)
C(24)	24(1)	25(1)	32(1)	8(1)	6(1)	-3(1)
C(3)	31(1)	26(1)	25(1)	7(1)	4(1)	2(1)
C(13)	25(1)	41(1)	30(1)	7(1)	1(1)	-4(1)
C(25)	28(1)	41(1)	35(1)	14(1)	11(1)	5(1)
C(17)	37(1)	38(1)	36(1)	0(1)	13(1)	2(1)
C(1)	36(1)	26(1)	34(1)	7(1)	10(1)	-4(1)
C(14)	26(1)	56(2)	40(2)	10(1)	3(1)	-11(1)
C(29)	31(1)	27(1)	50(2)	4(1)	-2(1)	-5(1)
C(15)	25(1)	63(2)	42(2)	15(1)	12(1)	1(1)
C(26)	26(1)	57(2)	54(2)	20(1)	14(1)	10(1)
C(5)	28(1)	38(1)	42(1)	12(1)	5(1)	9(1)
C(16)	37(2)	49(2)	38(2)	3(1)	18(1)	7(1)
C(27)	22(1)	65(2)	71(2)	25(2)	-2(1)	-6(1)
C(11)	37(2)	64(2)	45(2)	12(1)	-9(1)	8(1)
C(6)	48(2)	28(1)	77(2)	10(1)	14(2)	-2(1)
C(33)	43(2)	57(2)	31(1)	2(1)	9(1)	22(1)
C(28)	33(2)	43(2)	65(2)	9(1)	-11(1)	-13(1)
C(21)	44(2)	55(2)	37(2)	-4(1)	8(1)	-22(1)
C(10)	45(2)	38(2)	62(2)	10(1)	6(1)	18(1)
C(7)	73(2)	62(2)	31(2)	6(1)	19(1)	-24(2)
C(35)	44(2)	50(2)	46(2)	0(1)	10(1)	9(1)
C(23)	45(2)	53(2)	60(2)	-12(2)	2(1)	-12(1)
C(8)	34(2)	45(2)	66(2)	28(1)	11(1)	-9(1)
C(9)	29(1)	64(2)	70(2)	30(2)	8(1)	19(1)
C(30)	38(4)	45(3)	55(3)	-17(3)	-9(4)	-6(3)
C(18)	68(2)	62(2)	50(2)	-23(2)	36(2)	-25(2)
C(22)	102(3)	68(2)	42(2)	6(2)	-23(2)	-26(2)
C(20)	41(2)	79(2)	85(3)	-48(2)	9(2)	-2(2)
C(34)	133(4)	63(2)	45(2)	13(2)	40(2)	40(2)
C(32)	50(4)	48(4)	57(4)	-21(3)	23(3)	-12(3)
C(19)	149(4)	46(2)	51(2)	-9(2)	19(2)	-3(2)
C(31)	105(6)	34(2)	62(3)	-15(2)	6(3)	6(3)
C(36)	68(4)	103(4)	87(3)	31(3)	12(3)	-22(3)

C(37)	36(3)	61(3)	59(2)	17(2)	-2(2)	3(2)
C(41)	71(6)	85(4)	47(2)	7(3)	-14(3)	12(4)
C(40)	76(4)	72(3)	52(3)	30(2)	15(3)	13(3)
C(42)	46(4)	55(3)	71(3)	8(2)	-13(3)	4(3)
C(39)	50(4)	57(3)	67(3)	18(2)	6(2)	3(2)
C(38)	34(3)	68(2)	49(2)	5(2)	3(2)	-3(2)
C(36B)	34(7)	130(10)	98(11)	19(8)	-23(7)	4(7)
C(37B)	34(8)	119(11)	87(9)	26(7)	-10(7)	42(8)
C(41B)	53(10)	100(10)	68(9)	23(7)	-24(7)	27(7)
C(40B)	56(11)	118(10)	84(11)	9(9)	-34(9)	7(9)
C(42B)	41(9)	106(10)	79(9)	27(7)	-19(7)	32(7)
C(39B)	67(13)	119(12)	99(13)	-1(9)	-22(11)	22(9)
C(38B)	53(12)	136(13)	98(10)	4(8)	-13(8)	34(10)
C(31B)	78(9)	37(4)	52(5)	-1(3)	8(5)	18(5)
C(30B)	38(7)	27(4)	39(5)	-14(4)	5(4)	6(4)
C(32B)	68(8)	45(7)	43(5)	-7(5)	-8(5)	4(6)

Characterization of FeAs and films deposited on NF

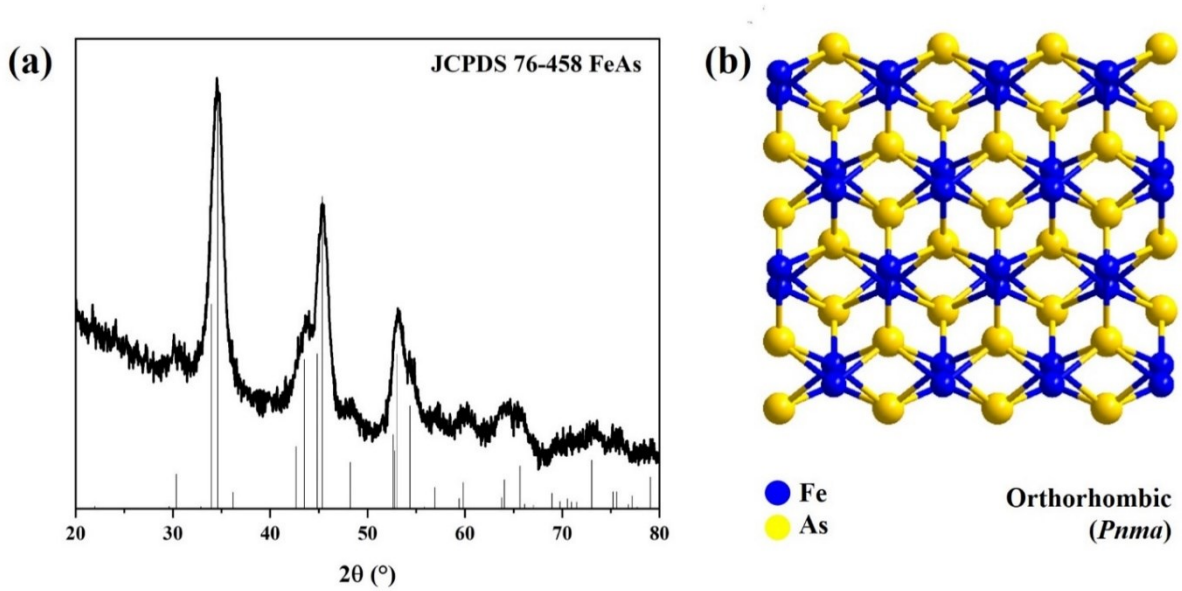

Figure S3. (a) Powder X-ray diffraction (XRD) pattern of FeAs prepared by hot injection. The obtained diffractogram reveals reflections matching the FeAs phase (JCPDS 76-458). The crystallinity of the material was additionally confirmed by the selected area diffraction pattern (SAED). Moreover, the composition of the material was confirmed by EDX, XPS and ICP-AES analysis. (b) The solid state crystal structure of FeAs (JCPDS 76-458) belongs to the MnP structure type (orthorhombic, *Pnma* (62) space group, with lattice parameters a = 5.442 Å and c = 3.3727 Å).[23–25]

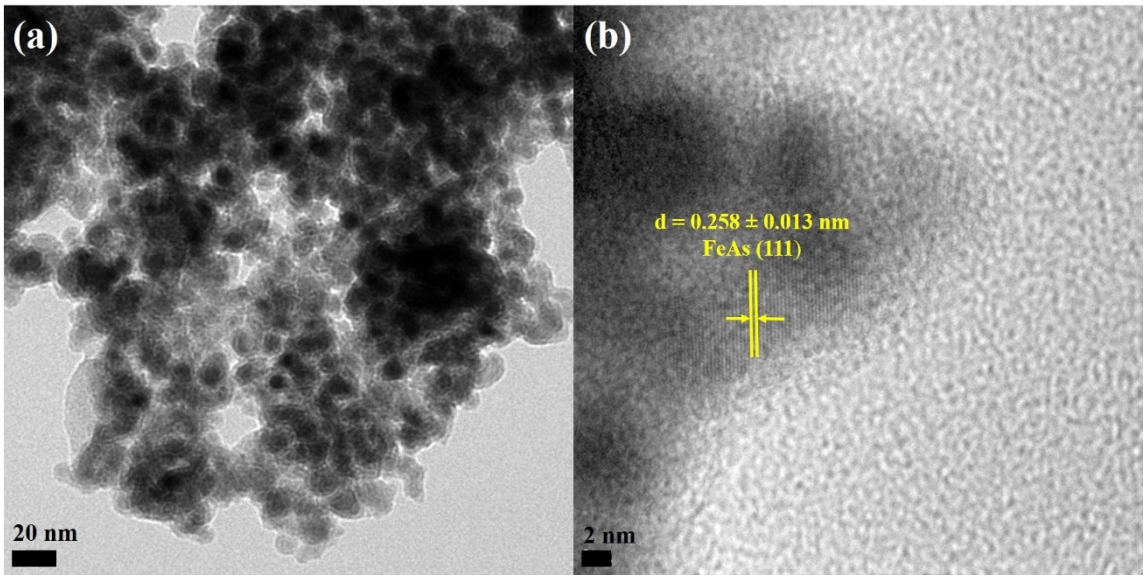

Figure S4. TEM image of (a) aggregated FeAs nanoparticles (~10nm size) and (b) high-resolution (HR)-TEM image showing the crystalline fringes associated to a lattice spacing of 0.258 ± 0.013 nm corresponding to the (111) plane of the FeAs phase.

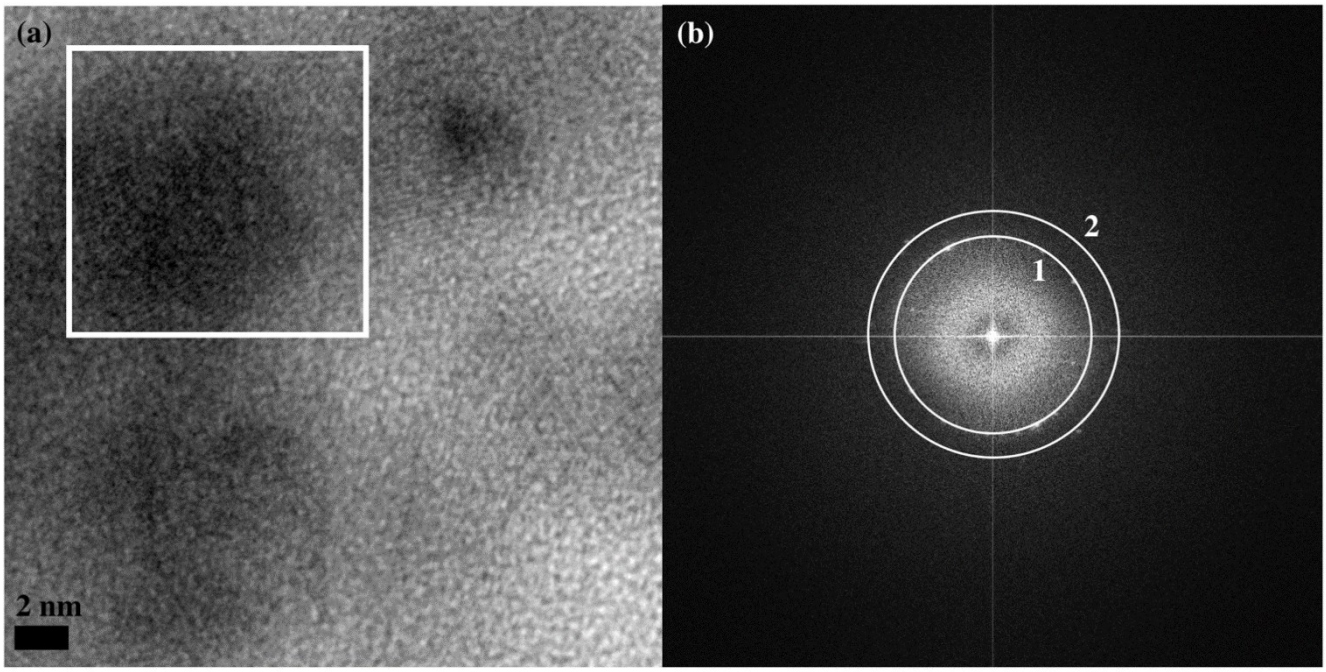

Figure S5. (a) HR-TEM image of FeAs particles with white framed areas containing lattice fringes and its respective (b) Fourier transform (FT) revealing the lattice distances 0.255 ± 0.004 nm (ring marked with 1) and 0.199 ± 0.001 nm (ring marked with 2) indicating the FeAs crystallographic planes (111) and (211), respectively (JCPDS 76-458).

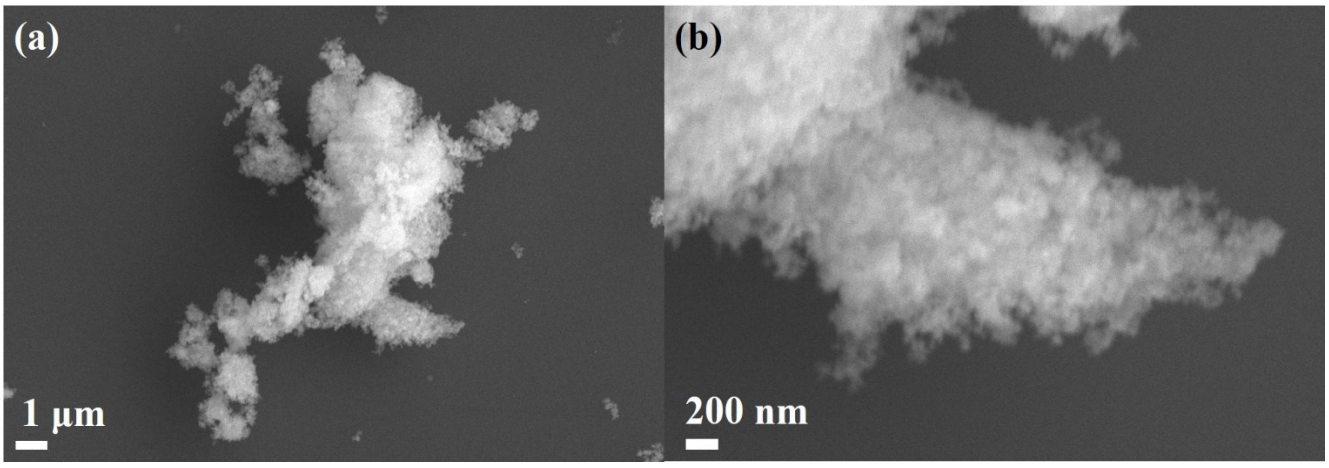

Figure S6. SEM images showing agglomerations of particles of FeAs at (a) 5000x and (b) 25000x.

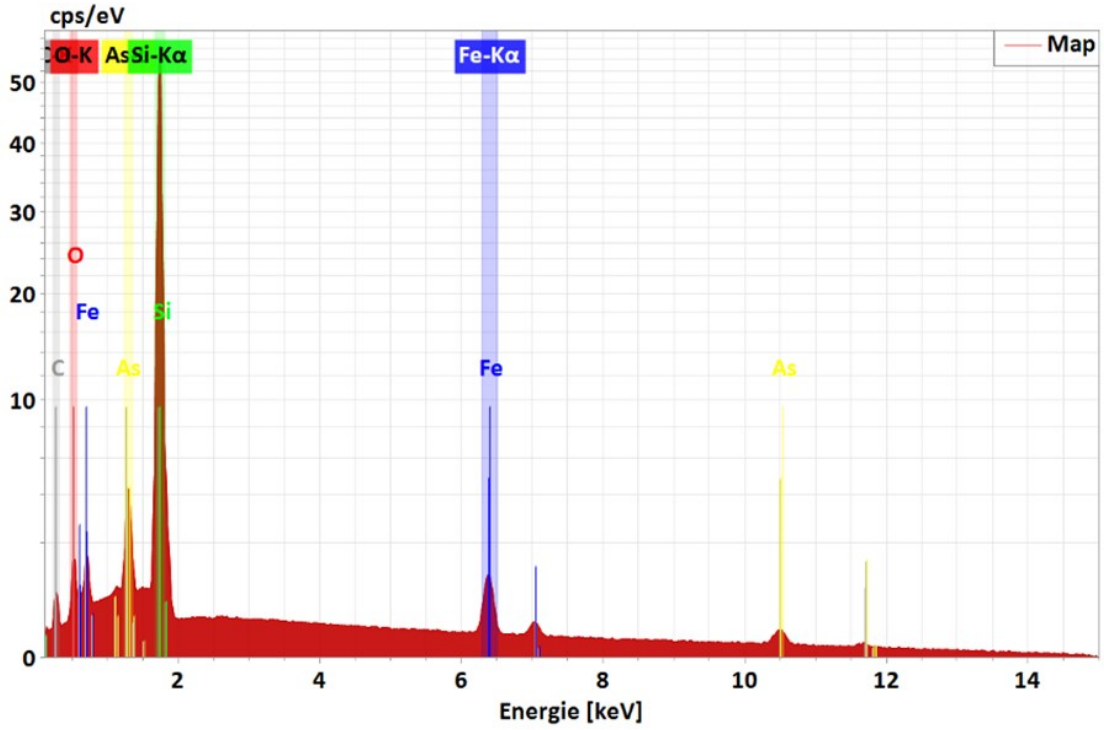

Figure S7. SEM-EDX of FeAs prepared by hot injection which confirms the presence of Fe and As. The presence of O is inevitable due to surface passivation. The presence of Si peaks arises from the Si wafer support used in SEM. The determined Fe:As ratio was 1:1.12.

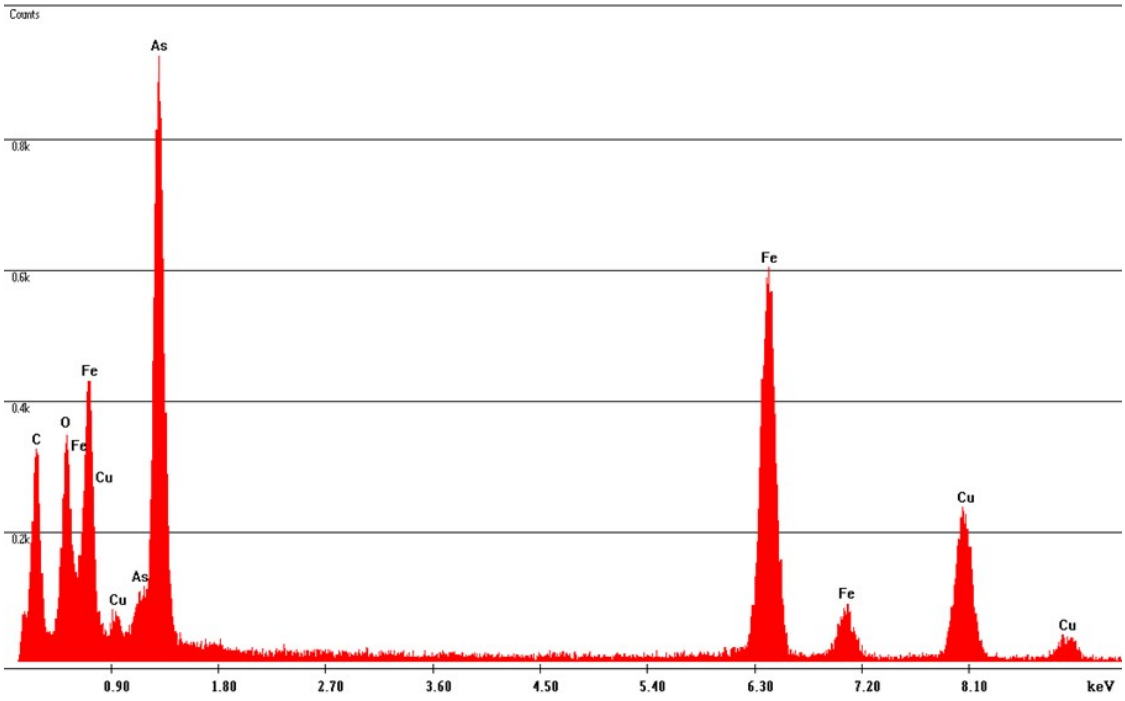

Figure S8. TEM-EDX of FeAs prepared through hot injection, which confirms the presence of Fe and As. The presence of Cu peaks arises from the TEM grid (carbon film on 300 mesh Cu-grid). The determined Fe:As ratio was 1:0.82.

Table S5. Determination of the Fe and As content in the prepared FeAs by ICP-AES, EDX-SEM, and EDX-TEM. The average value of three independent measurements is shown.

Fe:As (ICP-AES)	Fe:As (EDX-SEM)	Fe:As (EDX-TEM)
1:1.04 ± 0.04	1:1.12 ± 0.07	1:0.82*

*no error is presented because only one EDX measurement were performed.

Table S6. Determination of C, H and O content by elemental analysis. The presence of C, H, and N arises from the L^B ligand of the precursor.

%C	%H	%N
5.038 ± 0.022	0.479 ± 0.003	0.009 ± 0.001

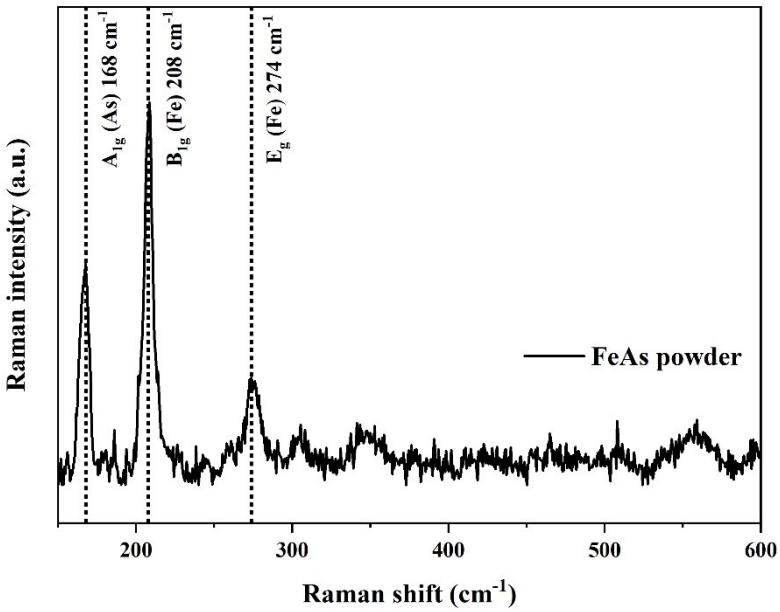

Figure S9. (Resonance) Raman spectra of FeAs powder. The shown bands match with the reported bands for bulk and FeAs nanoparticles[26] and can be assigned to the following phonon modes: low-frequency A_{1g} of As (168 cm^{-1}), B_{1g} of Fe (208 cm^{-1}) and high-frequency E_g of Fe (274 cm^{-1}).[27,28] Small deviations from reported values can be caused by thermal effects or laser power.

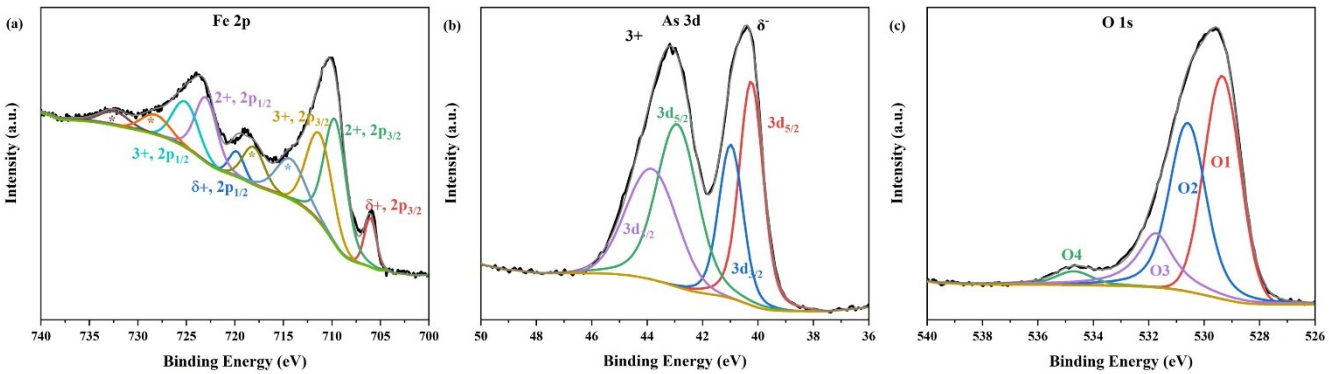

Figure S10. Deconvoluted XPS of FeAs: (a) Fe 2p, (b) As 3d and (c) O 1s. The Fe 2p deconvoluted spectrum shows the two peaks for $Fe^{\delta+}$ at $2p_{3/2}$ 705.9 eV and $2p_{1/2}$ 719.0 eV,[29] and peaks associated to Fe^{2+} ($2p_{3/2}$ 709.8 eV and $2p_{1/2}$ 723.1 eV) and Fe^{3+} ($2p_{3/2}$ 711.5 eV and $2p_{1/2}$ 725.3 eV), and two pairs of satellites of Fe^{2+} ($2p_{3/2}$ 714.5 eV and $2p_{1/2}$ 718.2 eV) and Fe^{3+} ($2p_{3/2}$ 728.5 eV and $2p_{1/2}$ 732.7 eV). The presence of peaks for $Fe^{\delta+}$ confirms the formation of FeAs, while the oxidized Fe peaks originated from the contact of the material with air. The As 3d deconvoluted spectrum shows two peaks, one related to $As^{\delta-}$ present in FeAs (40.4 eV) and oxidized As^{3+} (43.2 eV).[30,31] Each peak is deconvoluted into two peaks due to spin-orbital coupling, giving rise to 40.3 eV ($3d_{5/2}$) and 41.0 eV ($3d_{3/2}$) for the $As^{\delta-}$, and 42.3 eV ($3d_{5/2}$) and 43.4 eV ($3d_{3/2}$) for the As^{3+}. The O 1s deconvoluted spectrum shows four peaks related to products derived from air exposure: Fe-O (O1, 529.4 eV)[32] and As-O (O2, 530.6 eV).[30,31] The peaks at higher binding energy (O3, 531.8 eV and O4, 534.7 eV) are associated with hydroxylation and adsorbed water on the surface.[32]

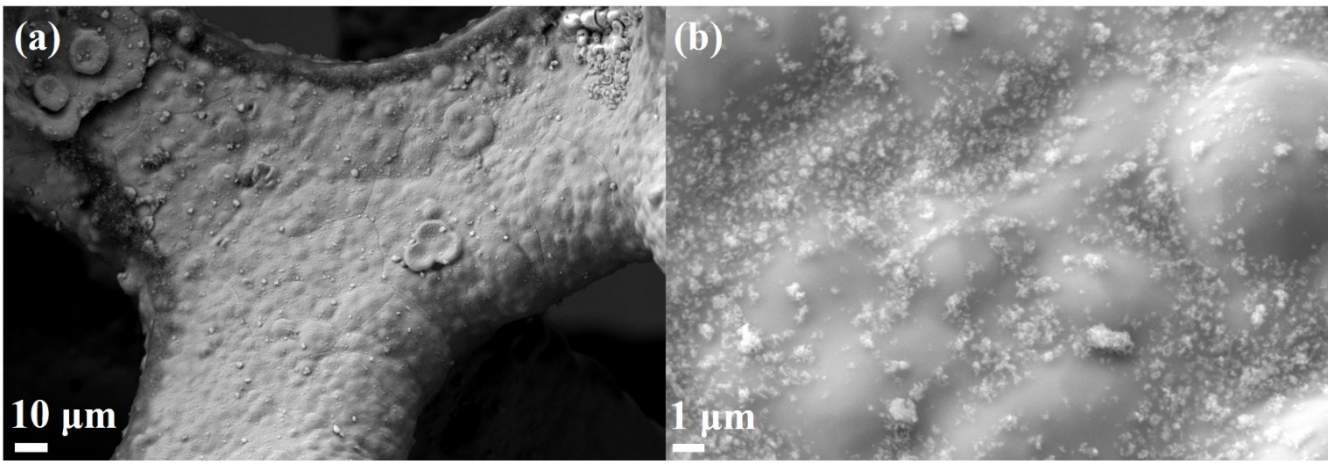

Figure S11. SEM of the FeAs films deposited on NF at (a) 500x and (b) 5000x. The high magnification image shows that the morphology of the FeAs particles is maintained (compare to as prepared FeAs SEM in Figure S6).

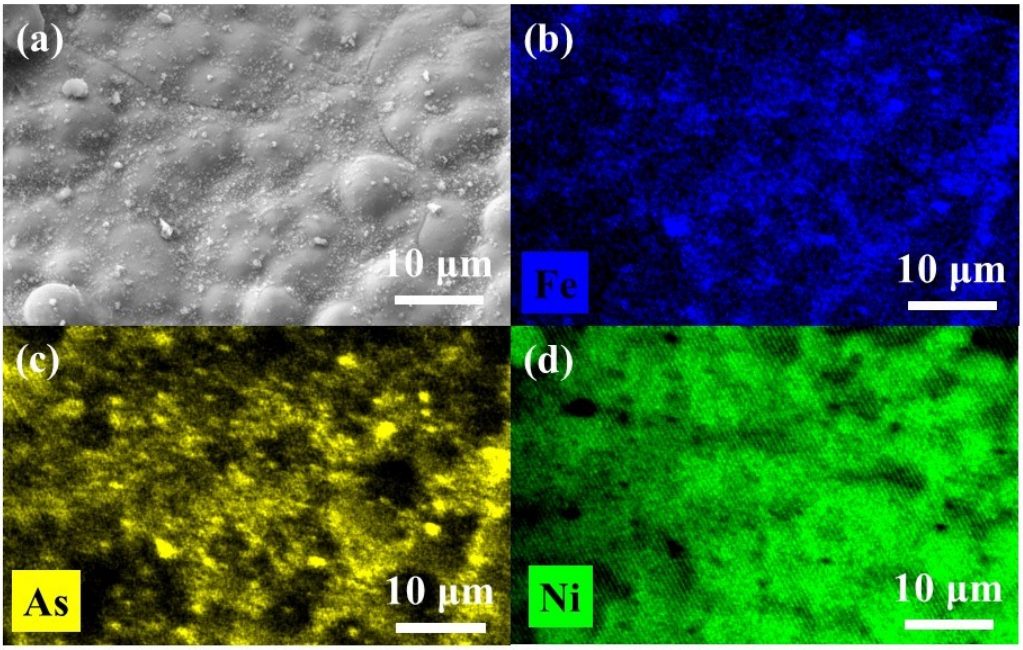

Figure S12. (a) SEM of FeAs/NF and elemental mapping of (b) Fe (blue), (c) As (yellow) and (d) Ni (green). Ni arises from the NF substrate. Homogenous distribution of Fe and As was observed in the particles deposited on NF.

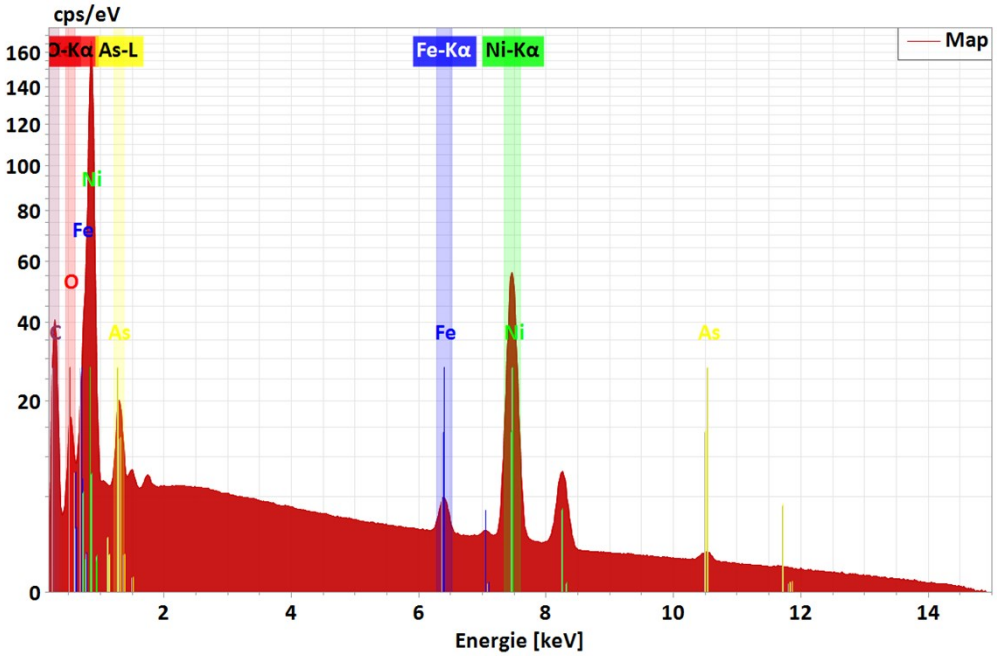

Figure S13. SEM-EDX of the film of FeAs/NF which confirmed the presence of Fe and As. The presence of Ni peaks arises from the NF substrate. The peaks between 1.5-2 keV correspond to Al ($K\alpha_1$, $K\alpha_2$ at 1.487 keV, 1.486 keV and K β_1 at 1.557 keV) and Si ($K\alpha_1$, $K\alpha_2$ at 1.740 keV, 1.739 keV and K β_1 at 1.836 keV); they arise from the Al sample holder and the Si wafer used during the measurement, respectively. The Fe:As ratio was ~1:1 as determined by SEM-EDX.

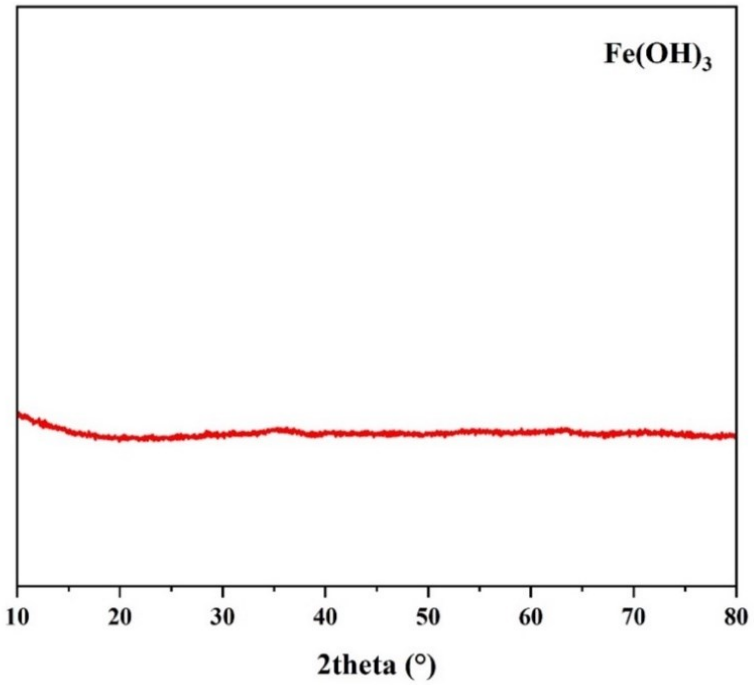

Figure S14. XRD patterns of the prepared $Fe(OH)_3$. The obtained material was amorphous. [11]

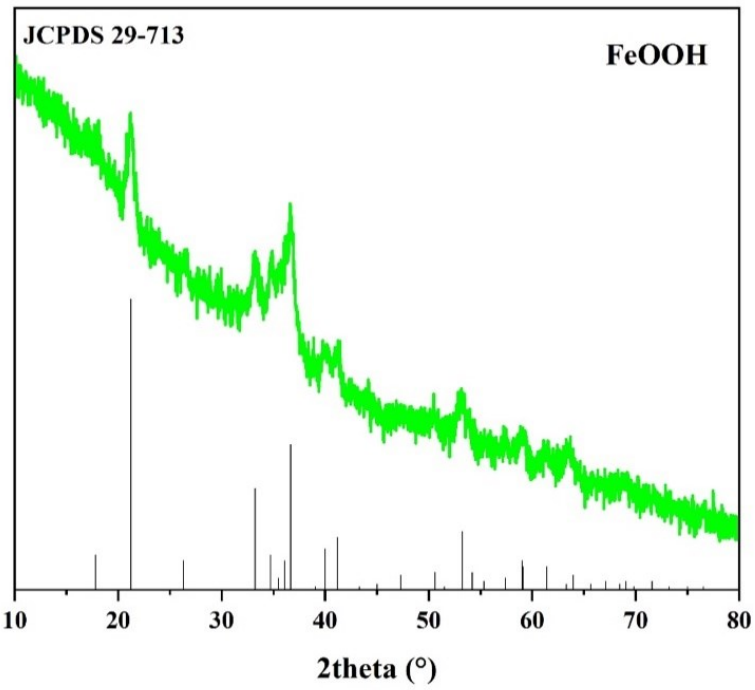

Figure S15. XRD patterns of the prepared FeOOH and its comparison to the diffraction peaks observed for α-FeOOH (goethite, JCPDS 29-713).

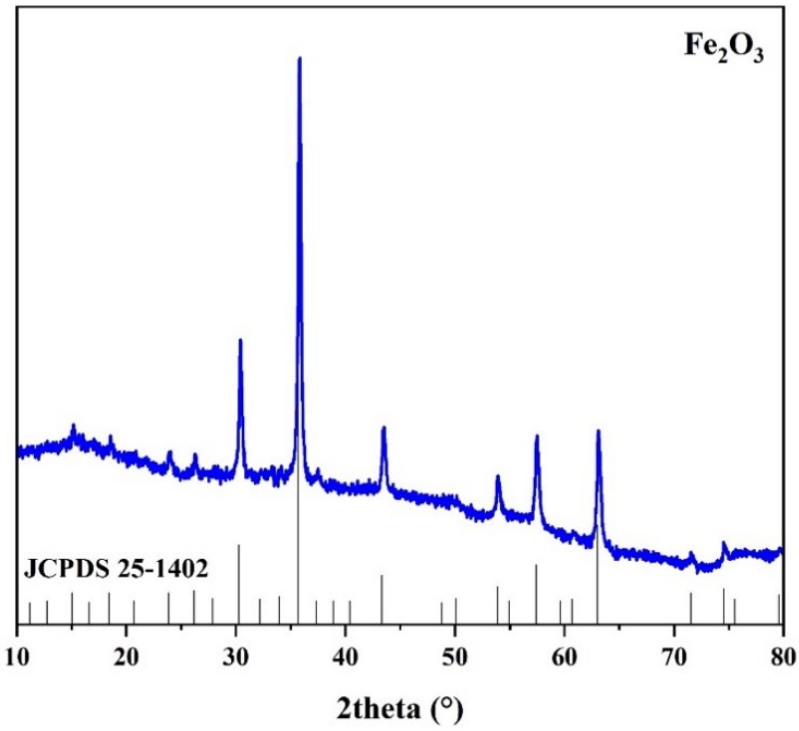

Figure S16. XRD patterns of the prepared Fe_2O_3 and its comparison to the diffraction peaks observed for Fe_2O_3 (maghemite, JCPDS 25-1402).

Electrochemical experiments of films deposited on NF

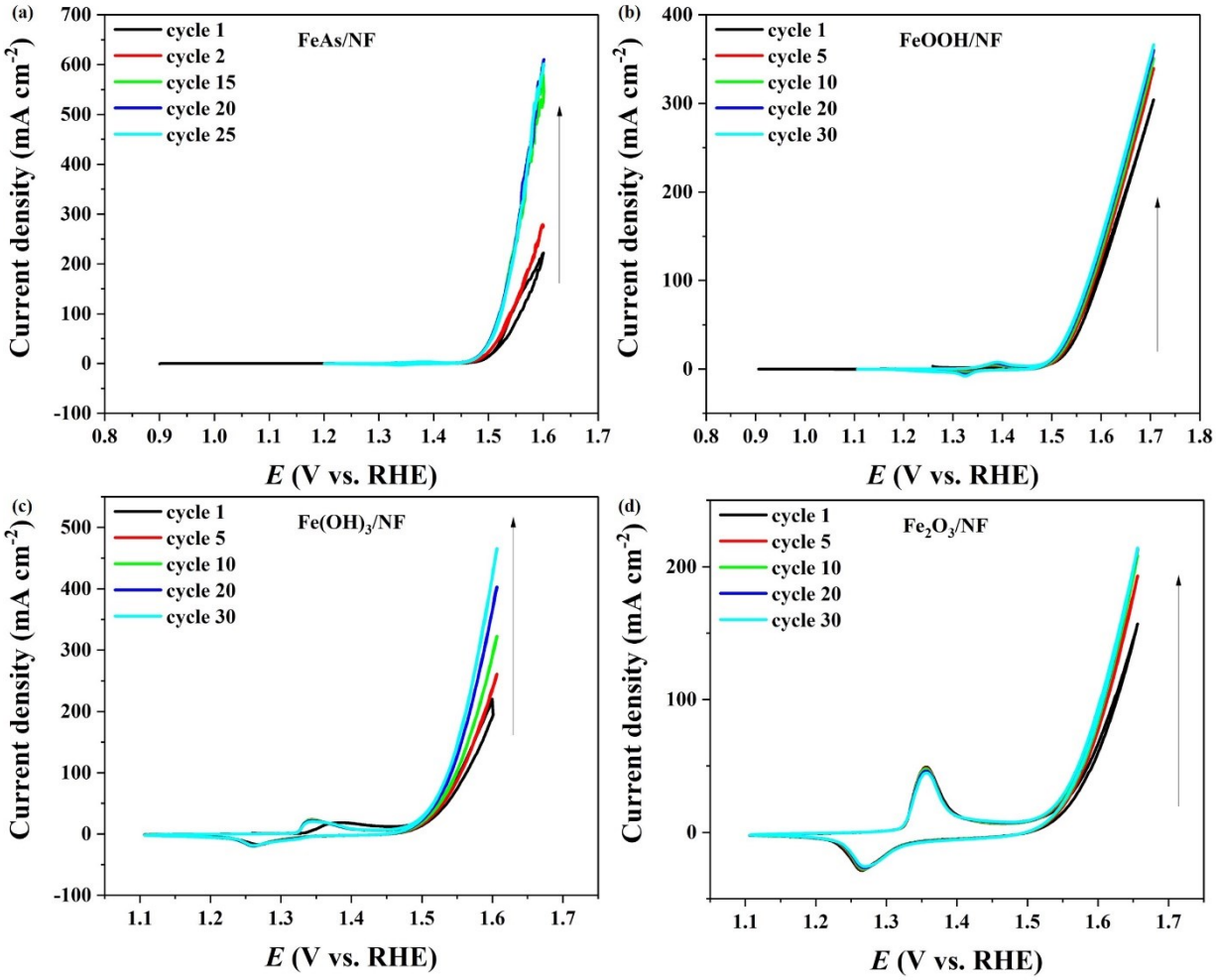

Figure S17. Activation of the (a) FeAs/NF, (b) $Fe(OH)_3$/NF, (c) FeOOH/NF, and (d) Fe_2O_3/NF by CV in 1 M KOH (5 mV s^{-1}).

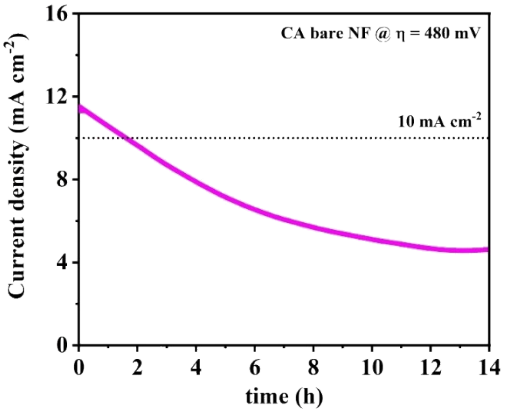

Figure S18. CA at η = 480 ± 5 mV (1.71 V vs. RHE, 0.81 V vs. Hg/HgO) of bare NF.

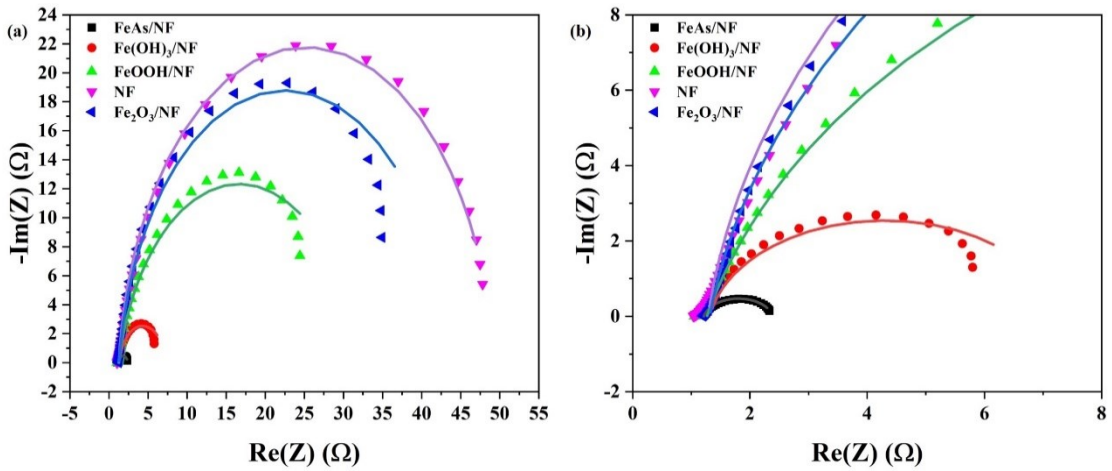

Figure S19. (a) Nyquist plot constructed from the EIS experiment of materials deposited on NF. The spectra were collected with an anodic polarization potential of 1.51 V vs RHE. (b) Zoom of the Nyquist plot. The continuous lines show the fitting to the circuit which contains two resistors R_1 and R_2 and Q a constant phase element (CPE) (Figure 3c). This circuit has been previously used to fit transition metal-based systems during OER reaction conditions.[33-36] The assignment of the elements is consistent in the literature and can be applied to our system: R_1 is the ohmic resistance of the solution and electrode (R_s), R_2 is the charge transfer resistance (R_{ct}), and a constant phase element (CPE, Q_2). We have used this model because it is the simplest model with which we could simulate our impedance spectra fairly well. When we used an ideal capacitor instead of a CPE, no reasonable simulation was possible. Inhomogeneities in the surface of the electrodes result in non-ideal capacitance in the double layer (C_{dl}) at the solid/electrolyte interface.[34] Therefore, we have considered this model that includes a CPE rather than a capacitor (C). Q represents the value of a non-ideal capacitor and has units of $F \times s^{(a_2 - 1)}$, where a_2 is an ideality factor which ranges from 0 to 1. When $a_2 = 1$ the interface is said to behave as an ideal capacitor ($Q = C_{dl}$). Normally, a_2 is found in the range 0.8-1 and indicates non-ideal behavior due to surface roughness and irregularities in surface termination, porosity, and complexity in the double-layer structure. Therefore, C_{dl} values are not possible to be derived from this model and compare them to the results obtained from the voltammetric data.[34]

Table S7. R_2 (Ω) (R_{ct}), R_1 (Ω) (R_s), Q ($F \times s^{(a_2 - 1)}$) and a_2 of FeAs, $Fe(OH)_3$, FeOOH, and Fe_2O_3 deposited on NF and its comparison to the bare NF substrate.

Material	R_{ct} **(Ω)**	R_s **(Ω)**	Q ($F \times s^{(a_2 - 1)}$)	a_2
NF	48.0 ± 1.2	1.3 ± 0.3	$1.5 \times 10^{-1} \pm 1.4 \times 10^{-2}$	$9.4 \times 10^{-1} \pm 6.6 \times 10^{-2}$
FeAs/NF	1.2 ± 0.4	1.2 ± 0.1	$1.9 \times 10^{-1} \pm 2.0 \times 10^{-2}$	$8.6 \times 10^{-1} \pm 1.0 \times 10^{-2}$
$Fe(OH)_3$/NF	6.0 ± 4.3	1.3 ± 0.7	$8.7 \times 10^{-2} \pm 1.3 \times 10^{-3}$	$8.9 \times 10^{-1} \pm 9.9 \times 10^{-2}$
FeOOH/NF	30.8 ± 3.2	1.3 ± 0.6	$6.2 \times 10^{-3} \pm 1.3 \times 10^{-3}$	$8.6 \times 10^{-1} \pm 5.6 \times 10^{-2}$
Fe_2O_3/NF	42.4 ± 3.1	1.3 ± 0.3	$5.7 \times 10^{-3} \pm 8.2 \times 10^{-4}$	$9.2 \times 10^{-1} \pm 6.2 \times 10^{-2}$

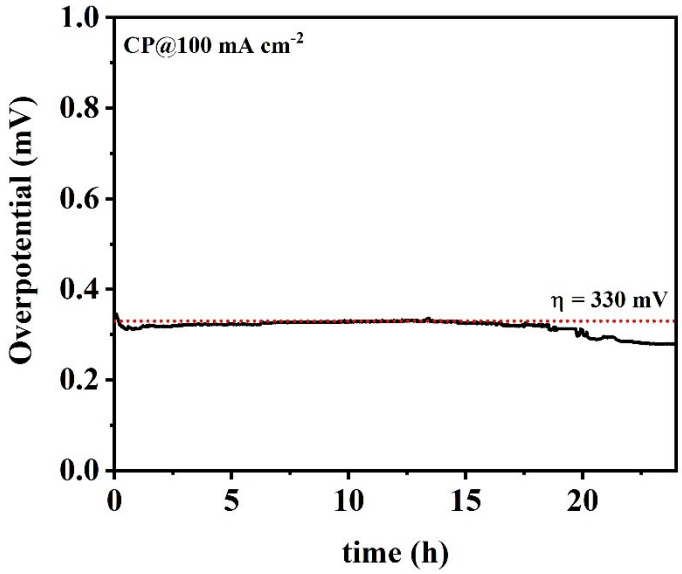

Figure S20. CP of FeAs/NF (1 mg cm^{-2}) at 100 mA cm^{-2}.

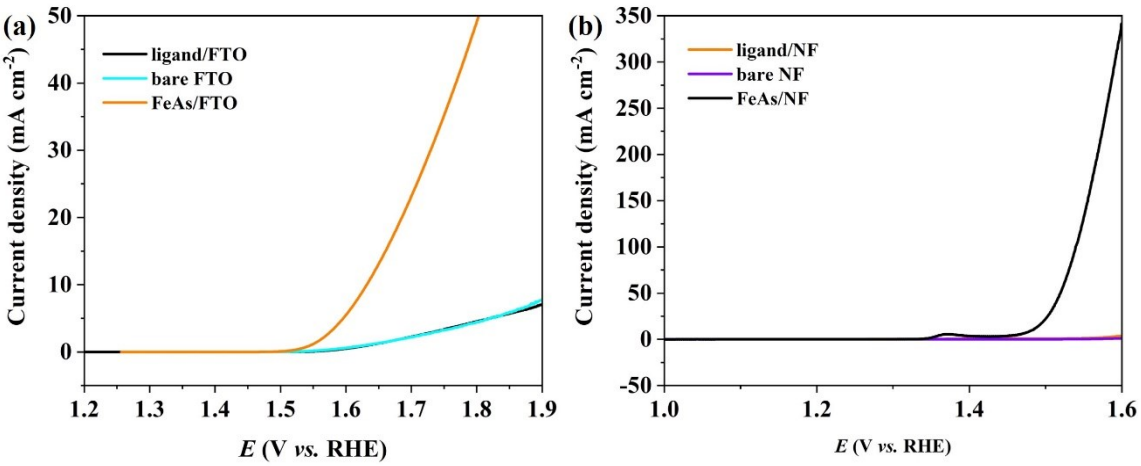

Figure S21. Electrochemical activity of films prepared from the β-diketiminato ligand deposited on (a) FTO and (b) NF compared to the FeAs and the bare substrate.

Calculation of Faradaic efficiency for OWS

The Faradaic efficiency (FE) towards OER in 1 M KOH was measured in a two-electrode configuration where FeAs/NF was used as anode and Pt as the cathode in a closed electrochemical cell. The two electrodes were placed on the same compartment of the electrochemical cell. The electrolyte and cell were first degassed with argon (Ar) for 1 hour under constant stirring. Afterward, a constant current density of 50 mA cm^{-2} was applied for a specified period. At the end of electrolysis, the gaseous samples were drawn from the headspace by a gas-tight syringe and analyzed by a GC calibrated for H_2 and O_2. Each injection was repeated at least three times, and the average value is presented. The FE is calculated based on:

$$FE(H_{2,\%}) = \frac{V_{H_2} \times 2 \times F}{V_m \times j \times t} \times 100\%$$

$$FE(O_{2,\%}) = \frac{V_{O_2} \times 4 \times F}{V_m \times j \times t} \times 100\%$$

V_{H2} and V_{O2} are the evolved volume of hydrogen and oxygen, F is the Faraday constant (96485.33289 C mol^{-1}), V_m is the molar volume of the gas, j is the current density and t is the time period of electrolysis (360 s).

A similar experiment was done at 100 mA cm^{-2}. The FeAs/NF was activated previous to the FE measurement by CV (1.2-1.7 V vs. RHE) for 2 h, which resulted in an increase of the FE.

The value of the FE relative to Pt can also be calculated, as Pt is known to show 100% of FE for H_2.[37-38] The value of FE is:

$$FE(O_{2,\%}) = \frac{V_{O_2}}{\frac{V_{H_2}}{2}} \times 100\%$$

Table S8. Calculation of Faradaic efficiency for FeAs/NF.

j (mA cm^{-2})*	t (s)	V_{H_2}(mL)	V_{O_2} (mL)	V_{H_2}:V_{O_2}	FE (H_2, %)	FE (O_2, %)	FE O_2 (rel. to H_2)**
49.39	360	2.15 ± 0.08	1.06 ± 0.04	2.01 ± 0.00	95 ± 3%	94 ± 3%	99% ± 1%
99.28	360	4.32 ± 0.07	2.14 ± 0.02	2.02 ± 0.01	97 ± 2%	96 ± 1%	99% ± 1%

*j (mA cm^{-2}) corresponds tot he actual current density measured during the CP experiment.
**the FE of O_2 relative to H_2 was calculated assuming 100% of FE for H_2 with Pt

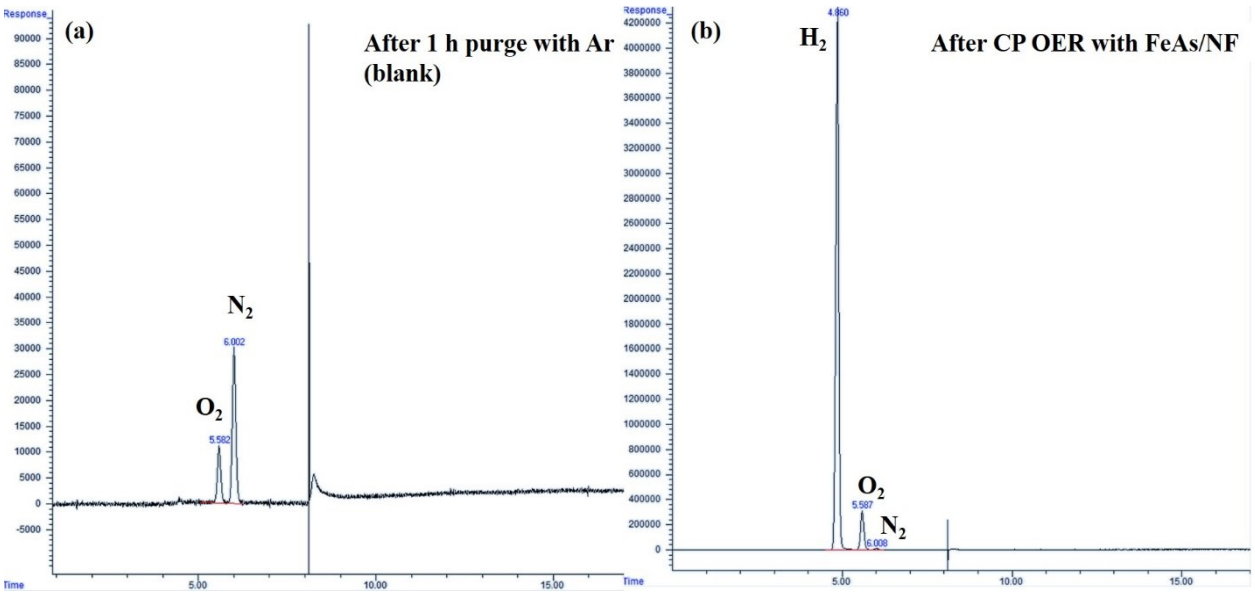

Figure S22. (a) Chromatogram obtained after 1 h purge with Ar. Remnants of air (O_2 and N_2) are detected. These detected quantities are used for de the calibration. (b) Chromatogram after CP OER 100 mA cm^{-2} for 360 s using FeAs/NF as anode and Pt rod as the cathode in a closed single-compartment electrochemical cell. H_2 and O_2 are produced from the electrolysis of water, N_2 (trace) is also present.

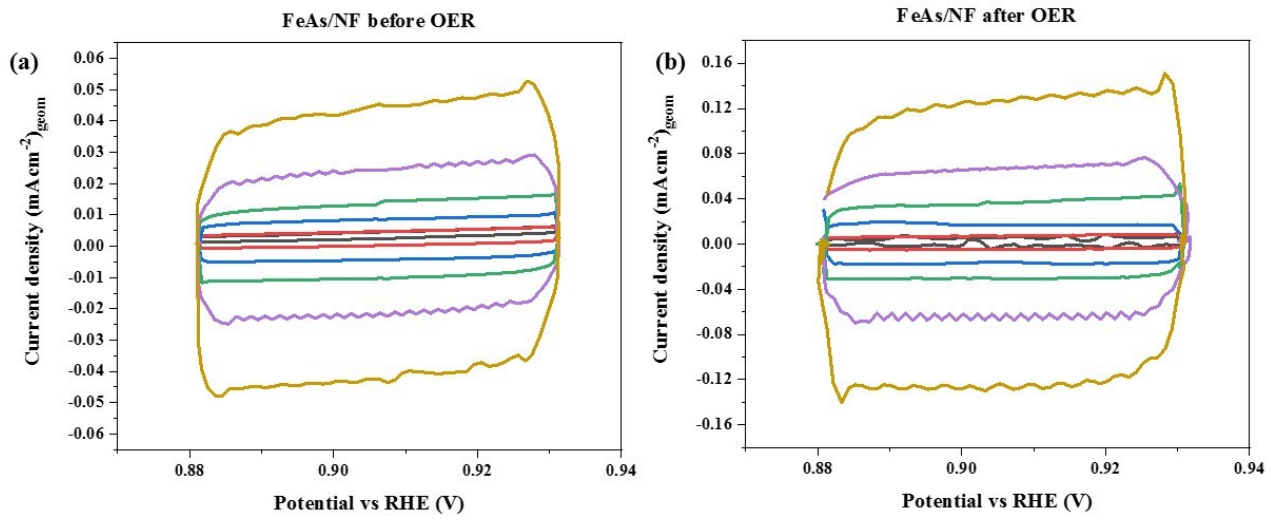

Figure S23. CV measurements at a non-faradaic process region at different scan rates for (a) FeAs/NF and (b) FeAs/NF after OER (CP OER 24h). Scan rates: 5 mVs^{-1} (black), 10 mVs^{-1} (red), 25 mVs^{-1} (blue), 50 mVs^{-1} (green), 100 mVs^{-1} (purple), 200 mVs^{-1} (dark yellow). The double-layer capacitance (C_{dl}) was determined as half of the slope from the plot of the capacitive current vs. scan rate plot (Figure S24). The value of C_{dl} is proportional to the ECSA.

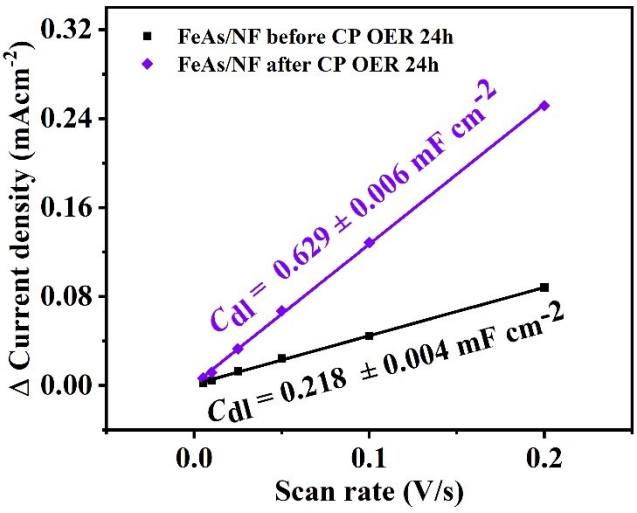

Figure S24. Difference in anodic and cathodic current density at the center of the potential range of the CVs measured at different scan rates (Figure S23). The value of C_{dl} is obtained from half of the slope of the graphs. After OER, there is an increase in ca. 3 times of the C_{dl}, suggesting the possibility of formation of surface defects as noted for non-oxidic materials during OER.[10,39,40]

Table S9. Activity comparison of the as-prepared FeAs and reference Fe-based materials with other highly efficient Fe-based pnictides in 1 M KOH for OER.

Catalyst	Current density ($mA\ cm^{-2}$)	Overpotential η (mV)	Reference
FeAs/NF	10	252 ± 3	This work
	100	309 ± 4	This work
FeAs/FTO	10	395 ± 6	This work
$Fe(OH)_3$/NF	10	275 ± 4	This work
	100	333 ± 3	This work
$Fe(OH)_3$/FTO	10	577 ± 3	This work
FeOOH/NF	10	283 ± 2	This work
	100	364 ± 3	This work
FeOOH/FTO	10	609 ± 5	This work
Fe_2O_3/NF	10	312 ± 4	This work
	100	397 ± 3	This work
Fe_2O_3/FTO	10	639 ± 5	This work
NF	10	480 ± 5	This work
$NiFeO_x$	10	350	[15]
NiAs/GC	10	360	[40]
FeP/NF	10	227	[41]
FeP/carbon fiber	10	290	[42]
FeP rGO/carbon fiber	10	260	[42]
Amorphous NiFe-OH-F/NF	10	220	[43]
FeMnP	10	250	[44]
FeP nanotubes/CC	10	288	[45]
FeP ultra small nanoparticles/Au @Au	10	320	[42]
FeP–rGO (50 : 50)@Au	10	290	[42]
FeMnP	10	250	[46]
Ultrathin FeOOH nanosheets	10	428	[47]
Ultrathin Ni-FeOOH nanosheets	10	274	[47]
FeS/IF	10	238	[48]
FeB_2	10	296	[49]
FeOOH/GC	10	530	[50]
FeOOH/NF	10	290	[51]
FeOOH nanosheet/NF	10	390	[52]
RGO/Ni-FeOOH/FTO	10	260	[53]
Fe_2O_3 hollow nanmorod/CNT/GC	10	383	[54]
γ-Fe_2O_3-CNT/GC	10	340	[55]
CNT@FeOOH sheet/CC	10	250	[56]
Fe@C-NG/NCNTs/GC	10	450	[57]
FeP nanorods/CP	10	350	[58]
FeP@RGO (50:50)/CP	10	290	[59]
Fe_xN/graphene-NF	10	238	[60]
Fe_7S_8 nanosheets/GC	10	270	[61]

$FeSe_2$ nanoplates/NF	10	330	[62]
$FeSe_2$/NF	10	245	[63]
$FePO_4$/NF	10	215	[64]
2D $FePO_4$ sheets/NF	10	218	[65]
FeHP/GC	10	442	[66]
NiFe- Boronized	10	309	[67]
NiFe-LDH	10	184	[68]
$(Ni_2Co_1)_{0.925}Fe_{0.075}$-MOF	10	257	[69]
Co-G	10	270	[70]
Cr-FeNi–P/NCN	10	240	[71]
Ni–Fe LDH@NiCu	10	218	[72]
Fe_2Ni@NC	10	308	[73]
G-$Ni_{0.5}Fe_{0.5}$	10	290	[74]
NiFeNP	10	200	[75]
$NiFeMoO_x$	10	280	[76]
NiFe@NC	10	226	[77]
$LaFe_xNi_{1-x}O_3$	10	302	[78]
FeS	GC	450	[79]
FeB	GC	296	[49]
FeOOH(Se)	IF	287	[80]
Fe_3W_1	Au	410	[81]
FeOOH	NF	280	[82]
$Fe_{2.95}(PO_4)_2(OH)_2$	SS	281	[83]
Iron ore	GC	270	[84]
FeNi@NGE	NF	275	[85]
$Ni_{1-x}Fe_x$ NC	GC	330	[86]
NiOx-Fe	NF-AC	215	[87]
$FeOOH/CeO_2$	NF	250	[88]
Fe–B–O@Fe_2B	Ni foil	273	[89]
Fe–B–O@FeB_2	Ni foil	260	[89]
$LaCo_{0.8}Fe_{0.2}O_{3-\delta}$	GC	293	[90]
SnCoFe	NF	270	[91]
NiFe-LDF-CO_3	GC	300	[92]
CoFe hydroxide	NF	220	[93]
FeCo-Co_4N	N-C	280	[94]
HG-NiFe	GC	310	[95]
Fe-CoO_x	GC	304	[96]
$FeCoWO_x$	Au-foam	191	[97]
Core shell Ni-Fe disulfide@oxyhydroxide	GC	230	[98]
$Ni_{0.7}Fe_{0.3}S_2$ microflowers	NF	198	[99]
NiFe (oxy)sulfide	GC	286	[100]
$Ni_xFe_{1-x}Se_2$	NF	195	[101]
$Ni_{0.75}Fe_{0.25}(OH)_{2+x}$-LDH	NF	210	[102]
$Ni_{0.75}Fe_{0.25}(OH)_{2+x}$-LDH	GC	270	[102]

Characterization of FeAs and films deposited on FTO

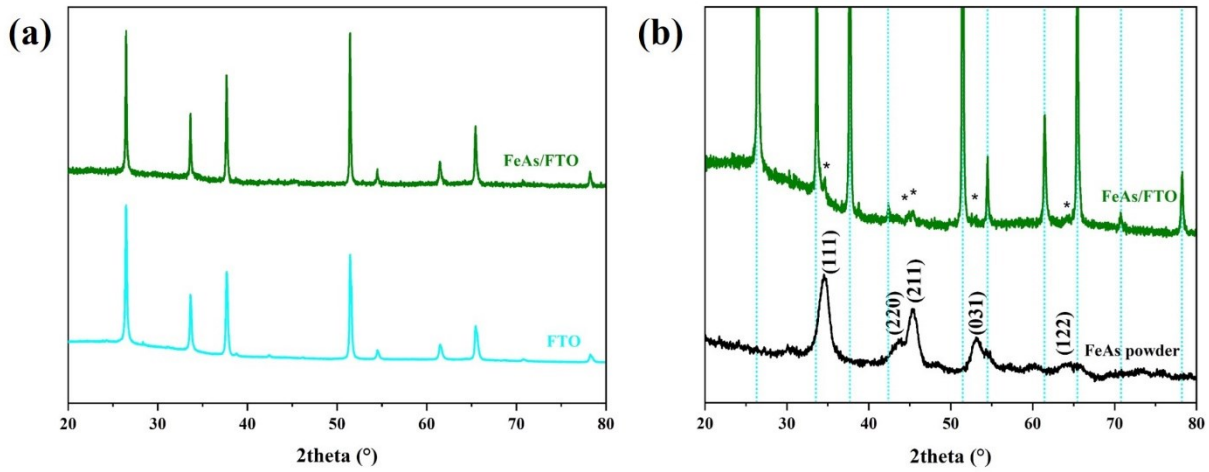

Figure S25. (a) XRD patterns of FeAs/FTO compared to bare FTO, (b) zoom-in of the XRD spectra of FeAs/FTO comparted to powder FeAs, showing the signals emerging on the diffraction pattern after deposition. The light blue lines represent the diffractions peaks associated with FTO (cassiterite, SnO_2, JCPDS 41-1445). The new peaks marked with an asterisk (*) are related to FeAs (JCPDS 76-458).

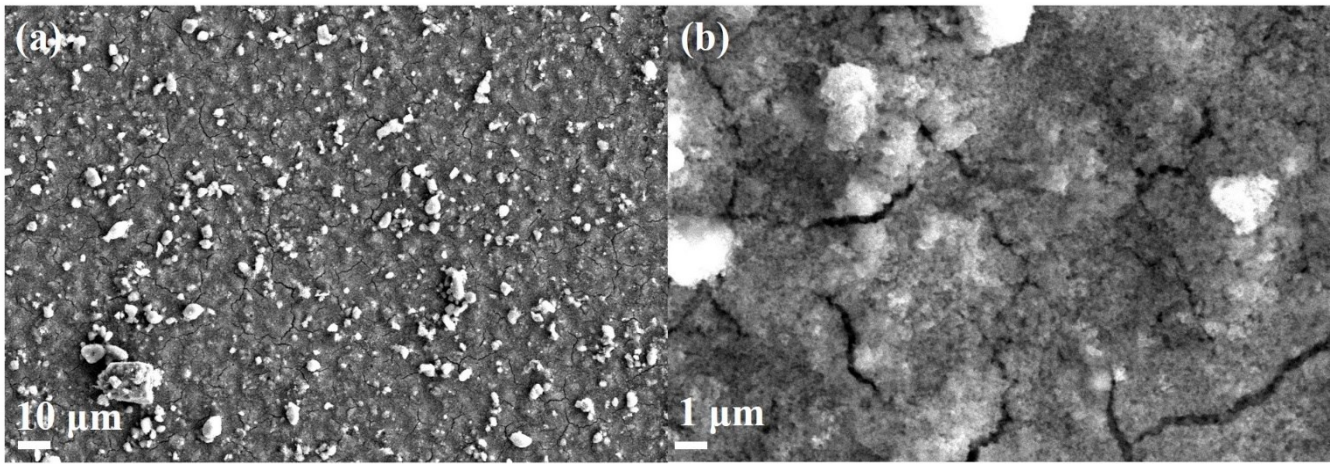

Figure S26. SEM of the FeAs films deposited on FTO at (a) 500x and (b) 5000x. Agglomerated FeAs particles can be observed on the low magnification figure. The high magnification figure proves that the morphology of the material is maintained after the deposition (compare to as prepared FeAs SEM in Figure S6).

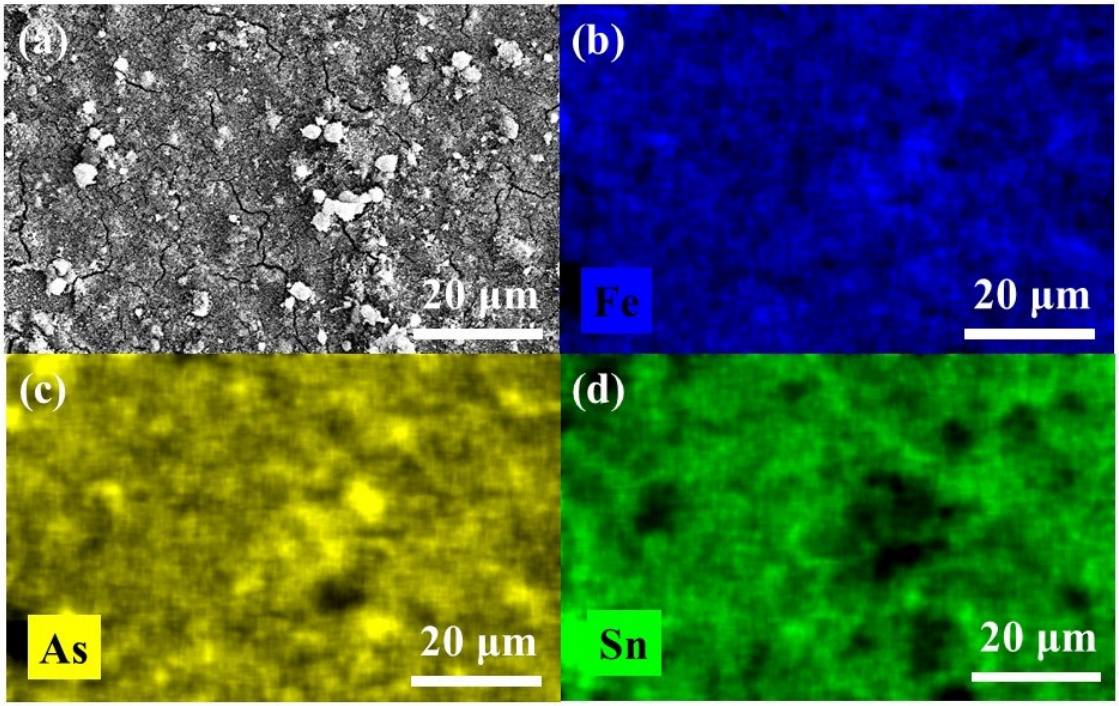

Figure S27. (a) SEM of FeAs/FTO and elemental mapping of (b) Fe (blue), (c) As (yellow) and (d) Sn (green). Sn arises from the FTO glass substrate. Homogenous distribution of Fe and As was observed in the particles deposited on FTO.

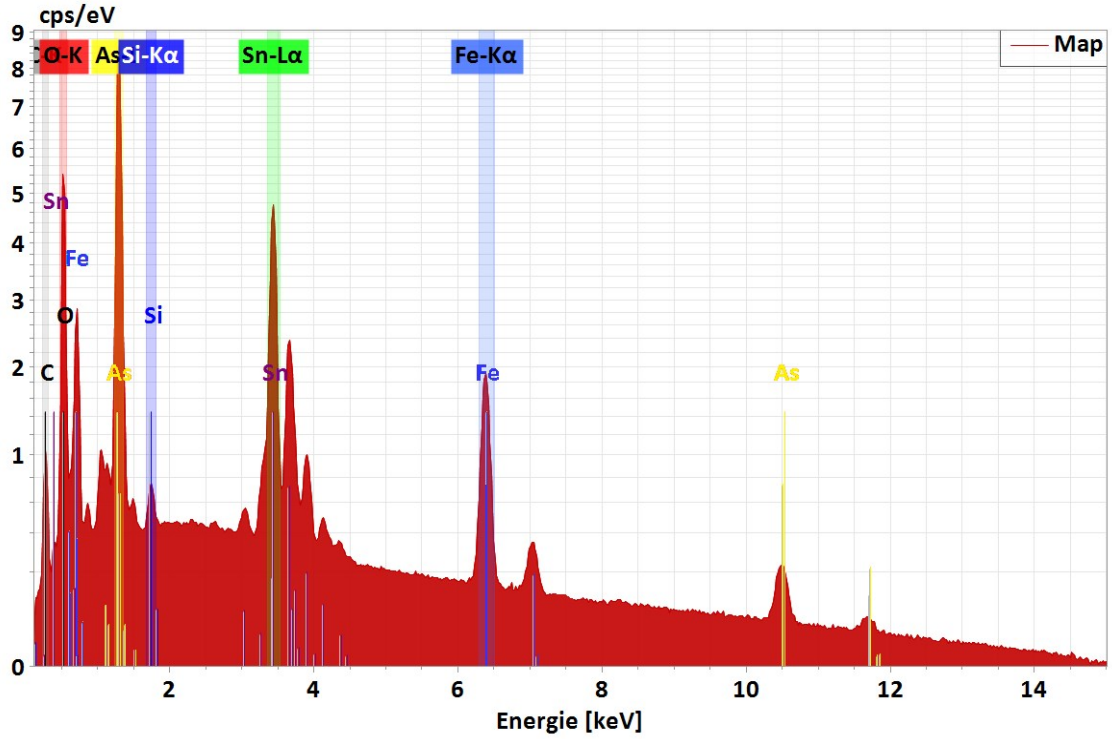

Figure S28. SEM-EDX of the FeAs film deposited on FTO, which confirmed the presence of Fe and As. The presence of Si emission peaks arises from the Si wafer used in the measurement. Sn signals arise from the FTO substrate. Fe:As ratio on the film is 1:1.24 ± 0.11 as determined by SEM-EDX.

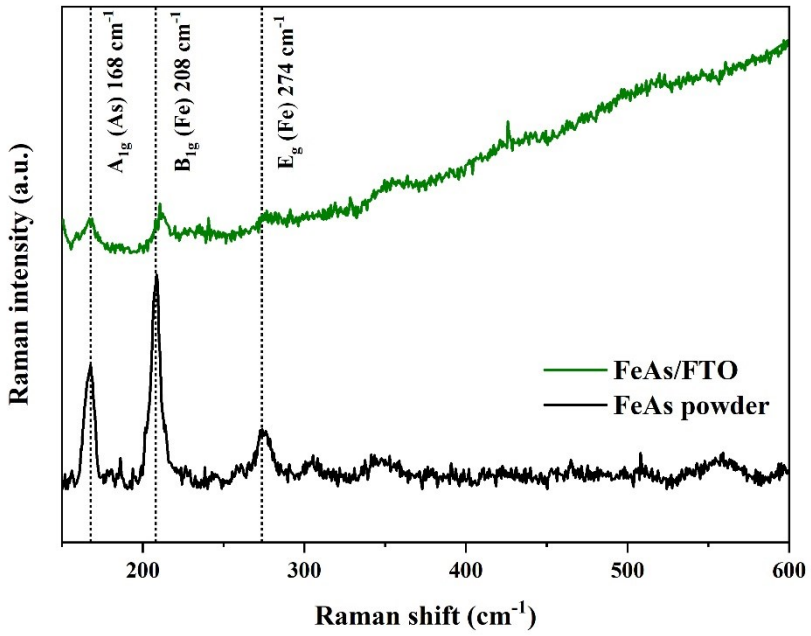

Figure S29. (Resonance) Raman spectra of FeAs/FTO compared to FeAs powder. The major bands of the FeAs powder are also present in the corresponding spectrum of the FeAs/FTO. A detailed band assignment is given in Figure S9.

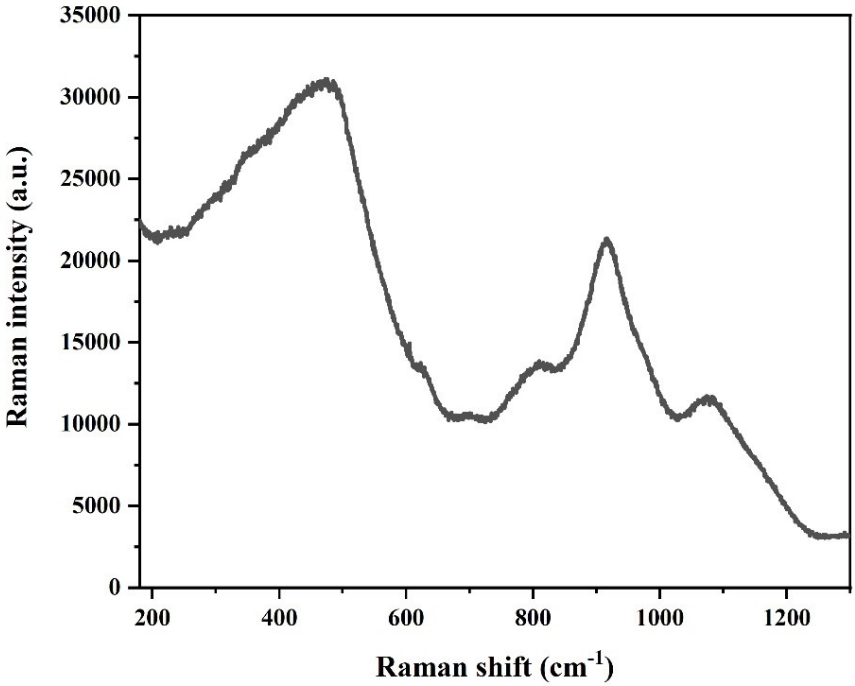

Figure S30. (Resonance) Raman spectrum of bare FTO. This spectrum was used as a reference in order to assign band frequencies referring only to FeAs.

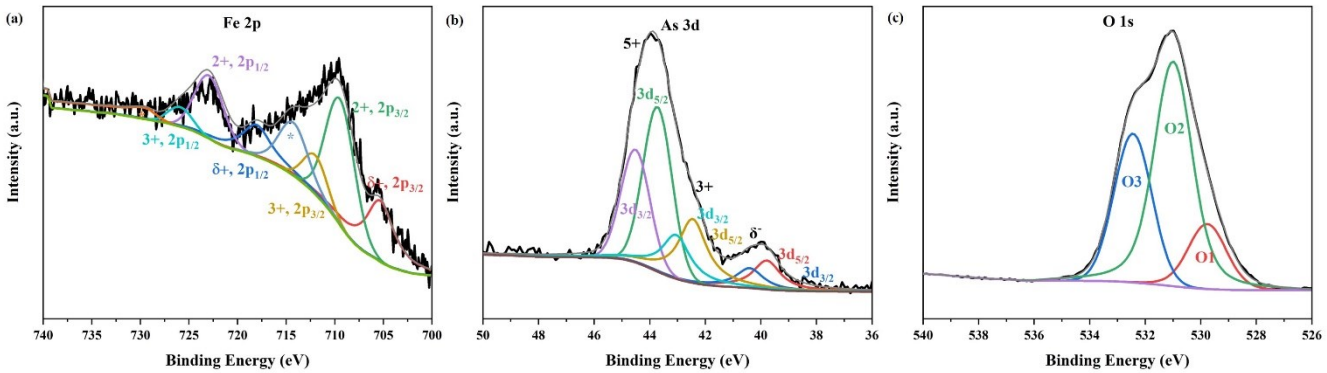

Figure S31. The deconvoluted XPS spectra of FeAs/FTO are shown on (a) Fe 2p, (b) As 3d and (c) O 1s. The Fe 2p deconvoluted spectrum shows the two peaks for $Fe^{\delta+}$ at $2p_{3/2}$ 705.5 eV and $2p_{1/2}$ 718.2 eV,[29] and peaks associated to Fe^{2+} ($2p_{3/2}$ 709.7 eV and $2p_{1/2}$ 723.1 eV) and Fe^{3+} ($2p_{3/2}$ 712.4 eV and $2p_{1/2}$ 726.1 eV), and one pair of satellite peaks from Fe^{2+} ($2p_{3/2}$ 714.5 eV and $2p_{1/2}$ 729.6 eV). The presence of peaks related to associated with oxidized Fe species originate from the contact of the material with air. The As 3d deconvoluted spectrum shows two peaks related to remaining $As^{\delta-}$ present in FeAs (40.0 eV), deconvoluted into 39.8 eV ($3d_{5/2}$) and 40.4 eV ($3d_{3/2}$), and oxidized As^{3+} (43.2 eV) and As^{5+} (43.9 eV) due to air exposure, deconvoluted into 42.5 eV ($3d_{5/2}$) and 43.1 eV ($3d_{3/2}$); and 43.8 eV ($3d_{5/2}$) and 44.5 eV ($3d_{3/2}$), respectively.[30] Finally, the O 1s spectrum shows one peak (531.1 eV) which is deconvoluted into three peaks derived from air exposure: Fe-O (O1, 529.8)[32] and As-O (O2, 531.0 eV).[30,31] The peak at higher binding energy (O3, 532.5 eV) is associated to adsorbed water on the surface.[32]

Electrochemical experiments on FTO

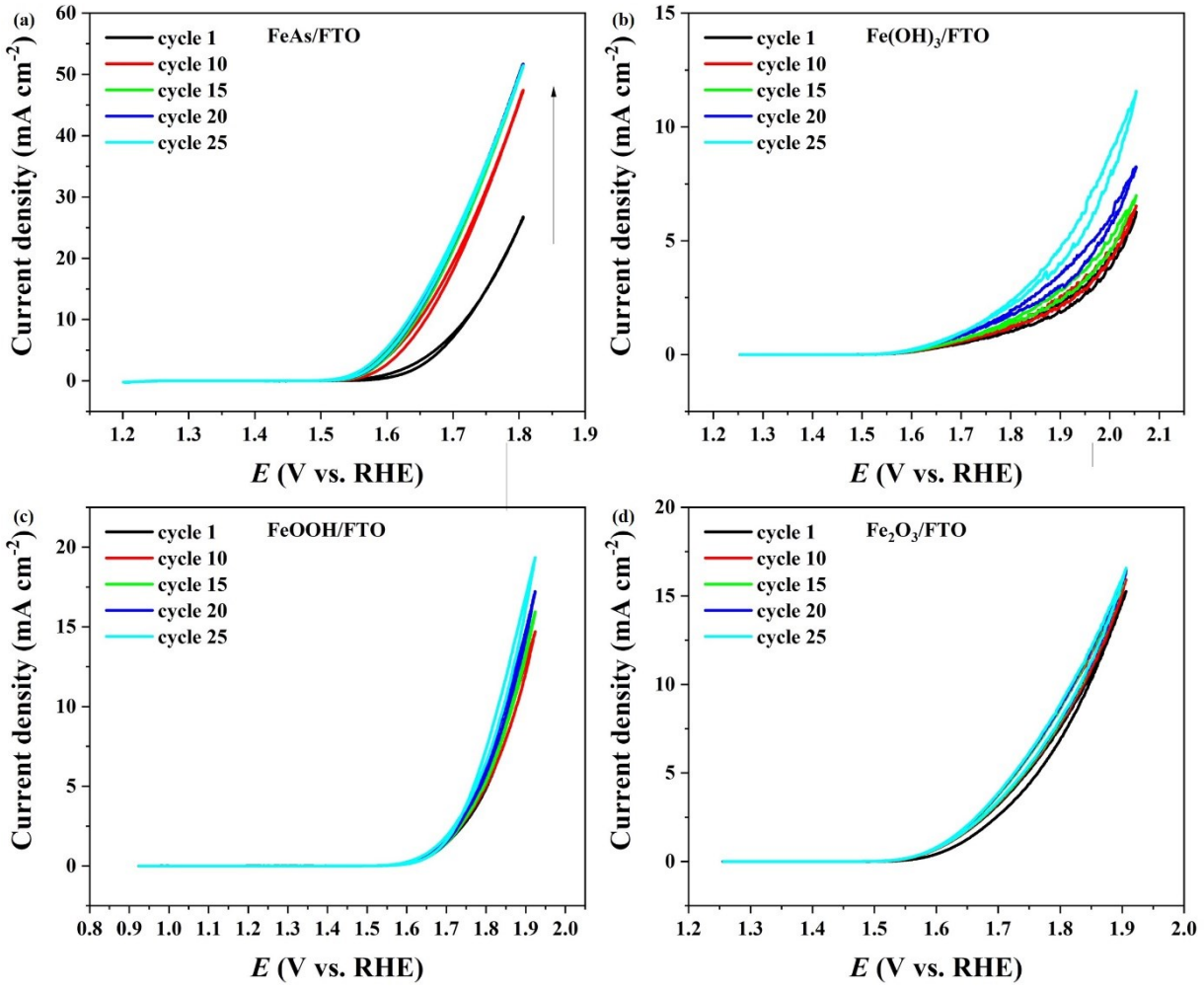

Figure S32. Activation of the (a) FeAs/FTO, (b) $Fe(OH)_3$/FTO, (c) FeOOH/FTO, and (d) Fe_2O_3/FTO by CV in 1 M KOH, 5 mV s^{-1}.

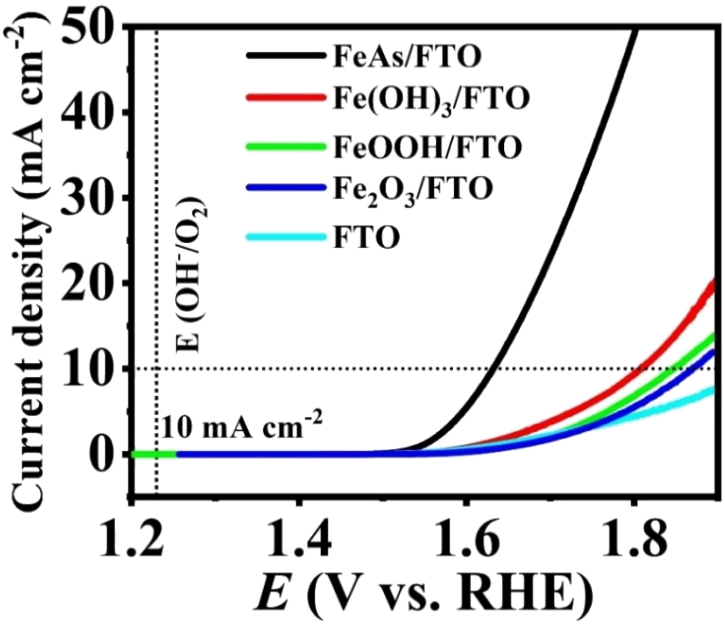

Figure S33. LSV (5 mV s^{-1}) of FeAs and Fe reference materials loaded on FTO (0.5 mg cm^{-2}). The order found for the overpotentials was the same as in the case of NF. For FeAs/FTO, η = 395 ± 6 mV (10 mA cm^{-2}) was obtained, which substantially lower than other $Fe(OH)_3$/FTO (577 ± 3 mV), FeOOH/FTO (609 ± 5 mV) and Fe_2O_3/FTO (639 ± 5 mV).

Table S10. Deposition time, mass loading, and overpotential (10 mA cm^{-2}) of FeAs films over FTO.

Deposition time (s)	Weight (mg)	Overpotential (mV @10 mA cm^{-2})	Current density at η = 500 mV
4	0.0062*	633 ±4	4.43
7.5	0.0125*	604 ±3	4.60
15	0.025*	533 ±5	7.88
30	0.05*	530 ±3	7.93
60	0.1 ±0.1	448 ±2	14.23
120	0.2 ±0.1	442 ±5	16.68
240	0.4 ±0.1	392 ±4	34.35
480	0.6 ±0.1	402 ±4	31.39

*weight determined by extrapolation of higher time deposition weights. The weight difference was not possible to measure precisely due to limitations in the used scale.

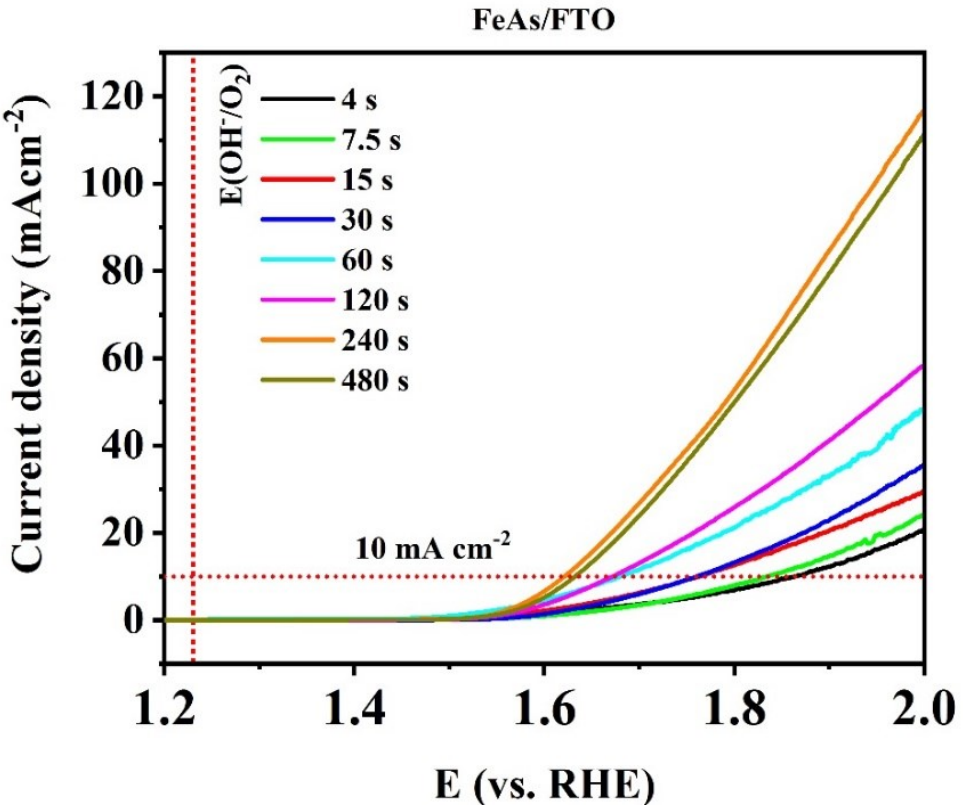

Figure S34. Polarization curves recorded for films prepared with different mass loadings of FeAs on 1 cm^2 FTO surface in 1 M KOH solution with a sweep rate of 20 mV s^{-1} (4 s to 480 s).

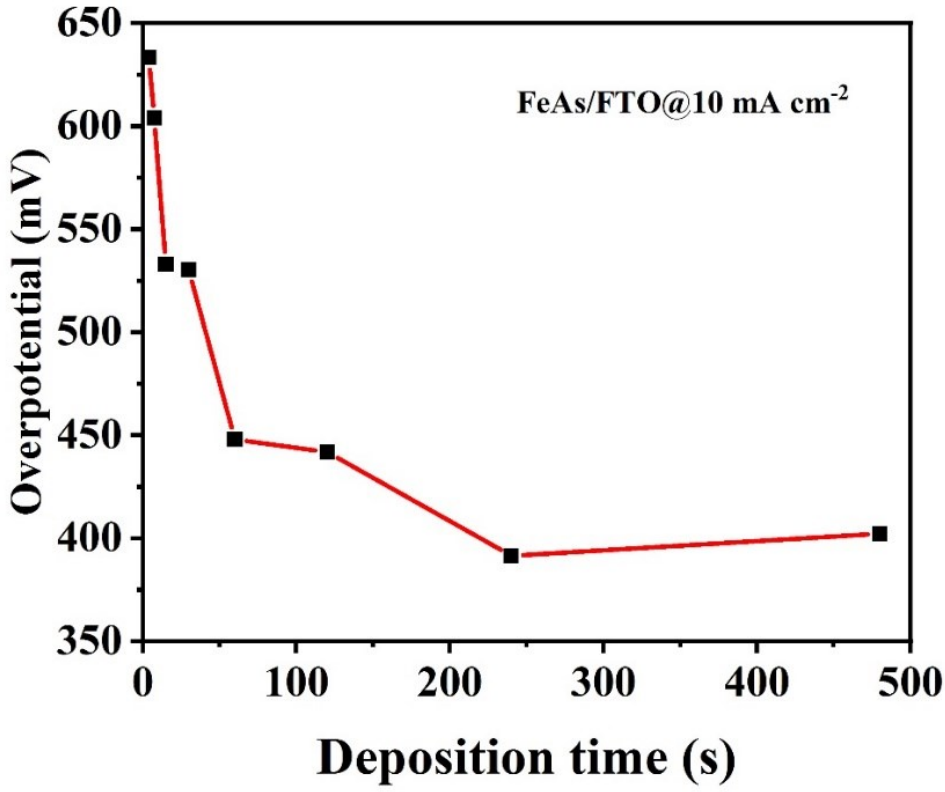

Figure S35. The overpotentials of FeAs on 1 cm^2 FTO surface with respect to deposition time of 4 s to 480 s (varying mass loadings; see Table S10).

Table S11. Deposition time, mass loading, and overpotential (10 mA cm^{-2}) of $Fe(OH)_3$ films over FTO.

Deposition time (s)	Weight (mg)	Overpotential (mV @10 mA cm^{-2})	Current density at η = 600 mV
4	0.05*	**	0.20
7.5	0.1 ±0.1	**	0.39
15	0.2 ±0.1	836 ±5	2.16
30	0.5 ±0.1	763 ±6	3.48
60	1.0 ±0.1	723 ±3	4.40
120	1.6 ±0.1	648 ±4	6.93
240	2.4 ±0.1	583 ±5	11.31
480	3.0 ±0.1	598 ±5	10.11

*weight determined by extrapolation of higher time deposition weights. The weight difference was not possible to measure precisely due to limitations in the used scale.

**the overpotential was not determined because the current densities were below 10 mA cm^{-2} (Figure S37).

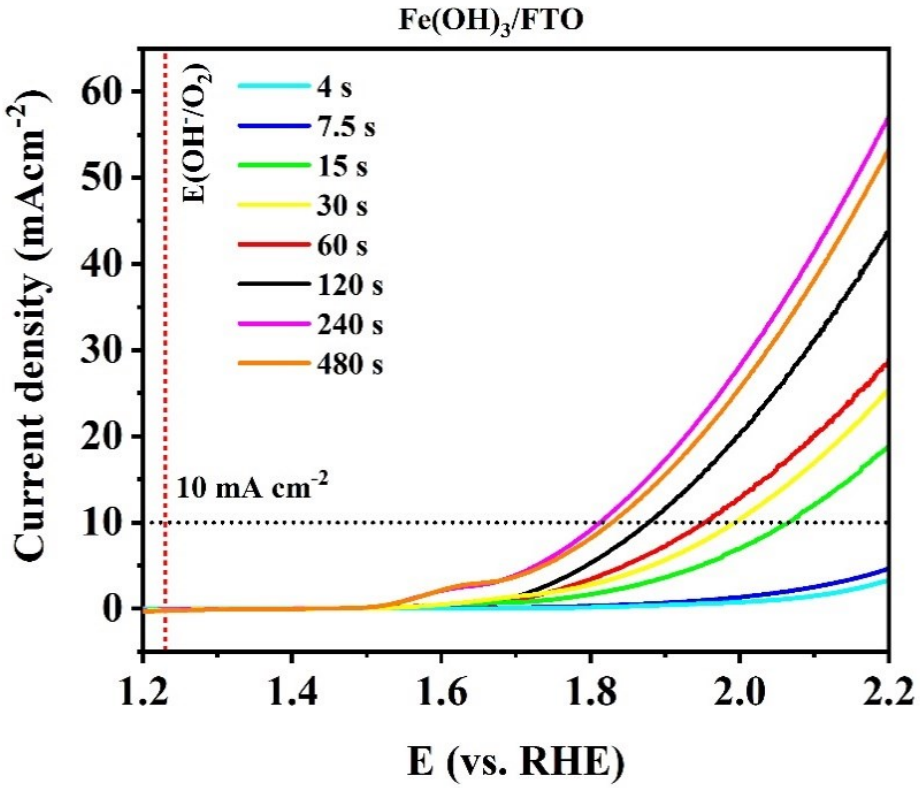

Figure S36. Polarization curves recorded for films prepared with different mass loadings of $Fe(OH)_3$ on 1 cm^2 FTO surface in 1 M KOH solution with a sweep rate of 20 mV s^{-1} (4 s to 480 s).

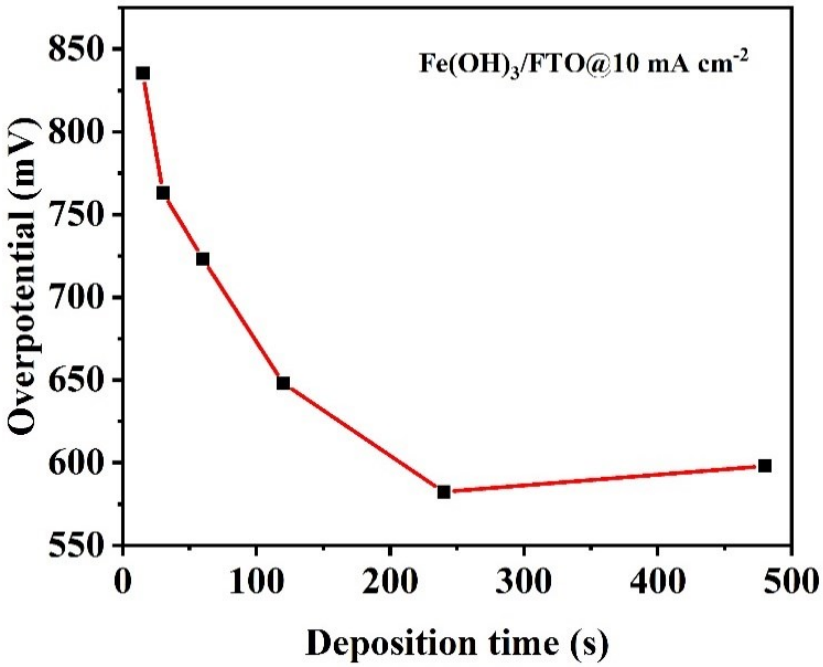

Figure S37. The overpotentials of $Fe(OH)_3$ on 1 cm^2 FTO surface with respect to deposition time of 4 s to 480 s (varying mass loadings; see **Table S11**).

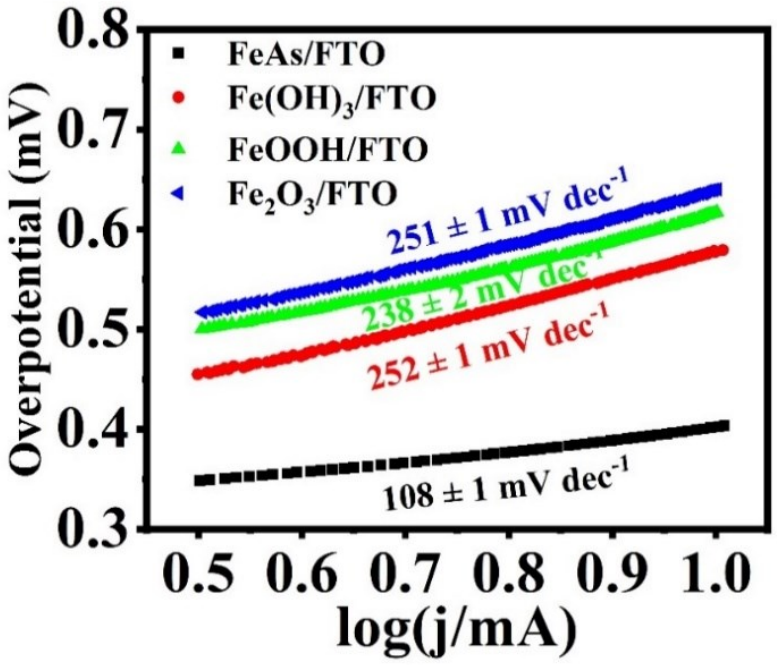

Figure S38. Tafel slopes obtained from LSVs (1 mV s^{-1}) of FeAs/FTO and Fe reference materials loaded on FTO (0.5 mg cm^{-2}). The FeAs/FTO has the lowest Tafel slope, indicating faster reaction kinetics.[103] The Tafel slope increased in the order FeAs/FTO < $Fe(OH)_3$/FTO < FeOOH/FTO < Fe_2O_3/FTO and follows the same order as obtained for the samples deposited on NF.

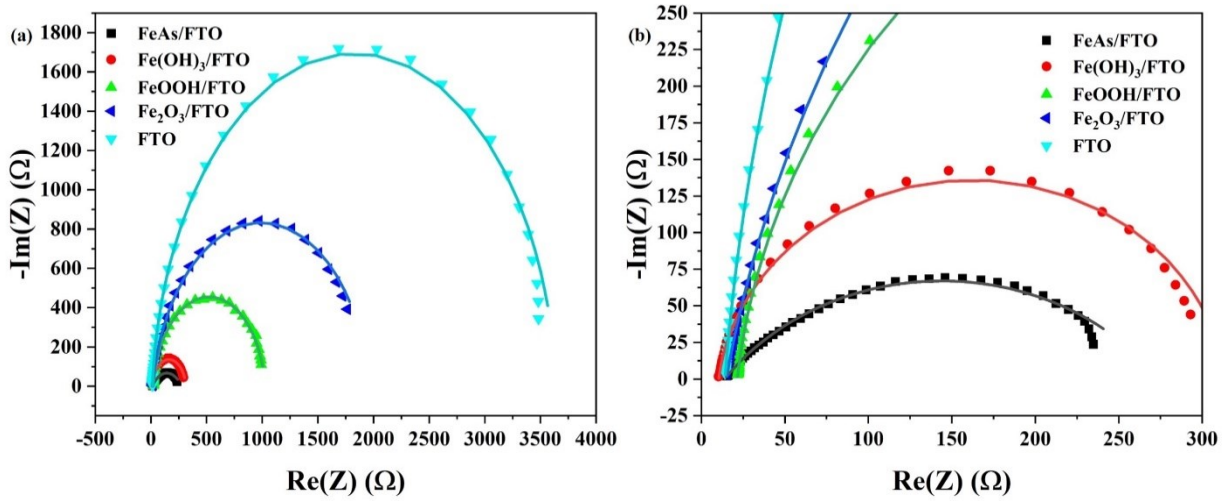

Figure S39. (a) Nyquist plot constructed from the EIS experiment of materials deposited on FTO. The spectra were collected with an anodic polarization potential of 1.58 V vs RHE. (b) Zoom of the Nyquist plot. The continuous lines show the fitting to the circuit which contains two resistors R_1 and R_2 and Q a constant phase element (CPE) (Figure 3c). Please refer to Figure S19 to discussion on the fitting of the parameters.

Table S12. R_2 (Ω) (R_{ct}), R_1 (Ω) (R_s), Q ($F \times s^{(a_2 - 1)}$) and a_2 of FeAs, $Fe(OH)_3$, FeOOH and Fe_2O_3 deposited on FTO, compared to the bare FTO.

Material	R_{ct} **(Ω)**	R_s **(Ω)**	Q ($F \times s^{(a_2 - 1)}$)	a_2
FTO	3626.0 ± 0.6	14.3 ± 0.2	$9.0 \times 10^{-6} \pm 1.3 \times 10^{-8}$	$9.6 \times 10^{-1} \pm 1.0 \times 10^{-2}$
FeAs/FTO	260.3 ± 0.3	13.9 ± 0.3	$5.1 \times 10^{-4} \pm 9.7 \times 10^{-6}$	$6.1 \times 10^{-1} \pm 1.1 \times 10^{-2}$
$Fe(OH)_3$/FTO	303.3 ± 0.9	10.4 ± 0.3	$1.7 \times 10^{-5} \pm 4.8 \times 10^{-7}$	$9.3 \times 10^{-1} \pm 1.2 \times 10^{-2}$
FeOOH/FTO	1000.2 ± 0.4	21.5 ± 0.3	$1.4 \times 10^{-5} \pm 9.9 \times 10^{-8}$	$9.4 \times 10^{-1} \pm 1.1 \times 10^{-2}$
Fe_2O_3/FTO	1949.0 ± 1.8	14.8 ± 0.3	$2.8 \times 10^{-5} \pm 3.8 \times 10^{-8}$	$9.0 \times 10^{-1} \pm 1.0 \times 10^{-2}$

Table S13. Specific resistivity ρ (Ω cm) of FeAs, $Fe(OH)_3$, FeOOH, Fe_2O_3, and FeAs after CP OER deposited on FTO, compared to the bare FTO recorded by a four-point probe resistivity measurement.

Material	**ρ (Ω cm)**
FeAs/FTO	1.86×10^2
FeAs/FTO after OER	3.09×10^3
$Fe(OH)_3$/FTO	5.60×10^4
FeOOH/FTO	2.30×10^5
Fe_2O_3/FTO	2.45×10^5

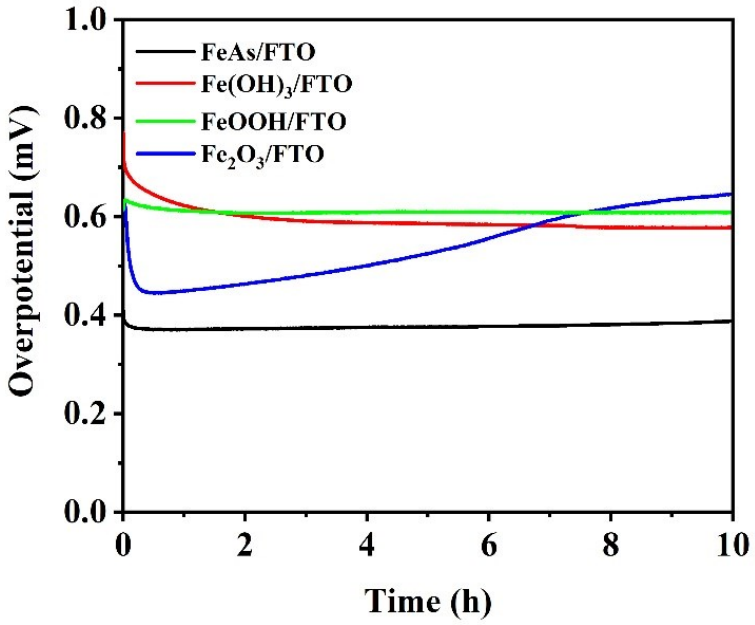

Figure S40. Chronopotentiometry experiment (CP) at 10 mA cm^{-2} for 10 h on FTO. A slight increase of the overpotential was observed during the experiment for the FeAs/FTO ($\eta = 380 \pm 6$ mV). The Fe-based reference materials show all deactivation after 10 h of continuous electrolysis: $Fe(OH)_3$ ($\eta = 580 \pm 80$ mV), FeOOH ($\eta = 610$ mV), Fe_2O_3 ($\eta = 650$ mV).

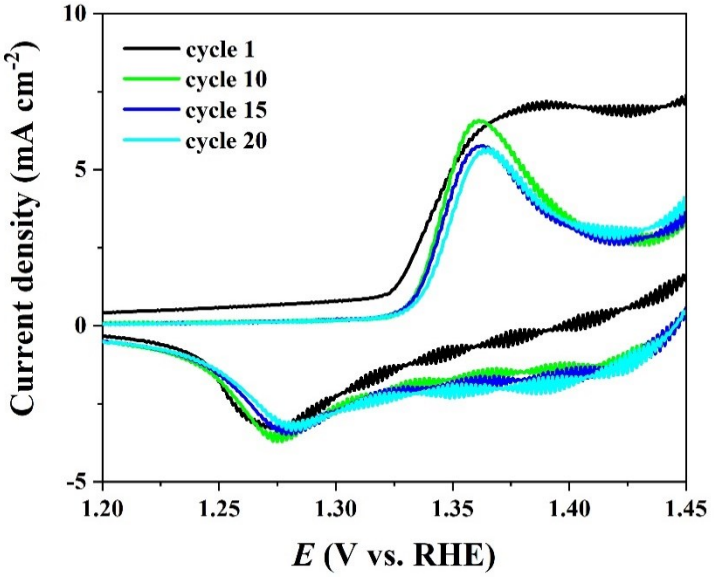

Figure S41. Evolution of redox peak observed for FeAs/NF. The anodic and cathodic peaks appear at 1.36 V and 1.28 V, respectively (vs. RHE). Scan rate: 5 mV s^{-1}.

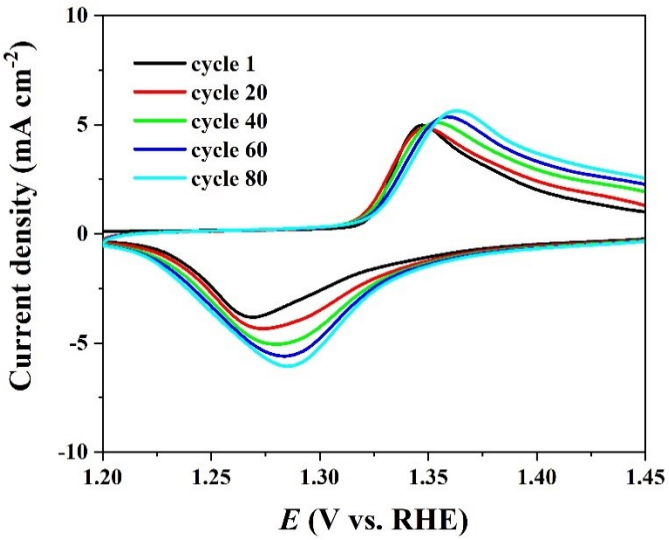

Figure S42. Evolution of redox peaks observed for bare NF. The anodic and cathodic peaks appear at 1.36 V and 1.28 V, respectively (vs. RHE). Scan rate: 5 mV s^{-1}.

Post-catalytic characterization

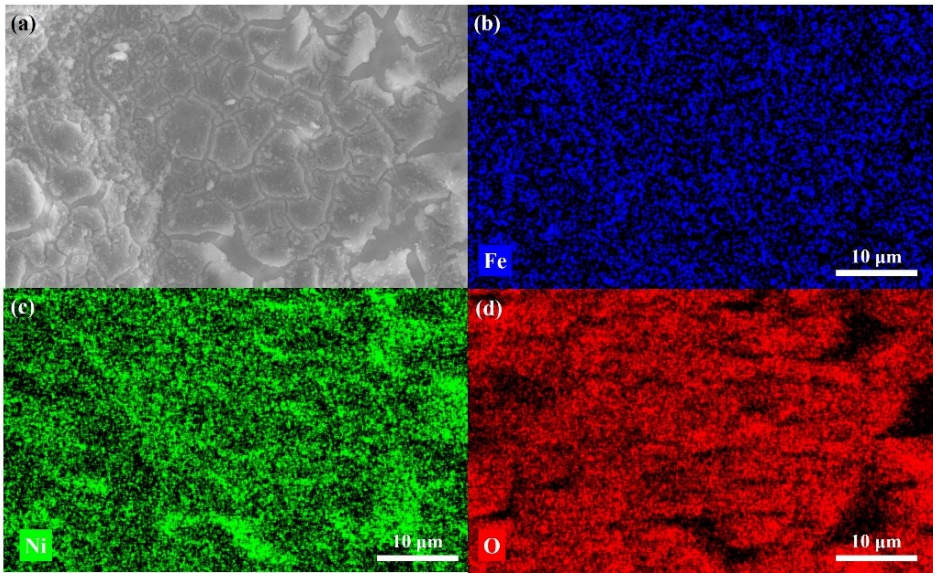

Figure S43. (a) SEM and the elemental mapping (b-d) of FeAs/NF after continuous CP OER for 2 h. The homogenous distribution of Fe (blue) and O (red) is observed on the surface of the film. Ni (green) arises from the NF and the mapping of As is omitted due to its complete loss (see EDX below).

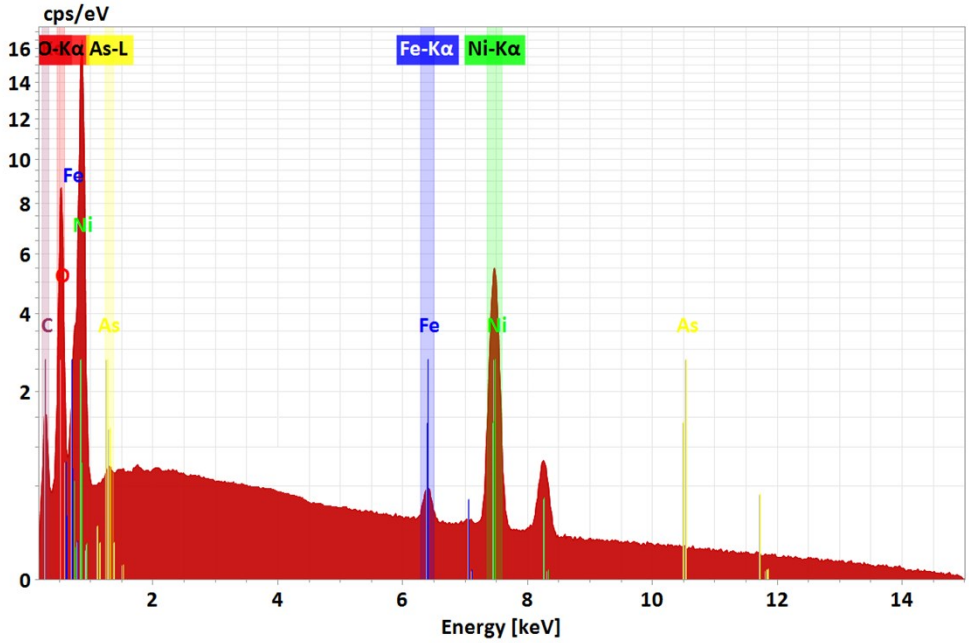

Figure S44. SEM-EDX of the FeAs/NF film after CP OER for 2 h. Fe is present after OER. The peaks corresponding to the high-energy emission of As ($K\alpha_1$, $K\alpha_2$ at 10.54 keV, 10.51 keV, and K β_1 at 11.73 keV) do not appear. The attained SEM-EDX of Fe:As ratio was 1:0.02 ± 0.01.

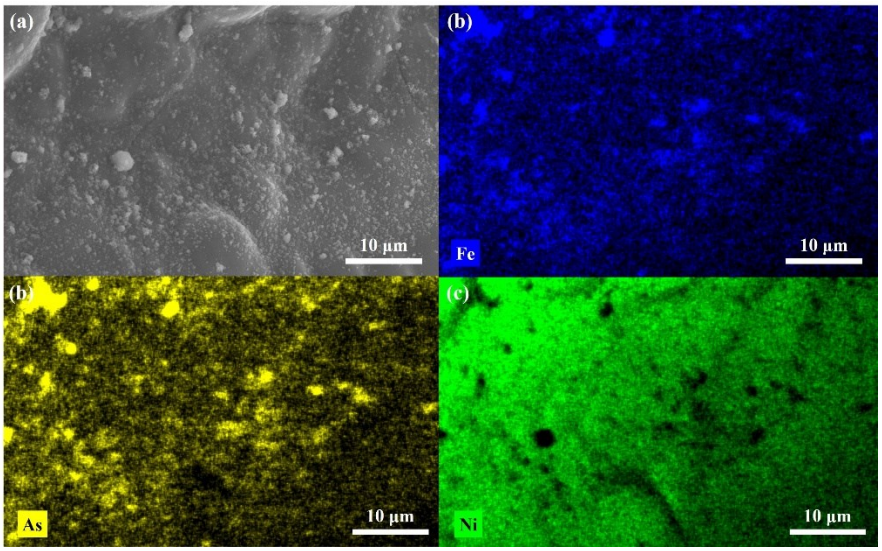

Figure S45. (a) SEM of FeAs/NF after the first CV and elemental mapping of (b) Fe (blue), (c) As (yellow), and (d) Ni (green). Ni arises from the NF.

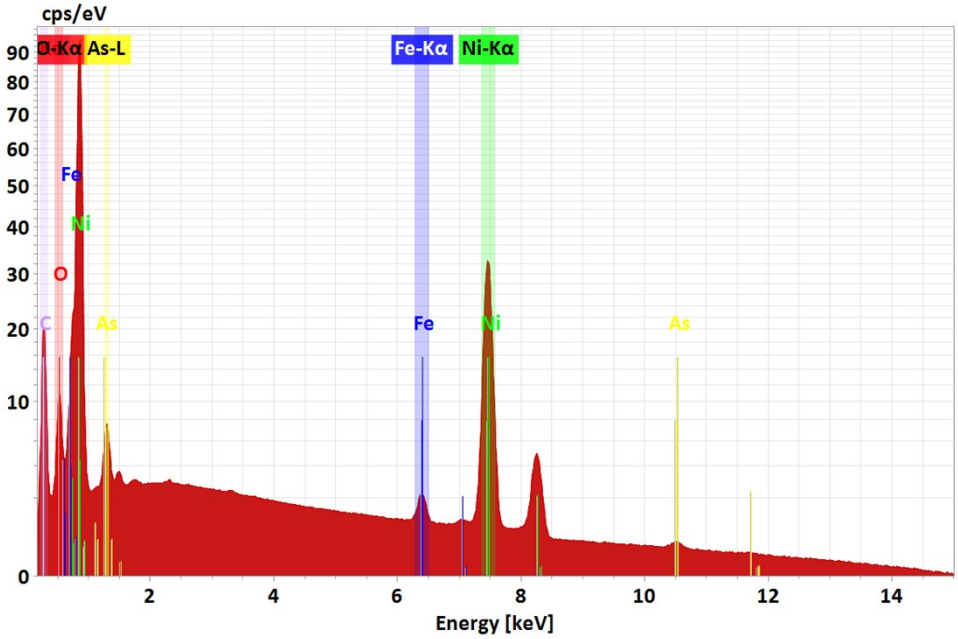

Figure S46. SEM-EDX of the film of FeAs/NF after the first CV. Fe is present after OER. The attained SEM-EDX of Fe:As ratio was 1:0.91 ± 0.02.

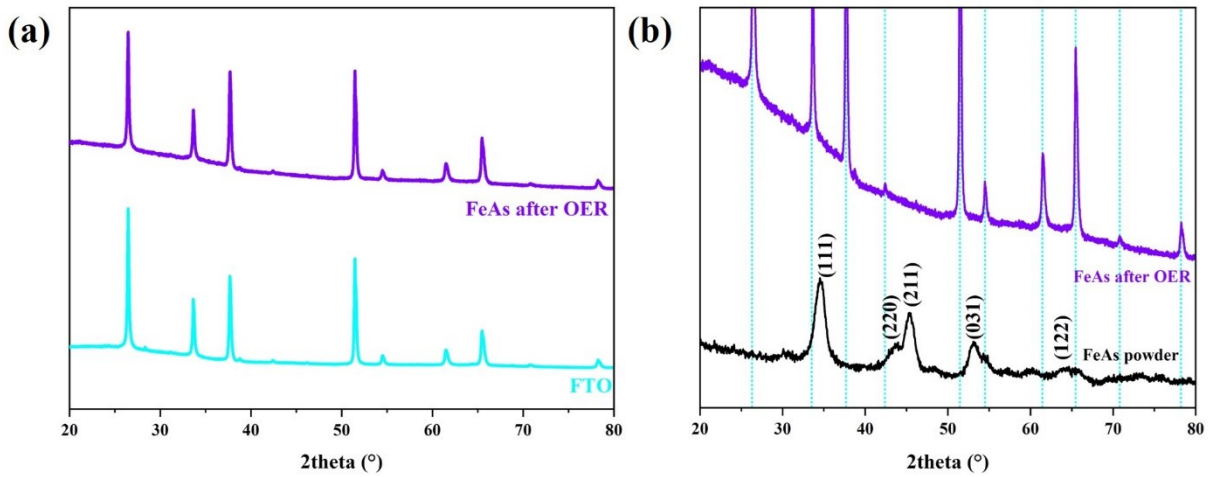

Figure S47. (a) XRD patterns of FeAs/FTO after OER (CP OER 24h) compared to bare FTO, (b) zoom-in of the XRD spectra of FeAs/FTO after OER (CP OER 24h) comparted to powder FeAs, showing no signals of FeAs are left after OER (CP OER 24h) which indicates the transformation of the material (compare to as prepared FeAs/FTO XRD pattern on Figure S25b). The light blue lines represent the diffractions peaks associated with FTO (cassiterite, SnO_2, JCPDS 41-1445).

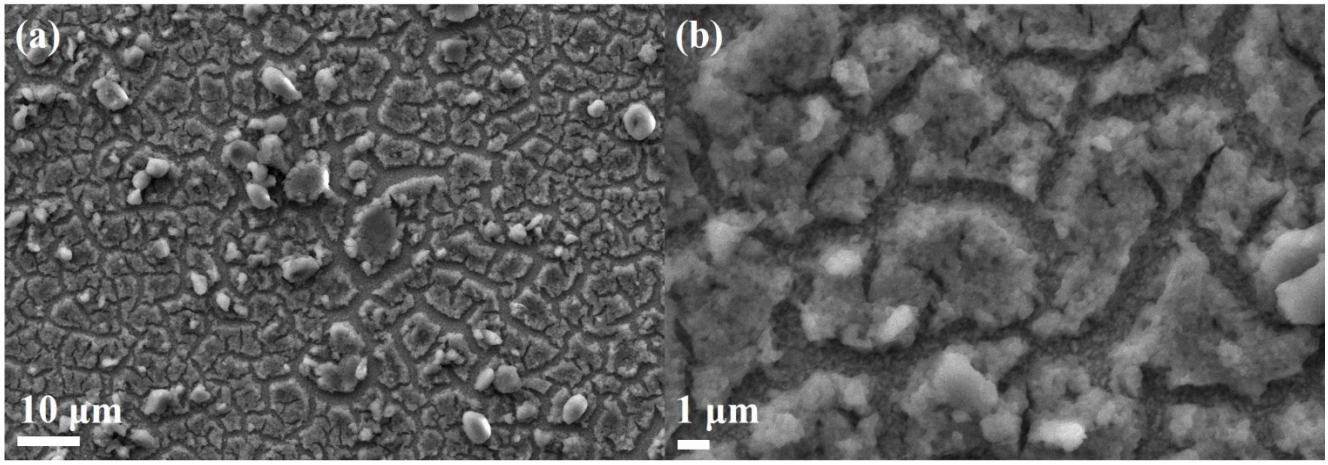

Figure S48. SEM of the FeAs/FTO after OER (CP OER 24h) at (a) 1000x and (b) 5000x. The image shows the cracking of the film, exposing FTO. The cracking appears during the drying process as reported before in the literature.[104]

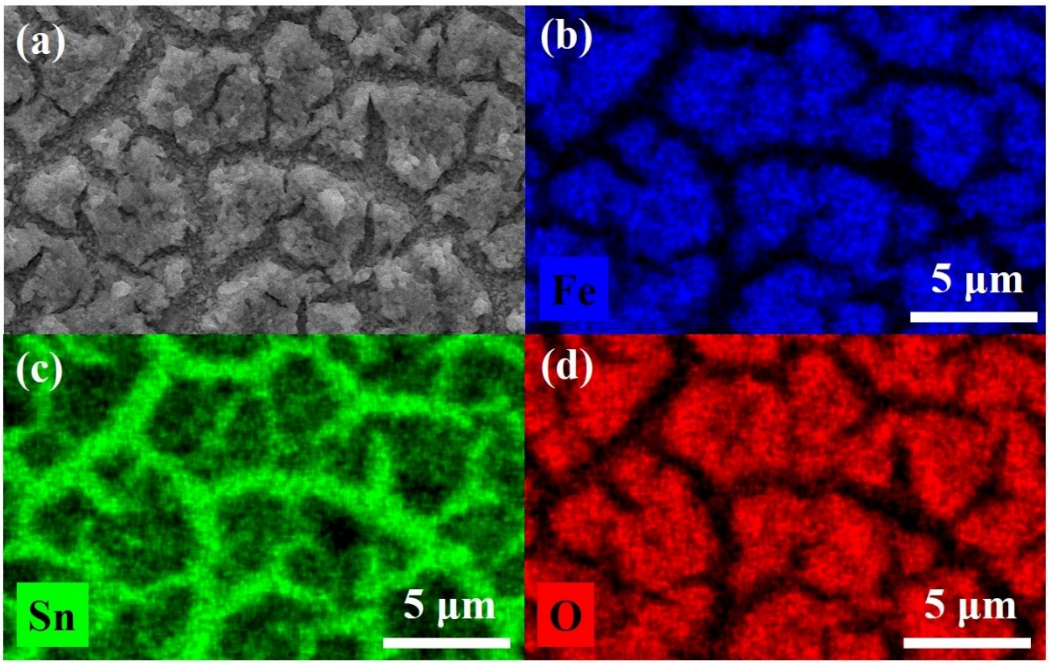

Figure S49. (a) SEM of FeAs/FTO after OER (CP OER 24h) and elemental mapping of (b) Fe (blue), (c) Sn (green) and (d) O (red). Homogenous distribution of Fe and O can be observed in the areas where the film is remaining. As mapping is not included since 96 ± 1% of As leaches into the solution (see Figure S50). Sn arises from the FTO glass substrate.

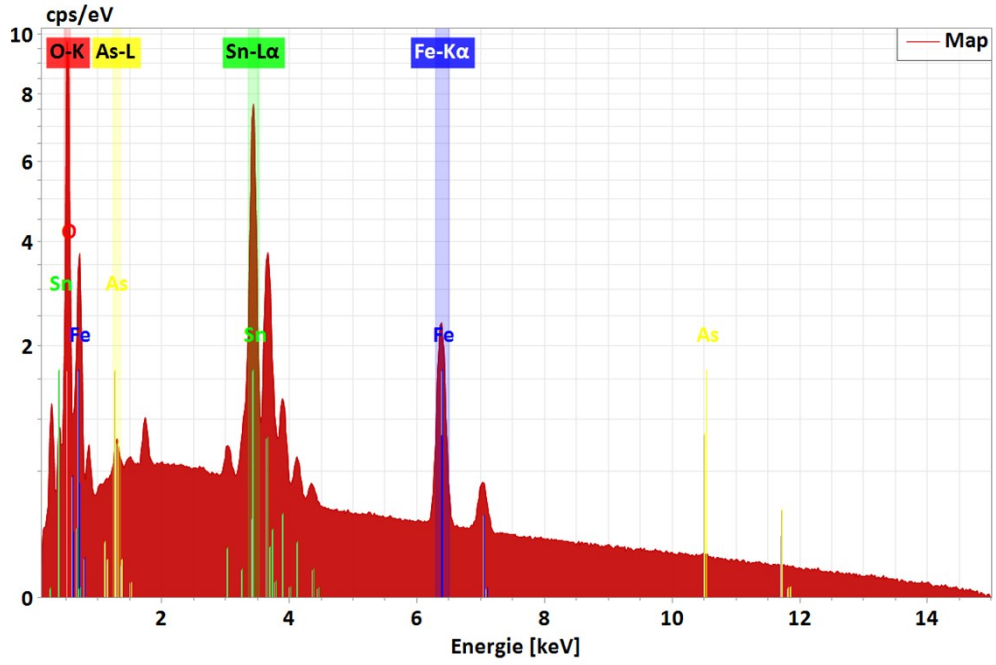

Figure S50. SEM-EDX of the film of FeAs/FTO after OER (CP OER 24h). Fe is present after OER (CP OER 24h), however, the peaks corresponding to the high-energy emission of As ($K\alpha_1$, $K\alpha_2$ at 10.54 keV, 10.51 keV and K β_1 at 11.73 keV) do not appear, indicating a loss of As into the solution. The attained SEM-EDX Fe:As ratio was 1:0.04 ± 0.01. The emission peaks in the 1.5-2 keV region correspond to Al ($K\alpha_1$, $K\alpha_2$ at 1.487 keV, 1.486 keV and K β_1 at 1.557 keV) and Si ($K\alpha_1$, $K\alpha_2$ at 1.740 keV, 1.739 keV and K β_1 at 1.836 keV) arise from the Al sample holder and the Si wafer used during the measurement, respectively.

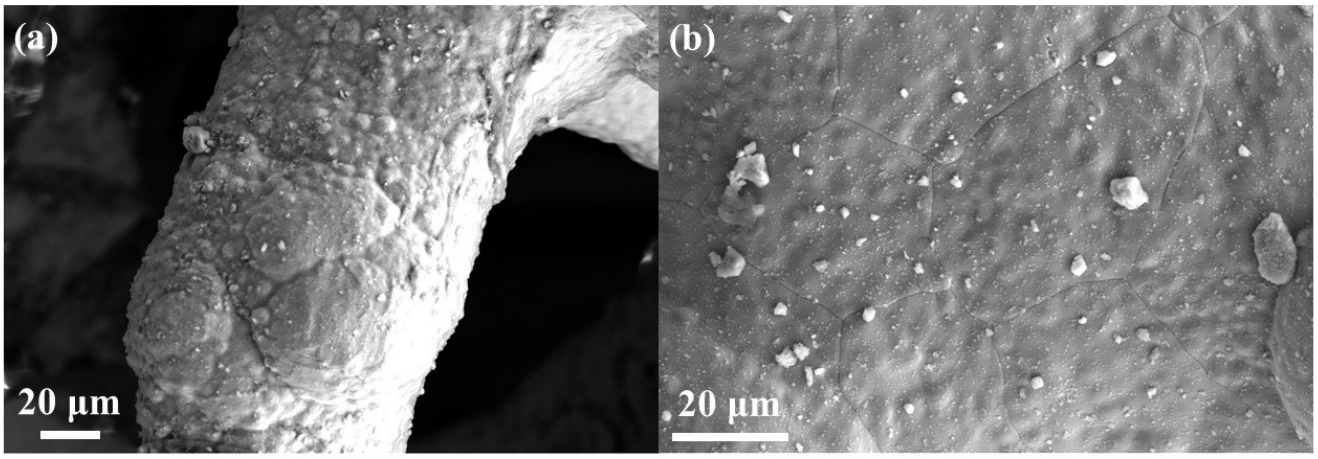

Figure S51. SEM of the FeAs/NF after OER (CP OER 24h).

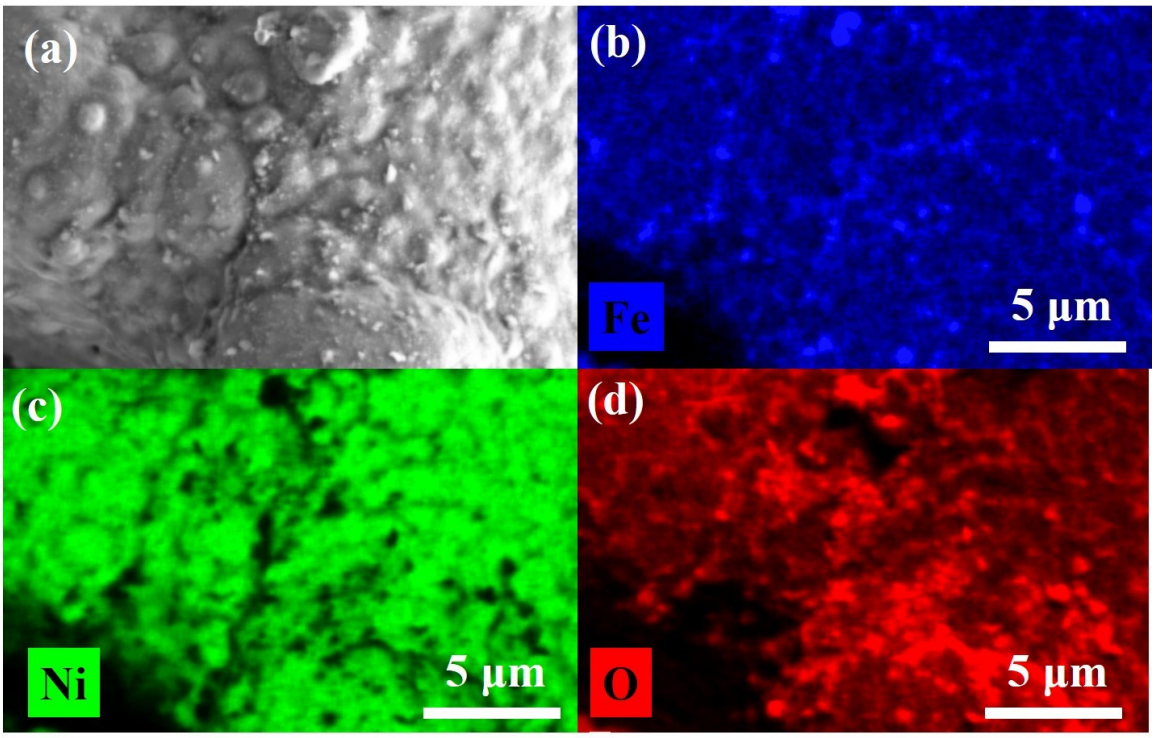

Figure S52. (a) SEM of FeAs/NF after OER (CP OER 24h) and elemental mapping of (b) Fe (blue), (c) As (yellow), (d) Sn (green) and (e) O (red). Homogenous distribution of Fe and O can be observed in the areas where the film is remaining. As mapping is not included since 95 ± 1% of As leaches into the solution (see Figure S53). Ni arises from the NF.

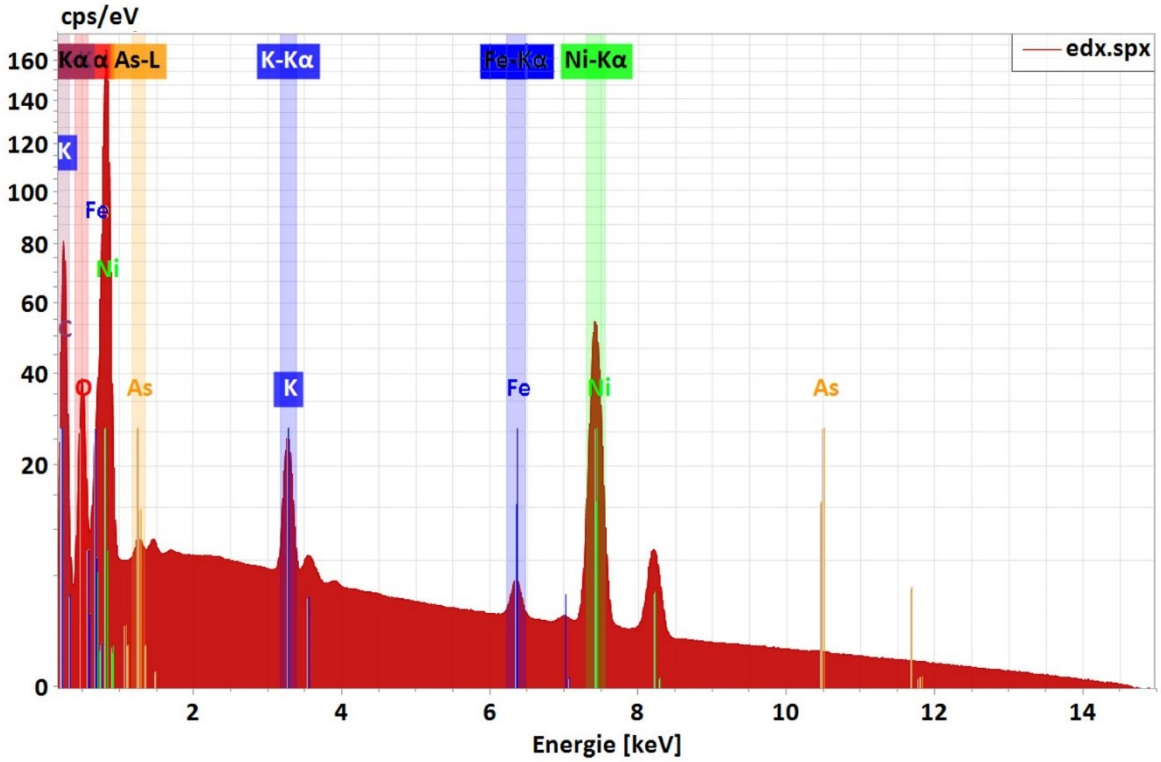

Figure S53. SEM-EDX of the film of FeAs/NF after OER (CP OER 24h). Fe is present after OER (CP OER 24h), in a similar way as in the experiment on FTO (Figure S50) the peaks corresponding to the high-energy emission of As ($K\alpha_1$, $K\alpha_2$ at 10.54 keV, 10.51 keV and K β_1 at 11.73 keV) do not appear. The attained SEM-EDX of Fe:As ratio was 1:0.05 ± 0.01. The emission peaks in the 1.5-2 keV region correspond to Al ($K\alpha_1$, $K\alpha_2$ at 1.487 keV, 1.486 keV and K β_1 at 1.557 keV) and Si ($K\alpha_1$, $K\alpha_2$ at 1.740 keV, 1.739 keV and K β_1 at 1.836 keV) arise from the Al sample holder and the Si wafer used during the measurement, respectively. The presence of K is due to the KOH 1M electrolyte used for the experiment.

Table S14. The concentration of Fe and As in the electrolyte solution after CP OER on FTO and NF. The concentration was determined by ICP-AES of the solution. For each long term experiment, 45 mL of KOH 1 M were used. The electrolyte solution was divided into three parts (15 mL each) and each one measured by ICP-AES. The average value of three independent measurements is shown on the table. The percentage of element loss in solution was calculated from the concentration in solution, the initial Fe:As ratio and the weight of the films.

Sample	Fe (mg/L)	As (mg/L)	Fe:As ratio	% of element loss in solution	
				%Fe	%As
1 M KOH	0.00	0.00	-	-	-
FeAs/FTO OER CP 24 h	0.13±0.03	0.33±0.02	2.00±0.27	3.4±0.8%	6.3±0.4%
FeAs/NF OER CP 24 h	0.29±0.01	2.33±0.12	6.02±0.25	3.1±0.1%	18.0±1.1%

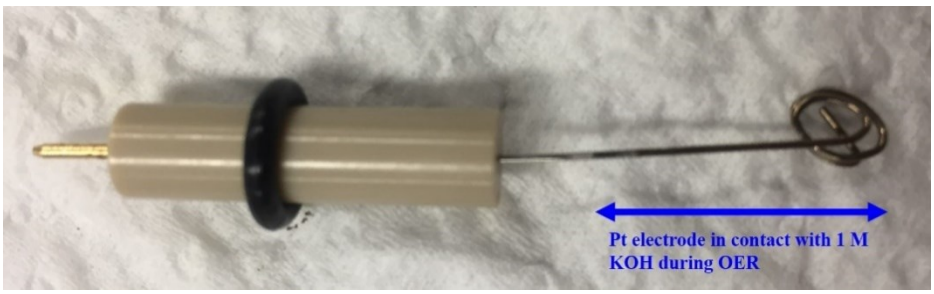

Figure S54. Pt counter electrode used during the OER experiments with FeAs/FTO. The lower part (which was in contact with the 1 M KOH solution) turned black due to the deposition of As.

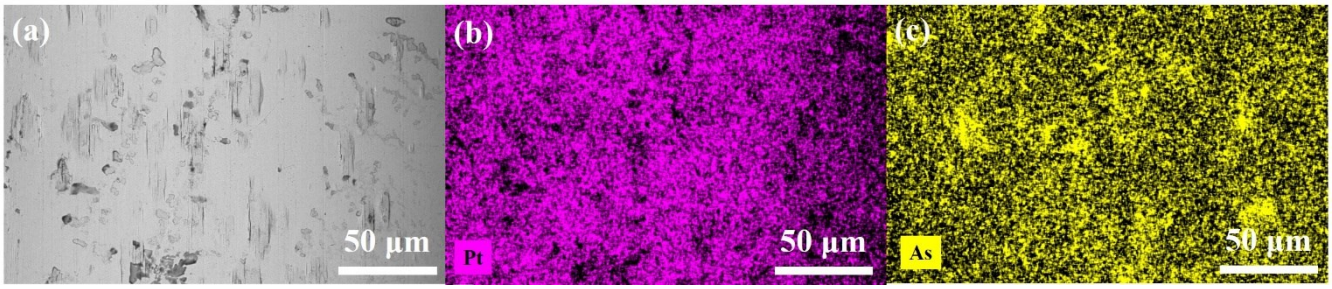

Figure S55. (a) SEM of the Pt counter electrode used during the OER experiments. Elemental mapping of (b) Pt (violet) and (c) As (yellow). The same measurements were done on the non-exposed part of the Pt counter electrode, showing no presence of As.

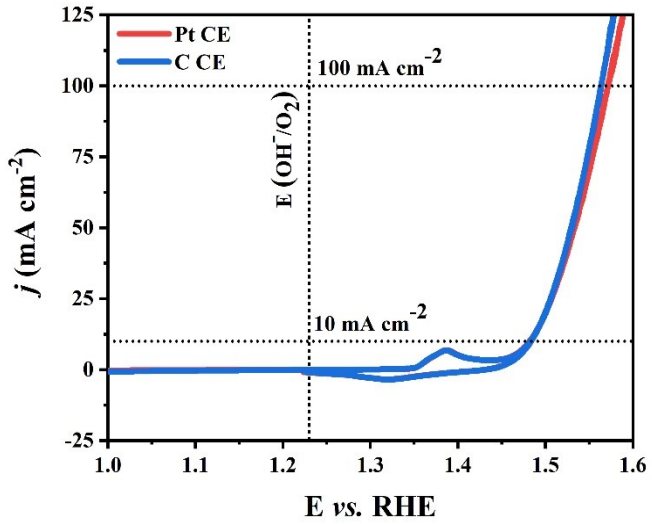

Figure S56. LSV (1 mV s^{-1}) for OER under 1 M KOH of FeAs/NF using a three electrode system. The effect of changing the CE was explored and Pt was replaced by a graphitic carbon rod. The difference in overpotential obtained by each material is minimum (1 mV).

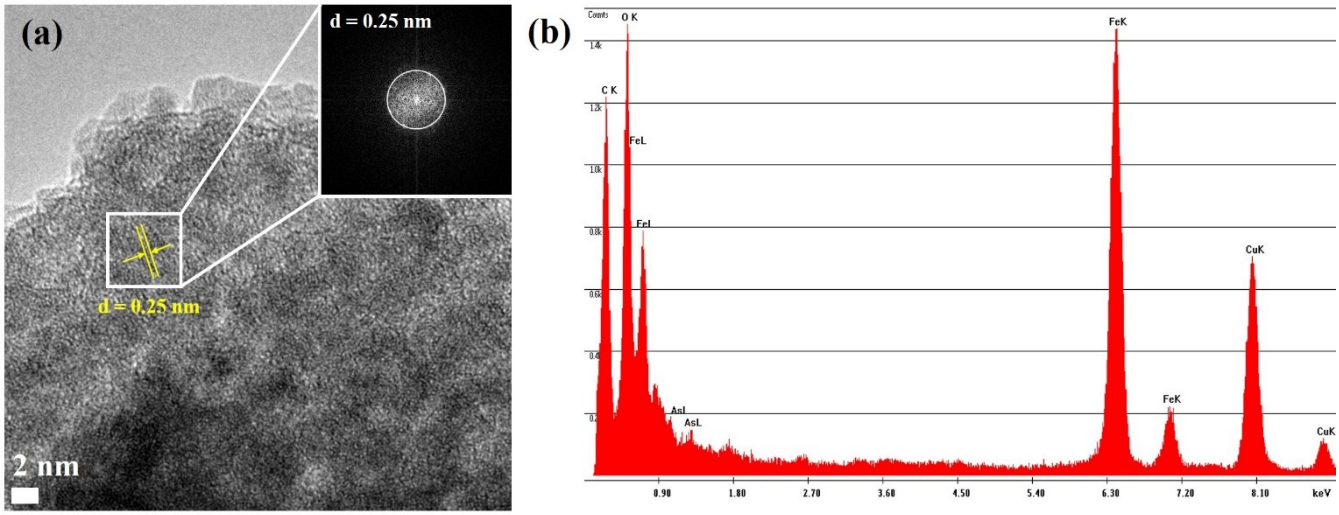

Figure S57. (a) High resolution (HR)-TEM and Fast Fourier Transform (FFT) (inset) of the selected area of FeAs/FTO after OER (CP OER 24h). The FFT reveals a lattice distance of ~0.25 nm, which corresponds to the (110) plane in 2-line ferrihydrite.[105–107] (b) TEM-EDX of FeAs/FTO after OER (CP OER 24 h). The presence of C and Cu arise from the carbon film substrate deposited on the 300 mesh Cu-grid used during the measurement. The Fe:As and Fe:O ratio can be derived from this experiment, resulting in 1:0.019* and 1:1.67*, respectively. The EDX results indicate that only 1.73%* of As is left after catalysis (*no error is included for the values because TEM-EDX was done once).

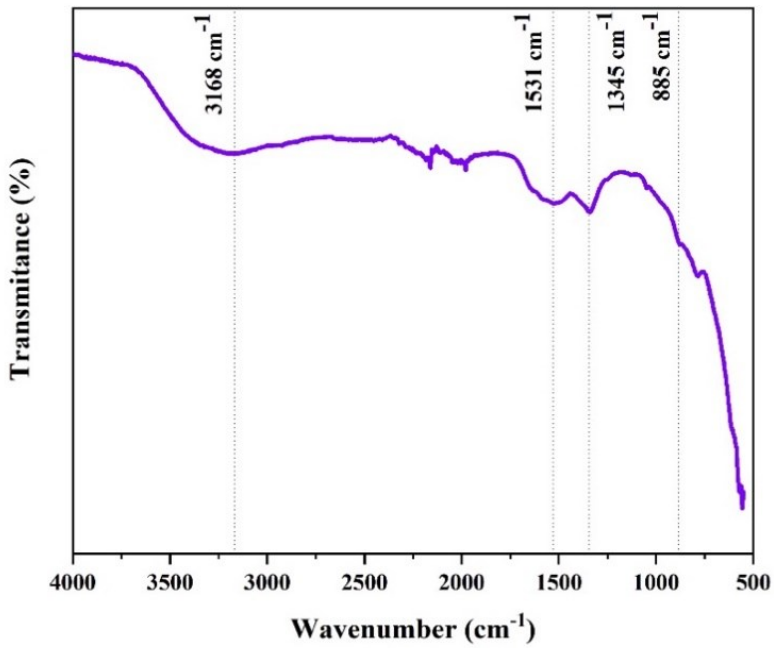

Figure S58. IR spectrum of FeAs/FTO after OER (CP OER 24h). The noted absorption bands have been observed before on pure 2-line ferrihydrite: (i) the absorption band at 3168 cm^{-1} is attributed to OH stretchings, (ii) the bands at 1531 and 1345 cm^{-1} are related to Fe-OH bending and Fe-O stretching, respectively, and (iii) at 885 cm^{-1} band corresponding to the bending vibration of the hydroxyl groups of iron hydroxides (Fe–OH).[108]

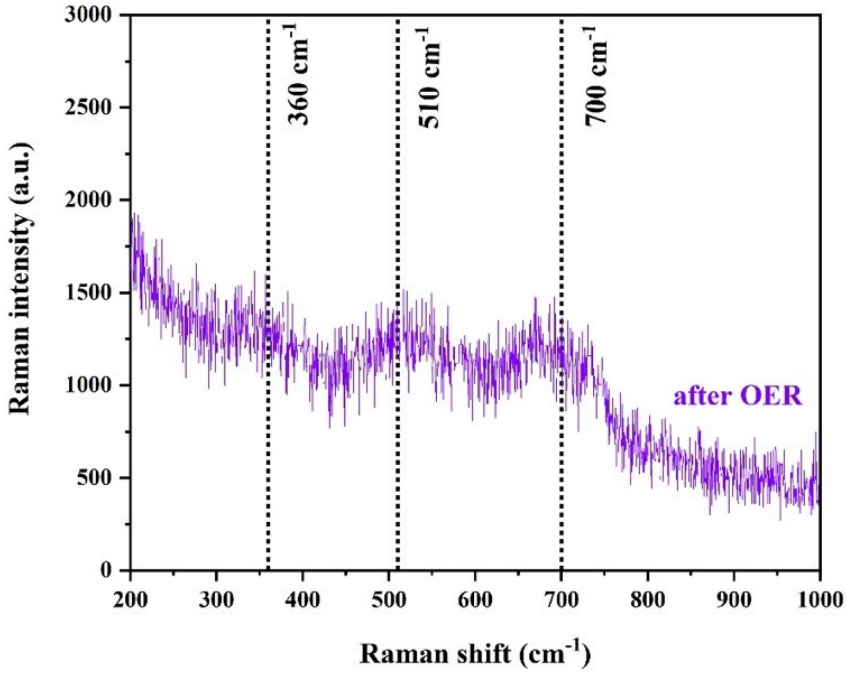

Figure S59. Raman spectrum of FeAs/FTO after CP OER 24 h. It shows three broad absorption bands that have been observed before on 2-line ferrihydrite.[108–112]

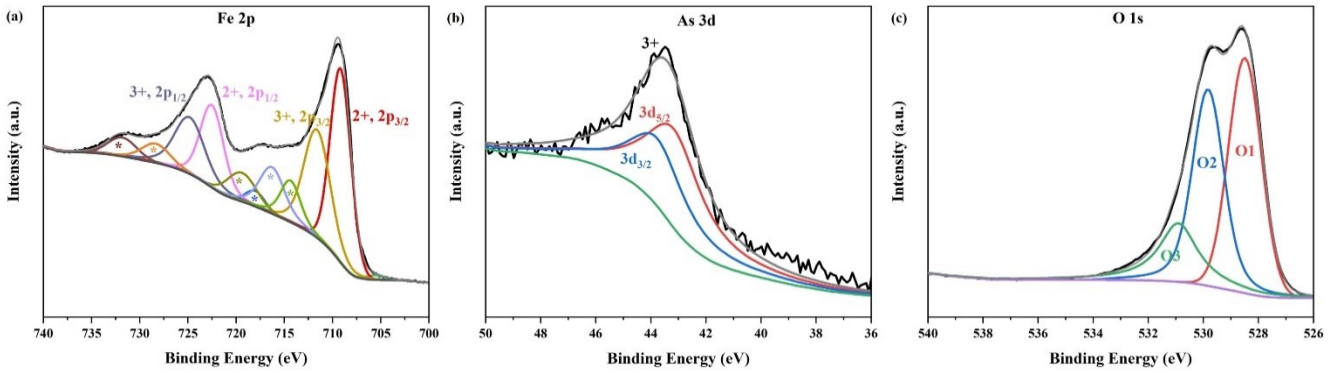

Figure S60. Deconvoluted XPS of FeAs/FTO after OER (CP OER 24h): (a) Fe 2p, (b) As 3d and (c) O 1s. The Fe 2p deconvoluted spectrum shows the disappearance of the peaks associated with $Fe^{\delta+}$, indicating the complete oxidation of the surface. The only peaks observed are related to Fe^{2+} ($2p_{3/2}$ 709.2 eV and $2p_{1/2}$ 722.6 eV) and Fe^{3+} ($2p_{3/2}$ 711.7 eV and $2p_{1/2}$ 725.0 eV), and the satellite peaks of Fe^{2+} ($2p_{3/2}$ 716.4 eV and $2p_{1/2}$ 728.6 eV) and Fe^{3+} ($2p_{3/2}$ 719.6 eV and $2p_{1/2}$ 732.0 eV). Moreover, at 714.5 eV is related to Sn ($3p_{3/2}$), which appears because of the exposure of the FTO-glass substrate (see Figure S48).[113] The As 3d deconvoluted spectrum shows that the peaks related to $As^{\delta-}$ present in FeAs have disappeared due to the oxidation of the surface and the loss of As into solution, as determined by ICP-AES. The only low intensity remaining peak (43.6 eV) is further deconvoluted into two peaks at 43.5 eV ($3d_{5/2}$) and 44.2 eV ($3d_{3/2}$), related to the presence of oxidized As^{5+}. Finally, the O 1s deconvoluted spectrum shows three peaks related to the oxidation of the FeAs precatalyst. The peaks at 528.5 eV (O1) and 529.8 eV (O2) are associated with oxygen with two different chemical environments on the 2-line ferrihydrite structure: Fe-O-Fe and Fe-O-H.[29,32,114] The last peak at 530.9 eV (O3) could be associated to the As-O peak (As^{5+} 530.9 eV).[30]

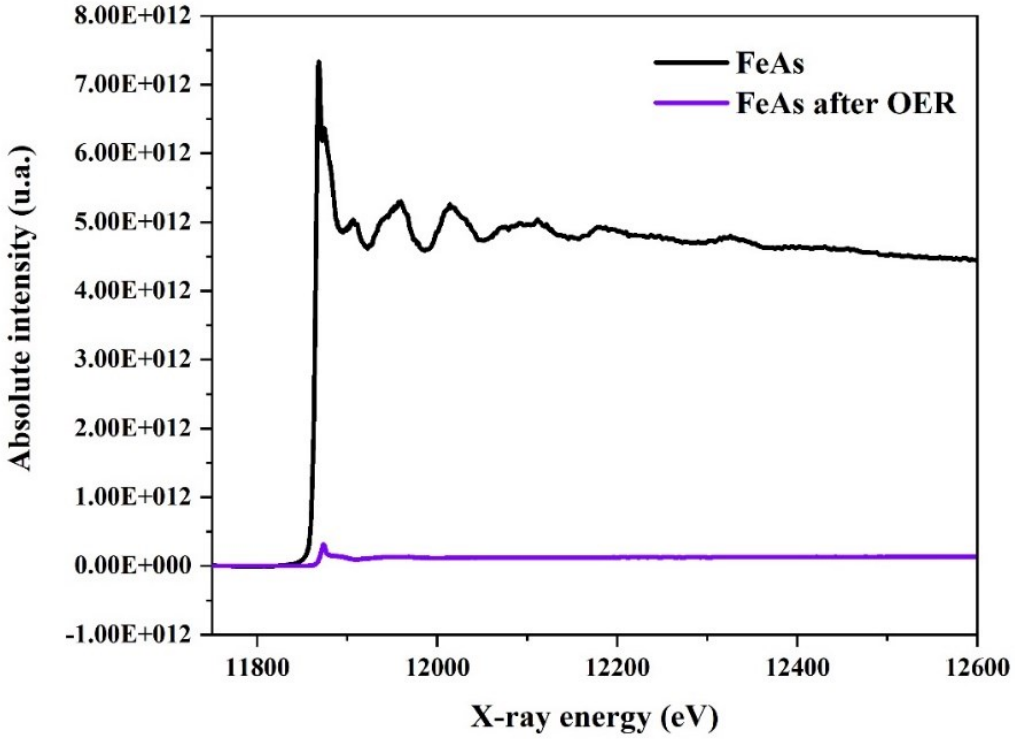

Figure S61. Absolute intensity of As-XANES fluorescence absorption for FeAs powder and FeAs after OER (CP OER 6 h 10 mA cm^{-2}). A case of "missing edge" is shown, in which the intensity of the signals after OER (CP OER 6 h 10 mA cm^{-2}) is reduced to a minimum due to the loss of As into the solution.

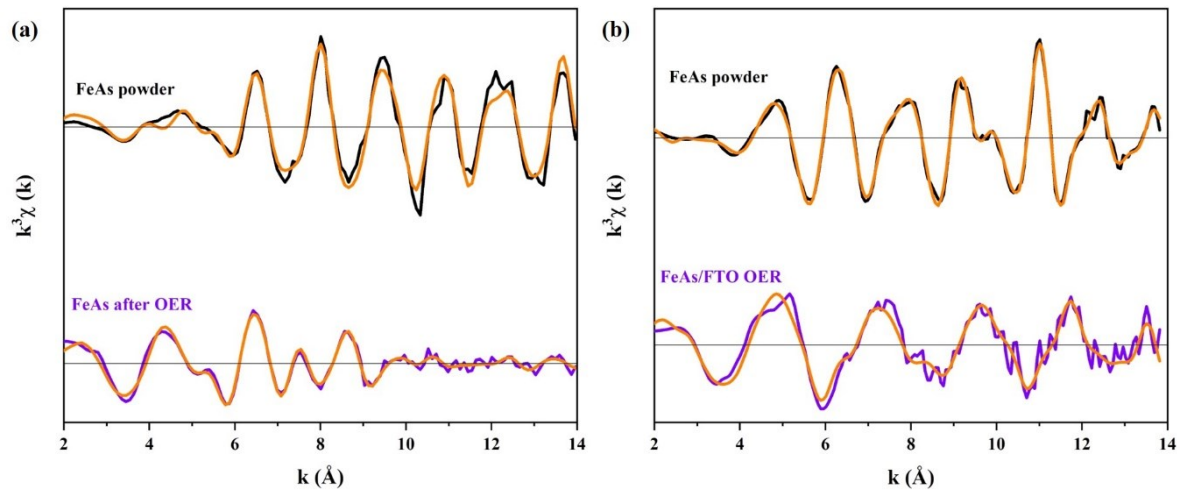

Figure S62. k^3-weighted EXAFS of (a) Fe and (b) As for FeAs powder and FeAs after OER (CP OER 6 h 10 mA cm^{-2}).

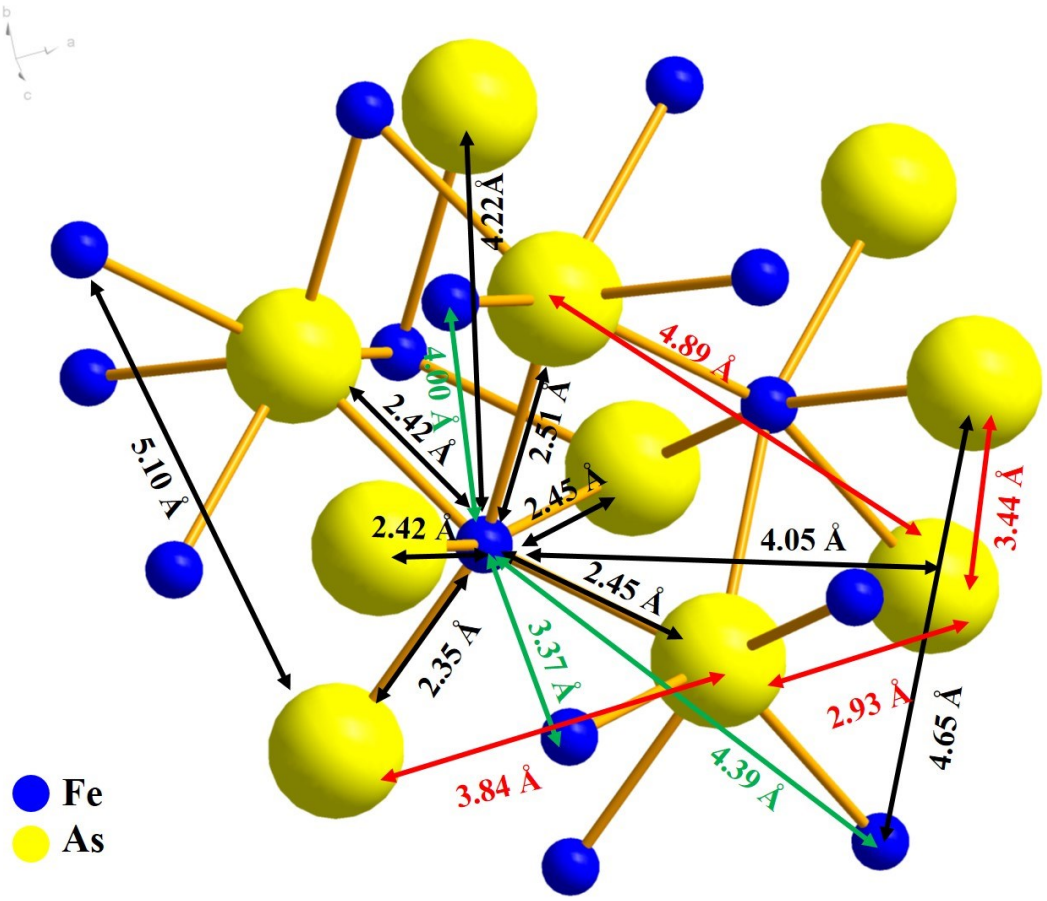

Figure S63. Distance between atoms on the FeAs structure (JCPDS 76-458, orthorhombic). Fe-As distances are shown in black, Fe-Fe in green and As-As in red.

Table S15. Fe-EXAFS fit parameters for the FeAs powder.

FeAs powder Fe-EXAFS (Rf = 14.0)							
type	N	err	R	R_{XRD}	err	DW	err
Fe-O	1.4	0.3	2.05		0.01	0.039	0.004
Fe-As	3.7	0.4	2.45	2.44	0.00	0.060	0.004
Fe-Fe	1.1	0.4	3.38	3.37	0.02	0.060	0.004
Fe-Fe	4.5	2.0	3.99	4.00	0.02	0.060	0.004
Fe-As	4.0	3.9	4.12	4.05	0.03	0.060	0.004
Fe-As	3.3	2.9	4.33	4.22	0.05	0.060	0.004
Fe-Fe	3.0	1.9	4.52	4.39	0.04	0.060	0.004

Table S16. As-EXAFS fit parameters for the FeAs powder.

FeAs powder As-EXAFS (Rf = 5.3)							
type	**N**	**err**	**R**	**R_{XRD}**	**err**	**DW**	**err**
As-O	0.7	0.2	1.76		0.02	0.043	0.014
As-Fe	3.0	0.5	2.40	2.41	0.01	0.043	0.018
As-Fe	1.8	0.3	2.51	2.48	0.01	0.043	0.018
As-As	1.4	0.3	2.90	2.93	0.00	0.043	0.018
As-As	3.8	1.8	3.47	3.44	0.01	0.078	0.018
As-As	4.9	2.8	3.81	3.84	0.01	0.078	0.018
As-Fe	2.0	1.5	4.10	4.13	0.03	0.078	0.018
As-Fe	4.4	5.1	4.74	4.65	0.03	0.078	0.018
As-As	7.7	9.0	4.89	4.89	0.01	0.078	0.018
As-Fe	5.4	4.7	5.17	5.10	0.03	0.078	0.018

Table S17. Fe-EXAFS fit parameters for the FeAs after OER (CP OER 6 h 10 mA cm^{-2}).

FeAs OER Fe-EXAFS (Rf = 9.9)							
type	N	err	R	R_{XRD}	err	DW	err
Fe-O	2.5	0.0	1.90	1.95	0.00	0.070	0.000
Fe-O	3.4	0.0	2.02	2.10	0.00	0.070	0.000
Fe-Fe	2.7	0.0	3.02	3.02	0.00	0.087	0.000
Fe-Fe	5.5	0.0	3.45	3.44	0.00	0.087	0.000
Fe-O	8.5	0.0	3.60	3.58	0.00	0.087	0.000
Fe-O	3.1	0.0	3.92	3.89	0.00	0.087	0.000
Fe-Fe	2.0	0.0	5.09	5.30	0.00	0.087	0.000
Fe-Fe	3.7	0.0	5.22	5.40	0.00	0.087	0.000

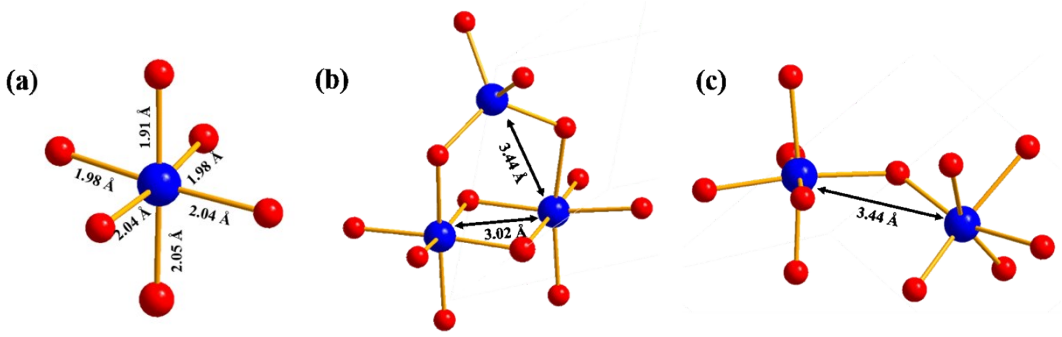

Figure S64. Structural motifs of the 2-line ferrihydrite structure.[106] The expected distances between Fe atoms (blue) and O atoms (red) are shown. Three different coordination environments for Fe in the 2-line ferrihydrite are shown: (a) FeO_6 octahedron, (b) two edge-sharing FeO_6 octahedra and one-corner sharing between the two FeO_6 octahedra and one FeO_4 tetrahedron (c) bent one-corner sharing between two FeO_6 octahedra.

References

[1] J. M. Smith, R. J. Lachicotte, P. L. Holland, *Organometallics* **2002**, *21*, 4808–4814.
[2] S. Yao, Y. Grossheim, A. Kostenko, E. Ballestero-Martínez, S. Schutte, M. Bispinghoff, H. Grützmacher, M. Driess, *Angew. Chemie Int. Ed.* **2017**, *56*, 7465–7469.
[3] J. M. Smith, R. J. Lachicotte, P. L. Holland, *Chem. Commun.* **2001**, *1998*, 1542–1543.
[4] P. H. M. Budzelaar, A. B. van Oort, A. G. Orpen, *Eur. J. Inorg. Chem.* **1998**, *1998*, 1485–1494.
[5] J. M. Smith, R. J. Lachicotte, P. L. Holland, *J. Am. Chem. Soc.* **2003**, *125*, 15752–15753.
[6] H. Andres, E. L. Bominaar, J. M. Smith, N. A. Eckert, P. L. Holland, E. Münck, *J. Am. Chem. Soc.* **2002**, *124*, 3012–3025.
[7] J. M. Smith, R. J. Lachicotte, P. L. Holland, *Organometallics* **2002**, *21*, 4808–4814.
[8] J. Vela, J. M. Smith, Y. Yu, N. A. Ketterer, C. J. Flaschenriem, R. J. Lachicotte, P. L. Holland, *J. Am. Chem. Soc.* **2005**, *127*, 7857–7870.
[9] J. M. Smith, R. J. Lachicotte, P. L. Holland, *Chem. Commun.* **2001**, *1*, 1542–1543.
[10] R. Beltrán-Suito, P. W. Menezes, M. Driess, *J. Mater. Chem. A* **2019**, *7*, 15749–15756.
[11] F. Gilbert, P. Refait, F. Lévêque, C. Remazeilles, E. Conforto, *J. Phys. Chem. Solids* **2008**, *69*, 2124–2130.
[12] P. W. Menezes, A. Indra, I. Zaharieva, C. Walter, S. Loos, S. Hoffmann, R. Schlögl, H. Dau, M. Driess, *Energy Environ. Sci.* **2019**, *12*, 988–999.
[13] A. L. Ankudinov, B. Ravel, J. J. Rehr, S. D. Conradson, *Phys. Rev. B* **1998**, *58*, 7565–7576.
[14] L. Trotochaud, S. L. Young, J. K. Ranney, S. W. Boettcher, *J. Am. Chem. Soc.* **2014**, *136*, 6744–6753.
[15] C. C. L. L. McCrory, S. Jung, J. C. Peters, T. F. Jaramillo, *J. Am. Chem. Soc.* **2013**, *135*, 16977–16987.
[16] C. C. L. McCrory, S. Jung, I. M. Ferrer, S. M. Chatman, J. C. Peters, T. F. Jaramillo, *J. Am. Chem. Soc.* **2015**, *137*, 4347–4357.
[17] S. Anantharaj, S. R. Ede, K. Karthick, S. Sam Sankar, K. Sangeetha, P. E. Karthik, S. Kundu, *Energy Environ. Sci.* **2018**, *11*, 744–771.
[18] S. Anantharaj, S. Noda, *ChemElectroChem* **2020**, *7*, 2297–2308.
[19] Q. Kang, L. Vernisse, R. C. Remsing, A. C. Thenuwara, S. L. Shumlas, I. G. McKendry, M. L. Klein, E. Borguet, M. J. Zdilla, D. R. Strongin, *J. Am. Chem. Soc.* **2017**, *139*, 1863–1870.
[20] N. Koura, T. Tsukamoto, HiromasaShoji, T. Hotta, *Jpn. J. Appl. Phys.* **1995**, *34*, 1643–1647.
[21] P. W. Menezes, C. Panda, S. Loos, F. Bunschei-Bruns, C. Walter, M. Schwarze, X. Deng, H. Dau, M. Driess, *Energy Environ. Sci.* **2018**, *11*, 1287–1298.
[22] C. Panda, P. W. Menezes, S. Yao, J. Schmidt, C. Walter, J. N. Hausmann, M. Driess, *J. Am. Chem. Soc.* **2019**, *141*, 13306–13310.
[23] K. Selte, A. Kjekshus, A. F. Andresen, M. J. Tricker, S. Svensson, *Acta Chem. Scand.* **1972**, *26*, 3101–3113.
[24] K. Selte, A. Kjekshus, J. Sletten, L. Torbjörnsson, P.-E. Werner, U. Junggren, B. Lamm, B. Samuelsson, *Acta Chem. Scand.* **1969**, *23*, 2047–2054.
[25] K. Selte, A. Kjekshus, C. Hyatt, G. D. Stucky, B. Lüning, C.-G. Swahn, *Acta Chem. Scand.* **1973**, *27*, 1448–1449.
[26] P. Desai, K. Song, J. Koza, A. Pariti, M. Nath, *Chem. Mater.* **2013**, *25*, 1510–1518.
[27] S. C. Zhao, D. Hou, Y. Wu, T. L. Xia, A. M. Zhang, G. F. Chen, J. L. Luo, N. L. Wang, J. H. Wei, Z. Y. Lu, et al., *Supercond. Sci. Technol.* **2009**, *22*, 015017.
[28] A. P. Litvinchuk, V. G. Hadjiev, M. N. Iliev, B. Lv, A. M. Guloy, C. W. Chu, *Phys. Rev. B - Condens. Matter Mater. Phys.* **2008**, *78*, 4–7.
[29] B. J. Tan, K. J. Klabunde, P. M. A. Sherwood, *Chem. Mater.* **1990**, *2*, 186–191.
[30] J. M. Epp, J. G. Dillard, *Chem. Mater.* **1989**, *1*, 325–330.
[31] D. E. King, J. E. Fernandez, W. E. Swartz, *Appl. Surf. Sci.* **1990**, *45*, 325–339.
[32] N. S. McIntyre, D. G. Zetaruk, *Anal. Chem.* **1977**, *49*, 1521–1529.

[33] L. Negahdar, F. Zeng, S. Palkovits, C. Broicher, R. Palkovits, *ChemElectroChem*, **2019**, *6*, 5588-5595
[34] A. R. C. Bredar, A. L. Chown, A. R. Burton, B. H. Farnum, *ACS Appl. Energ. Mater.*, **2020**, *3*, 66-98
[35] M. V. Abrashev, P. Chernev, P. Kubella, M. R. Mohammadi, C. Pasquini, H. Dau, I. Zaharieva, *J. Mater. Chem. A*, **2019**, *7*, 17022-17036
[36] G. Li, L. Anderson, Y. Chen, M. Panb, P. A. Chuang, *Sustain. Energy Fuels*, **2018**, *2*, 237-251
[37] Y. Mo, D. A. Scherson, *J. Electrochem. Soc.* **2003**, *150*, E39-E46
[38] Y. Qu, M. Shao, Y. Shao, M. Yang, J. Xu, C. T. Kwok, X. Shi, Z. Lu, H. Pan *J. Mater. Chem. A*, **2017**, *5*, 15080
[39] J. N. Hausmann, E. M. Heppke, R. Beltrán-Suito, J. Schmidt, M. Mühlbauer, M. Lerch, P. W. Menezes, M. Driess, *ChemCatChem* **2020**, *12*, 1–9.
[40] J. Masa, S. Piontek, P. Wilde, H. Antoni, T. Eckhard, Y. Chen, M. Muhler, U. Apfel, W. Schuhmann, *Adv. Energy Mater.* **2019**, 1900796.
[41] S. Yao, V. Forstner, P. W. Menezes, C. Panda, S. Mebs, E. M. Zolnhofer, M. E. Miehlich, T. Szilvási, N. Ashok Kumar, M. Haumann, et al., *Chem. Sci.* **2018**, *9*, 8590–8597.
[42] J. Masud, S. Umapathi, N. Ashokaan, M. Nath, *J. Mater. Chem. A* **2016**, *4*, 9750–9754.
[43] B. Zhang, K. Jiang, H. Wang, S. Hu, *Nano Lett.* **2019**, *19*, 530–537.
[44] D. Li, H. Baydoun, B. Kulikowski, S. L. Brock, *Chem. Mater.* **2017**, *29*, 3048–3054.
[45] Y. Yan, B. Y. Xia, X. Ge, Z. Liu, A. Fisher, X. Wang, *Chem. - A Eur. J.* **2015**, *21*, 18062–18067.
[46] Y. Zhu, W. Zhou, Y. Chen, J. Yu, X. Xu, C. Su, M. O. Tadé, Z. Shao, *Chem. Mater.* **2015**, *27*,3048–3054.
[47] J. Zou, G. Peleckis, C. Y. Lee, G. G. Wallace, *Chem. Commun.* **2019**, *55*, 8808–8811.
[48] X. Zou, Y. Wu, Y. Liu, D. Liu, W. Li, L. Gu, H. Liu, P. Wang, L. Sun, Y. Zhang, *Chem* **2018**, *4*, 1139–1152.
[49] H. Li, P. Wen, Q. Li, C. Dun, J. Xing, C. Lu, S. Adhikari, L. Jiang, D. L. Carroll, S. M. Geyer, *Adv. Energy Mater.* **2017**, *7*, 1–12.
[50] X. Zhang, L. An, J. Yin, P. Xi, Z. Zheng, Y. Du, *Sci. Rep.* **2017**, *7*, 1–10.
[51] P. T. Babar, B. S. Pawar, A. C. Lokhande, M. G. Gang, J. S. Jang, M. P. Suryawanshi, S. M. Pawar, J. H. Kim, *J. Energy Chem.* **2017**, *26*, 757–761.
[52] J. Lee, H. Lee, B. Lim, *J. Ind. Eng. Chem.* **2018**, *58*, 100–104.
[53] X. Zhang, B. Zhang, S. Liu, H. Kang, W. Kong, S. Zhang, Y. Shen, B. Yang, *Appl. Surf. Sci.* **2018**, *436*, 974–980.
[54] H. A. Bandal, A. R. Jadhav, A. A. Chaugule, W. J. Chung, H. Kim, *Electrochim. Acta* **2016**, *222*, 1316–1325.
[55] M. Tavakkoli, T. Kallio, O. Reynaud, A. G. Nasibulin, J. Sainio, H. Jiang, E. I. Kauppinen, K. Laasonen, *J. Mater. Chem. A* **2016**, *4*, 5216–5222.
[56] Y. Zhang, G. Jia, H. Wang, B. Ouyang, R. S. Rawat, H. J. Fan, *Mater. Chem. Front.* **2017**, *1*, 709–715.
[57] G. Ren, L. Gao, C. Teng, Y. Li, H. Yang, J. Shui, X. Lu, Y. Zhu, L. Dai, *ACS Appl. Mater. Interfaces* **2018**, *10*, 10778–10785.
[58] D. Xiong, X. Wang, W. Li, L. Liu, *Chem. Commun.* **2016**, *52*, 8711–8714.
[59] Y. Yan, B. Zhao, S. C. Yi, X. Wang, *J. Mater. Chem. A* **2016**, *4*, 13005–13010.
[60] F. Yu, H. Zhou, Z. Zhu, J. Sun, R. He, J. Bao, S. Chen, Z. Ren, *ACS Catal.* **2017**, *7*, 2052–2057.
[61] S. Chen, Z. Kang, X. Zhang, J. Xie, H. Wang, W. Shao, X. Zheng, W. Yan, B. Pan, Y. Xie, *ACS Cent. Sci.* **2017**, *3*, 1221–1227.
[62] R. Gao, H. Zhang, D. Yan, *Nano Energy* **2017**, *31*, 90–95.
[63] C. Panda, P. W. Menezes, C. Walter, S. Yao, M. E. Miehlich, V. Gutkin, K. Meyer, M. Driess, *Angew. Chemie Int. Ed.* **2017**, *56*, 10506–10510.
[64] D. Zhong, L. Liu, D. Li, C. Wei, Q. Wang, G. Hao, Q. Zhao, J. Li, *J. Mater. Chem. A* **2017**, *5*, 18627–18633.
[65] L. Yang, Z. Guo, J. Huang, Y. Xi, R. Gao, G. Su, W. Wang, L. Cao, B. Dong, *Adv. Mater.* **2017**,

29, 1–9.
[66] V. Mani, S. Anantharaj, S. Mishra, N. Kalaiselvi, S. Kundu, *Catal. Sci. Technol.* **2017**, *7*, 5092–5104.
[67] F. Guo, Y. Wu, H. Chen, Y. Liu, L. Yang, X. Ai, X. Zou, *Energy Environ. Sci.* **2019**, *12*, 684–692.
[68] Z. Qiu, C. W. Tai, G. A. Niklasson, T. Edvinsson, *Energy Environ. Sci.* **2019**, *12*, 572–581.
[69] Q. Qian, Y. Li, Y. Liu, L. Yu, G. Zhang, *Adv. Mater.* **2019**, *31*, 1–8.
[70] H. Qiu, P. Du, K. Hu, J. Gao, H. Li, P. Liu, T. Ina, K. Ohara, Y. Ito, M. Chen, *Adv. Mater.* **2019**, *31*, 1900843.
[71] Y. Wu, X. Tao, Y. Qing, H. Xu, F. Yang, S. Luo, C. Tian, M. Liu, X. Lu, *Adv. Mater.* **2019**, *31*, 1900178.
[72] Y. Zhou, Z. Wang, Z. Pan, L. Liu, J. Xi, X. Luo, Y. Shen, *Adv. Mater.* **2019**, *31*, 1806769.
[73] J. Zhu, M. Xiao, G. Li, S. Li, J. Zhang, G. Liu, L. Ma, T. Wu, J. Lu, A. Yu, et al., *Adv. Energy Mater.* **2020**, *10*, 1903003.
[74] H. Khani, N. S. Grundish, D. O. Wipf, J. B. Goodenough, *Adv. Energy Mater.* **2020**, *10*, 1903215.
[75] B. H. R. Suryanto, Y. Wang, R. K. Hocking, W. Adamson, C. Zhao, *Nat. Commun.* **2019**, *10*, 1–10.
[76] Y. Duan, Z. Y. Yu, S. J. Hu, X. S. Zheng, C. T. Zhang, H. H. Ding, B. C. Hu, Q. Q. Fu, Z. L. Yu, X. Zheng, et al., *Angew. Chemie - Int. Ed.* **2019**, *58*, 15772–15777.
[77] C. Wang, H. Yang, Y. Zhang, Q. Wang, *Angew. Chemie - Int. Ed.* **2019**, *58*, 6099–6103.
[78] H. Wang, J. Wang, Y. Pi, Q. Shao, Y. Tan, X. Huang, *Angew. Chemie - Int. Ed.* **2019**, *58*, 2316–2320.
[79] Z. Tan, L. Sharma, R. Kakkar, T. Meng, Y. Jiang, M. Cao, *Inorg. Chem.* **2019**, *58*, 7615–7627.
[80] S. Niu, W. J. Jiang, Z. Wei, T. Tang, J. Ma, J. S. Hu, L. J. Wan, *J. Am. Chem. Soc.* **2019**, *141*, 7005–7013.
[81] C. Wang, R. Wang, Y. Peng, J. Chen, J. Li, *Chem. Commun.* **2019**, *55*, 10944–10947.
[82] C. Zhang, B. Zhang, Z. Li, J. Hao, *ACS Appl. Energy Mater.* **2019**, *2*, 3343–3351.
[83] S. A. Khalate, S. A. Kadam, Y. R. Ma, S. S. Pujari, S. J. Marje, P. K. Katkar, A. C. Lokhande, U. M. Patil, *Electrochim. Acta* **2019**, *319*, 118–128.
[84] M. Abu Sayeed, G. J. Millar, A. P. O'Mullane, *ChemElectroChem* **2019**, *6*, 3667–3673.
[85] S. A. Shah, Z. Ji, X. Shen, X. Yue, G. Zhu, K. Xu, A. Yuan, N. Ullah, J. Zhu, P. Song, et al., *ACS Appl. Energy Mater.* **2019**, *2*, 4075–4083.
[86] X. Zhang, H. Xu, X. Li, Y. Li, T. Yang, Y. Liang, *ACS Catal.* **2016**, *6*, 580–588.
[87] F. Song, M. M. Busch, B. Lassalle-Kaiser, C. S. Hsu, E. Petkucheva, M. Bensimon, H. M. Chen, C. Corminboeuf, X. Hu, *ACS Cent. Sci.* **2019**, *5*, 558–568.
[88] J. X. Feng, S. H. Ye, H. Xu, Y. X. Tong, G. R. Li, *Adv. Mater.* **2016**, *28*, 4698–4703.
[89] L. Wang, J. Li, X. Zhao, W. Hao, X. Ma, S. Li, Y. Guo, *Adv. Mater. Interfaces* **2019**, *6*, 1–6.
[90] S. Song, J. Zhou, X. Su, Y. Wang, J. Li, L. Zhang, G. Xiao, C. Guan, R. Liu, S. Chen, et al., *Energy Environ. Sci.* **2018**, *11*, 2945–2953.
[91] D. Chen, M. Qiao, Y. R. Lu, L. Hao, D. Liu, C. L. Dong, Y. Li, S. Wang, *Angew. Chemie - Int. Ed.* **2018**, *57*, 8691–8696.
[92] F. Song, X. Hu, *Nat. Commun.* **2014**, *5*, 4477.
[93] P. Babar, A. Lokhande, H. H. Shin, B. Pawar, M. G. Gang, S. Pawar, J. H. Kim, *Small* **2018**, *14*, 1–8.
[94] X. Zhu, T. Jin, C. Tian, C. Lu, X. Liu, M. Zeng, X. Zhuang, S. Yang, L. He, H. Liu, et al., *Adv. Mater.* **2017**, *29*, 1–6.
[95] J. Wang, L. Gan, W. Zhang, Y. Peng, H. Yu, Q. Yan, X. Xia, X. Wang, *Sci. Adv.* **2018**, *4*, 1–9.
[96] F. Lyu, Y. Bai, Q. Wang, L. Wang, X. Zhang, Y. Yin, *Mater. Today Chem.* **2019**, *11*, 112–118.
[97] B. Zhang, X. Zheng, O. Voznyy, R. Comin, M. Bajdich, M. Garcia-Melchor, L. Han, J. Xu, M. Liu, L. Zheng, et al., *Science (80-.).* **2016**, *352*, 333–337.
[98] M. Zhou, Q. Weng, X. Zhang, X. Wang, Y. Xue, X. Zeng, Y. Bando, D. Golberg, *J. Mater.*

Chem. A **2017**, *5*, 4335–4342.
[99] J. Yu, G. Cheng, W. Luo, *J. Mater. Chem. A* **2017**, *5*, 15838–15844.
[100] B. Q. Li, S. Y. Zhang, C. Tang, X. Cui, Q. Zhang, *Small* **2017**, *13*, 1–6.
[101] X. Xu, F. Song, X. Hu, *Nat. Comm.* **2016**, *7*, 1–7.
[102] M. Chatti, A. M. Glushenkov, T. Gengenbach, G. P. Knowles, T. C. Mendes, A. V. Ellis, L. Spiccia, R. K. Hocking, A. N. Simonov, *Sustain. Energy Fuels* **2018**, *2*, 1561–1573.
[103] F. Zhou, A. Izgorodin, R. K. Hocking, L. Spiccia, D. R. MacFarlane, *Adv. Energy Mater.* **2012**, *2*, 1013–1021.
[104] A. J. Esswein, Y. Surendranath, S. Y. Reece, D. G. Nocera, *Energy Environ. Sci.* **2011**, *4*, 499–504.
[105] D. E. Janney, J. M. Cowley, P. R. Buseck, *Clays Clay Miner.* **2000**, *48*, 111–119.
[106] F. M. Michel, L. Ehm, S. M. Antao, P. L. Lee, P. J. Chupas, G. Liu, D. R. Strongin, M. A. A. Schoonen, B. L. Phillips, J. B. Parise, *Science.* **2007**, *316*, 1726–1729.
[107] J. L. Jambor, J. E. Dutrizac, *Chem. Rev.* **1998**, *98*, 2549–2586.
[108] K. Rout, M. Mohapatra, S. Anand, *Dalt. Trans.* **2012**, *41*, 3302–3312.
[109] S. Das, M. Jim Hendry, J. Essilfie-Dughan, *Appl. Geochemistry* **2013**, *28*, 185–193.
[110] M. Hanesch, *Geophys. J. Int.* **2009**, *177*, 941–948.
[111] L. Mazzetti, P. J. Thistlethwaite, *J. Raman Spectrosc.* **2002**, *33*, 104–111.
[112] D. L. A. de Faria, S. Venâncio Silva, M. T. de Oliveira, *J. Raman Spectrosc.* **1997**, *28*, 873–878.
[113] W. E. Morgan, J. R. Van Wazer, *J. Phys. Chem.* **1973**, *77*, 964–969.
[114] I. Banerjee, Y. B. Khollam, C. Balasubramanian, R. Pasricha, P. P. Bakare, K. R. Patil, A. K. Das, S. V. Bhoraskar, *Scr. Mater.* **2006**, *54*, 1235–1240.